creative commons
COMMONS DEED

저작자표시-비영리-변경금지 2.0 대한민국

이용자는 아래의 조건을 따르는 경우에 한하여 자유롭게

- 이 저작물을 복제, 배포, 전송, 전시, 공연 및 방송할 수 있습니다.

다음과 같은 조건을 따라야 합니다:

저작자표시. 귀하는 원저작자를 표시하여야 합니다.

비영리. 귀하는 이 저작물을 영리 목적으로 이용할 수 없습니다.

변경금지. 귀하는 이 저작물을 개작, 변형 또는 가공할 수 없습니다.

- 귀하는, 이 저작물의 재이용이나 배포의 경우, 이 저작물에 적용된 이용허락조건을 명확하게 나타내어야 합니다.
- 저작권자로부터 별도의 허가를 받으면 이러한 조건들은 적용되지 않습니다.

저작권법에 따른 이용자의 권리는 위의 내용에 의하여 영향을 받지 않습니다.

이것은 이용허락규약(Legal Code)을 이해하기 쉽게 요약한 것입니다.

Disclaimer

dCollection

工學博士學位論文

Shape Control of Electrospun 1D metal oxide/carbon Nanomaterials by Adjusting Precursor and Their Sensor Applications

전기 방사의 전구체 조절을 통한 일차원 금속산화물/탄소 나노 소재의 표면 형상 제어방법과 이의 센서로의 응용

2018年 2月

서울大學校 大學院

化學生物工學部

全 在 彣

↑
2cm
↓

Shape Control of Electrospun 1D metal oxide/carbon Nanomaterials by Adjusting Precursor and Their Sensor Applications

2018年

全 在 彣

↑
2.5cm
↓

↑
4cm
↓

↑
3cm
↓

↑
2cm
↓

Shape Control of Electrospun 1D metal oxide/carbon Nanomaterials by Adjusting Precursor and Their Sensor Applications

by

Jaemoon Jun

Submitted to the Graduate School of Seoul National University in Partial Fulfillment of the Requirements for the Degree of Doctor of Philosophy

February, 2018

Thesis Adviser: Jyongsik Jang

Abstract

Due to the structural properties such as high aspect ratio and specific surface area, one-dimensional (1D) nanomaterials have been studied variously for improving the physical properties through constitution and structural molding. Electrospinning is one of the methods for manufacturing 1D nanomaterials using viscous polymer solution. It is advantageous that application fields are greatly expanded because manufacturing is relatively simple from organic materials to inorganic materials by changing spinning conditions. However, there is still lack of research on manufacturing methods for forming a precise 1D structure through the spinning conditions of electrospinng, and methods for manufacturing 1D organic/inorganic composite nanomaterial by deepening it.

This dissertation proposes a method to control the structure shape and composition of the final 1D nanomaterials by applying a mixed polymer solution, solvent and metal oxide precursor to electrospinning. In order to improve the performance, a method of fabricating 1D organic/iorganic composite nanomaterials by coating a conducting polymer, polypyrrole (PPy) on the surface of 1D nanomaterials was

proposed and applied to various sensor fields.

Fistlty, polymer solution containing poly(methyl methacrylate) (PMMA), poly(acrylonitrile) (PAN) and cobalt acetate was applied to electrospinning to prepare phase separated nanofibers. Using this method, cobalt oxide nanopartilces (NPs) embedded multichannel carbon nanofibers (C_MCNFs) was fabricated and applied as a glucose sensor electrode material.

Secondly, the method of controlling shape of 1D nanomaterial by mixing two solvents and finally fabricating a complex tube structure for high performance DMMP gas sensor was demonstrated.

Third, to fabricate a metal oxide NPs decorated ultrathin CNF (ZCNF), a polymer solution with a mixture of poly (vinlypyrrolidone) (PVP), PAN and zinc acetate was applied to electrospinng. By using the ZCNF as a sensor electrode, we realized a platelet derived growth factor biosensor with a high sensitivity and fast response time

Keywords: electrospinning, one-dimensional nanomaterials, carbon nanofiber, metal oxide, polypyrrole, sensor

Student Number: 2013-22535

List of Abbreviations

-NH_2: amino group

1D: one-dimension

2D: two dimension

3D: three dimension

A: ampere

Ag/AgCl electrode: silver chloride electrode

Ag: silver

Au: gold

ca.: circa

cm: centi-meter

CPs: conducting polymers

CPMCNFs: Carboxylated polypyrrole-coated hybrid carbon nanofibers

CPZCNF: carboxylated polypyrrole-coated, zinc oxide-decorated ultrafine carbon nanofibers

C_MCNF: cobalt oxide nanoparticles (NPs) embedded multichannel carbon nanofibers

CNF: carbon nanofiber

CNT: carbon nanotube

D: drain

DMF: dimethyl formamide

e^- :electron

eV: electron volt

fcc: face-centered-cubic

FE-SEM: field emission-scanning electron microscopy

$FeCl_3$: iron (III) chloride

FET: field-effect-transistor

fM: femto- mole

FT-IR: fourier transform-infrared

GCE: glassy carbon electrode

GOx: glucose oxidase

HR-TEM: high resolution-transmission electron microscopy

hr: hour

I-V: current-voltage

I: instantaneous recorded current

I_0: initial current

I_{SD}-V_{SD}: source-drain current versus source-drain voltage

I_{SD}: source-drain current

M: mole

MCNF: multichannel carbon nanofiber

MDL: minimum detectable level

MFC: mass flow controller

MWNT: multiwall carbon nanotube

min: minute

mM: milli-mole

N_2: nitrogen

NaOH: sodium hydroxide

nm: nano-meter

nM: nano-mole

NO_2: nitrogen dioxide

p-type: positive-type

p: partial pressure

PA: polyacetylene

PAN: polyacrylonitrile

PANI: polyaniline

PBS: phosphate-buffered saline

PEDOT: poly(3,4-ethylenedioxylthiophene)

PMMA: poly(methyl methacrylate)

ppb: parts per billion

ppm: parts per million

PPy: polypyrrole

PPy@SnO_2 tube-in-tube: PPy coated SnO_2 tube in tube structure

PSe: polyselenophene

Pt: platinum

PT: polythiophene

PVP: poly(vinylpyrrolidone)

r: adsorption rate

R_0: initial resistance

rGO: reduced graphene oxide

S/N: signal to noise

s: second

S: source or sensitivity

sccm: standard cubic centimeters per minute

slm: standard liters per minute

SnO_2: tin dioxide

SO_4^{2-}: sulfate ion

SWNT: single wall nanotube

TEM: transmission electron microscopy

V: voltage

VDP: vapor deposition polymerization

V_G: gate voltage

XPS: x-ray photoemission spectroscopy

XRD: x-ray diffraction

ΔR: resistance change

θ: fraction of metal covered by target gas

μm: micro-meter

ZCNF: ZnO nanonodule-decorated hybrid CNFs

ZnO: zinc oxide

List of Figures

Figure 1. Schematic diagram for fabrication of polymer nanofibers by electrospinning

Figure 2. Electrospinning schematic with variation for diiffent processing outcomes

Figure 3. Various conducting polymer structures

Figure 4. Possible chemical structures in PPy chains

Figure 5. Electronic energy diagrams for (a) neutral (b) polaron, (c) bipolaron, and (d) fully doped PPy, respectively

Figure 6. Structure for (a) neutral, (b) polaron, (c) bipolaron PPy, respectively

Figure 7. Schematic of gas sensor fabrication techniques

Figure 8. Schematic diagram illustrating the fabrication procedure of multichannel carbon nanofiber (MCNF) (inset is optical microscopy of immisible polymer solution)

Figure 9. (a) Field-emission scanning electron microscopy (FE-SEM)

and (b) Transmission electron microscopy (TEM) images of phase separated polymer nanofiber. (c) Low- and (d) high-resolution cross sectional FE-SEM image of multichannel carbon nanofiber

Figure 10. (a, d) Transmission electron microscopy (TEM) and scanning electron microscopy (SEM) images of the MCNF_5. (b, e) TEM and SEM images of the MCNF_7. (c, f) TEM and SEM images of the MCNF_9

Figure 11. Schematic diagram of the sequential fabrication of the C-MCNFs

Figure 12. XRD patterns of MCNFs (black: MCNF_5; red: MCNF_7; blue: MCNF_9)

Figure 13. Raman spectroscopy of MCNFs (black: MCNF_5; red: MCNF_7; blue: MCNF_9)

Figure 14. Nitrogen adsorption–desorption isotherm curves of (a) MCNF_5, (b) MCNF_7 and (c) MCNF_9

Figure 15. Barrett–Joyner–Halenda (BJH) pore-size distribution curves

of (a) MCNF_5, (b) MCNF_7 and (c) MCNF_9

Figure 16. (a)Low-and (b)high resolution field-emission scanning electron microscopy(FE-SEM)images of the C0.05-MCNFs. (c)low-,(d)mid- and (e)high magnification transmission electron microscopy (TEM) image of the C0.05-MCNF. (f)High resolution-TEM (HR-TEM)image of the cobalt nanoparticle

Figure 17. Field-emission scanning electron microscopy(FE-SEM)images of the C-MCNFs.(a)Low-and (b)High-resolution FE-SEM images of the C0.01-MCNF. (d)Low-and (e)high resolution FE-SEM images of the C0.1-MCNF. Transmission electron microscopy (TEM) image of the (c)C0.01-MCNF and (f)C0.1-MCNF

Figure 18. High-angle annular dark field (HAADF)-scanning electron transmission microscopy (STEM)-electron energy-loss spectroscopy (EELS) image of the C0.05-MCNF. EELS elemental mapping of C0.05-MCNF surface components indicating (b)whole, (c)carbon, (d)cobalt, (e)oxygen and (f)nitrogen

Figure 19. XRD patterns of C-MCNFs (green: C0.01-MCNF; orange: C0.05-MCNF; purple: C0.1-MCNF; Blue: C0.2-MCNF)

Figure 20. FT-IR spectra of C-MCNFs (green: C0.01-MCNF; orange: C0.05-MCNF; purple: C0.1-MCNF; Blue: C0.2-MCNF)

Figure 21. Raman spectroscopy of C-MCNFs (green: C0.01-MCNF; orange: C0.05-MCNF; purple: C0.1-MCNF; Blue: C0.2-MCNF)

Figure 22. Nitrogen adsorption–desorption isotherm curves of (a)C0.01-MCNF, (b) C0.05-MCNF, and (c) C-0.1_MCNF

Figure 23. Barrett–Joyner–Halenda (BJH) pore-size distribution curves of (a)C0.01-MCNF, (b) C0.05-MCNF, and (c) C0.1_MCNF

Figure 24. Detection of glucose in 0.1 M NaOH solution by using the C0.05_MCNF. a) CV curves measured at diffent scan rates b) CV curves in the presence of various concentrations of glucose

Figure 25. Amperometric response of the C0.05_MCNF electrode (at 0.58 V) upon addition of glucose with increasing concentrations

Figure 26. Amperometric response of the C0.05_MCNF with the addition of diffent analytes

Figure 27. Schematic diagram of the sequential fabrication of the PPy@SnO_2 tube-in-tube structure

Figure 28. (a, c) Transmission electron microscopy (TEM) and scanning electron microscopy (SEM) images of the SnO_2 fibers. (b, d) TEM and SEM images of the SnO_2 tubes

Figure 29. Transmission electron microscopy (TEM) images of the PPy@SnO_2 tube in tube by conducting the VDP step at different temperature (a)60℃ and (b)100℃

Figure 30. TEM image of the morphology of the PPY coated SnO2 tube structure after VDP method in ambient state

Figure 31. (a) Field-emission scanning electron microscopy (FE-SEM) image of the electrospun nanofiber. (b) Low-and (c) high-resolution FE-SEM images of the tube-in-tube SnO_2. (d) Low-and (e) high-resolution transmission electron microscopy (TEM) image of the tube-in-tube SnO_2. (f) Selected area electron diffraction (SAED) pattern of the

tube-in-tubeSnO_2. (g) FE-SEM and (h) TEM images of the tube-in-tube polypyrrole (PPy)/SnO_2. (i) High-resolution TEM image of the tube-in-tube PPy/SnO_2

Figure 32. Low-and (c) high-resolution FE-SEM images of the tube-in-tube SnO_2

Figure 33. X-ray diffraction (XRD) pattern for the tube-in-tube SnO_2 (blue) and tube-in-tube PPy@SnO_2 (black) structures. (b) Fourier transform-infrared (FT-IR) spectra of the tube-in-tube SnO_2 (blue) and tube-in-tube PPy@SnO_2 (black) structures. (c) High-resolution N 1s X-ray photoelectron (XPS) spectra of the tube-in-tube SnO_2 (blue) and tube-in-tube PPy@SnO_2 (black) structures. (d) High-resolution Sn 3d pattern of the tube-in-tube PPy@SnO_2

Figure 34. X-ray photoelectron spectroscopy (XPS) analysis of a fully scanned spectra (0–1200 eV)

Figure 35. EDS dot mapping of PPy@SnO_2 tube in tube surface components indicating (a)overall SEM image, (b)carbon, (c)nitrogen, (d)tin, (e)oxygen and (f)iron

Figure 36. EDX spectrum of the PPy@SnO_2 tube in tube surface

Figure 37. Nitrogen adsorption–desorption isotherm curves of (a) Fiber, (b) Tube, and (c) Tube-in-tube

Figure 38. (a)Low- and (b) high-resolution optical microscopy images of the interdigitated array (IDA) electrode

Figure 39. Current–voltage (I–V) curve of the tube-in-tube PPy@SnO_2 sensor electrode

Figure 40. Molecular structures of (a) dimethyl methylphosphonate (DMMP) and (b) polypyrrole (PPy). (c) Schematic diagram describing the effect of hydrogen bonding on PPy

Figure 41. (a, b) Real-time responses of the tube-in-tube PPy@SnO_2 structure upon periodic exposure to dimethyl methylphosphonate (DMMP); (a) 0.05 ppb to 0.1 ppm and (b) 0.05 ppb. (c) Long-term stability of the tube-in-tube PPy@SnO_2 structure. (d) Selective DMMP-sensing characteristics of the tube-in-tube PPy@SnO_2 structure with respect to interfering analytes; each analyte concentration was fixed at 1 ppm. (acetone, water, benzene, hexane,

toluene and chloroform)

Figure 42. Schematic diagram of the formation of a p-n junction

Figure 43. SEM image of the PPy@SnO_2 nanoparticles

Figure 44. Real-time monitoring of PPy@SnO_2 having different one-dimensional (1D) structures after sequential exposure to DMMP

Figure 45. Real-time responses of the PPy@SnO_2 nanoparticles upon periodic exposure to dimethyl methylphosphonate(DMMP); 0.1 ppb to 1 ppm

Figure 46. Changes in sensitivity as a function of DMMP concentration calculated from the real-time responses

Figure 47. Variation and comparison of the sensitivity parameter. These parameters were evaluated from 10 devices fabricated at 1 ppm

Figure 48. Illustrative diagram of the sequential fabrication steps for 3-carboxylated PPy coated hybrid carbon nanofibers (CPMCNFs)

Figure 49. (a) SEM and (b) TEM image of ZnO nanonodule decorated

on the surface CNFs with 40 nm-diameters

Figure 50. TEM and (b) HR-TEM image of 3-carboxylated PPy coated hybrid CNFs with 3 nm-thickness coated layer on the surface

Figure 51. FT-IR spectra of MCNFs (red) and CPMCNFs (blue)

Figure 52. Synthetic protocol of immobilization of CPMCNF-aptamer tranducers on the inter-digitated array electrode substrate

Figure 53. (a) Current-voltage (I-V) curves of aptamer-conjugated CPMCNF immobilized IDA electrode (black: without aptamer; red: low concentration of conjugated-aptamer; blue: high concentration of conjugated-aptamer). (b) Schematic diagram of a liquid-ion gated

Figure 54. Real-time responses with normalized current changes (Vg: 50 mV and Vsd: 50 mV) and (b) calibration curve of CPB-Apt FET sensor toward three variants of PDGF with different concentration (black: PDGF_AA; red: PDGF_AB; blue: PDGF_BB)

Figure 55. TEM image of Carboxylated polypyrrole(CPPy) coated

pristine CNFs using vapor deposition polymerization (VDP). There was CPPy layer on the surface of CNFs

Figure 56. Control experiment using (a) CPPy coated MCNFs without PDGF-B binding aptamer and (b) CPPy coated pristine CNFs with aptamer

Figure 57. Real-time selective responses of CPB-Apt FET sensor toward (a) 1 μM of non-target molecules (ATP, BSA, Calmoduline (Cal), PDGF-AA) and 500 fM of target molecules (PDGF-BB and PDGF-AB) and (b) 5 fM of different target molecules (Vg: 50 mV; Vsd: 50 mV)

Figure 58. Re-usability test of the CPB-Apt FET sensor system toward three variants of PDGF at 50 pM concentration (black: PDGF-AA; red: PDGF-AB; blue: PDGF-BB)

List of Tables

Table 1. Room-temperature sensing properties of the tube in tube PPy@SnO_2-based sensor toward DMMP in comparison with other nanomaterial reported in the literature

Table of Contents

Abstract ..... **i**

List of Abbreviations ..... **iii**

List of Figures ..... **ix**

List of Tables ..... **xvi**

List of Contents ..... **xvii**

1. Introduction 1

1.1 Background **1**

1.1.1 One-dimensional nanomaterials 1

1.1.1.1 Nanofiber 2

1.1.1.2 Nanotubes 3

1.1.2 Electrospinning method 4

1.1.2.1 Electrospun 1D carbon nanomaterial 8

1.1.2.2 Electrospun 1D metaloxide nanomaterial 9

1.1.2.2.1 Tin dioxide 11

1.1.2.2.2 Cobaltic oxide 11

1.1.2.3 Composite nanomaterial 12

1.1.3 Polypyrrole 13
1.1.4 Sensor applications 19
1.1.4.1 Chemical Sensor 21
1.1.4.1.1 DMMP gas sensor 24
1.1.4.2 Bio sensor 26
1.1.4.2.2 Glucose sensor 28
1.1.4.2.2 Platelet-derived growth factor (PDGF) sensor 29

1.2 Objectives and Outlines 31
1.2.1 Objectives 31
1.2.2 Outlines 32

2. Experimental Details 34

2.1 Fabrication of a One-dimensional cobalt oxide NPs embedded multichannel carbon nanofibers for glucose sensor 34
2.1.1 Materials 34
2.1.2 Fabrication of MCNFs 34
2.1.3 Fabrication of C_MCNFs 35
2.1.4 Electrochemical measurement 35
2.1.5 Characterization 36

2.2 Fabrication of a One-dimensional Tube-in-tube

Polypyrrole/Tin oxide Structure for Highly Sensitive DMMP Sensor Applications 37

2.2.1 Materials 37

2.2.2 Fabrication of the tube-in-tube SnO_2 37

2.2.3 Fabrication of the PPy@SnO_2 tube-in-tube structure 38

2.2.4 Characterization of the PPy@SnO_2 tube-in-tube structure 38

2.2.5 Electrical sensitivity measurements of the tube-in-tube PPy@SnO_2 39

2.3 Fabrication of One-dimensional nano-nodule decorated Carbon Nanofiber for a Highly Sensitive and Selective Platelet-Derived Growth Factor Biosensor 40

2.3.1 Materials 40

2.3.2 Fabrication of MCNFs 40

2.3.3 Fabrication of CPMCNFs 41

2.3.4 Fabrication of the CPB-Apt FET sensor 42

2.3.5 Characterization 42

2.3.6 Electrical measurements with the CPB-Apt sensor 43

3. Results and Disccusions 44

3.1 Fabrication of a One-dimensional cobalt oxide NPs embedded multichannel carbon nanofibers for glucose sensor 44

3.1.1 Fabrication of Materials 44

3.1.1.1 Fabrication of MCNFs 44

3.1.1.2 Fabrication of C-MCNFs 50

3.1.2 Characterization 53

3.1.2.1 Characterization of MCNFs 53

3.1.2.2 Characterization of C-MCNFs 59

3.1.2.3 Electrochemical sensing performance 71

3.2 Fabrication of a One-dimensional Tube-in-tube Polypyrrole/Tin oxide Structure for Highly Sensitive DMMP Sensor Applications 76

3.2.1 Fabrication of the materials 76

3.2.2 Characterizations 82

3.2.3 Electrical sensor measurements 93

3.3 Fabrication of One-dimensional nano-nodule decorated Carbon Nanofiber for a Highly Sensitive and Selective Platelet-Derived Growth Factor Biosensor 108

3.3.1 Fabrication of CPMCNFs 108

3.3.2 Fabrication of the CPB-Apt FET sensor 115

3.3.3 Real-time responses of the CPB-Apt FET sensor 120

4. Conclusion.....129

Reference.....132

국문초록 140

1. Introduction

1.1 Background

1.1.1 One-dimensional nanomaterials

Along with the development of nanotechnology over the years, studies have been to synthesize and improve various nanomaterials and apply them to appropriate field. In genrally, nanomaterials are classified into four types as mophologically zero, one, two, and three dimension structure.[1, 2] Among the nanomaterials, one-dimensional (1D) nanomaterials have received much attention due to their intriguing features and great potential in various application such as catalysis, energy conversion/storage system, chemical gas sensor, and many others.[3-7] 1D materials including nanowire, nanofiber and nanotube exhibit high electron mobility, specific surface area and catalytic properties due to their high aspect ratio and directional structure.[4, 5]

1.1.1.1 Nanofiber

Nanofibes are collectively referred to as fibers with diameters in the nanometer range and are 1D nanomaterials having physical properties different form those of conventional fibers. Nanofibers can be categorized into natural polymers (e.g. silk fibroin, keratin, gelatin, cellulose, collagen, and so on) and synthetic resin (e.g. poly (lactic acid) (PLA), polyurethane (PU), polyacrylonitrile (PAN), polymethylmethacrylate (PMMA), and so on).[8, 9] In general, polymer nanofiber chains are connected via covalent bonds and diameters depend on the type of polymer and synthetic method.

Nanofibers have various application potentials owing to their unique properties such as high surface area, porosity and flexibility.

There are many different methods to synthetic nanofibers, including drawing, self-assembly, template synthesis and electospinning. Among the methods, electospinning is the commonly used facile method to generate the nanofibers.[10]

1.1.1.2. Nanotubes

Nanotube is a tube like stuructre with a nanometer scale. The first nanotube to be discoverd were carbon nanotubes. Carbon nanotube is a kind of nanotube, which has cylindrical hollow carbon structure with lenth-to ratio of up to 132,000,000:1, stiffness and strength.[11] In particular, carbon nanotubes have application potentials thanks to their high thermal conductivity, mechanical properties, and electrical conducitivity. Nanotubes are categorized as single-wall nanotubes (SWNTs) and multi-wall nanotubes (MWNTs). Nanotubes composed of various materials such as DNA, boron nitride, cobalt oxide, tin oxide, gallium nitride, silicon, titania, and other metal oxides have been disclosed, and the manufacturing method and properties have been explored.[12-17] In recent years, many researches have been made to make a hollow structure of a nanotube not a general structure but a complex structure. Such complex hollow nano structure exhibit different physical properties, higher surface area and porosity compared to general nanotubes.

1.1.2. Electrospinning

Electrospinning is a facile, simple and versatile method for generating 1D nanomaterials with diameter on both the micro- and nanoscales.[10, 18-20]

Electrospinning shares the characteristcs of the electrospray method and the conventional solution dry spinning method by applying a high voltage electric force to the polymer solution or polymer melt to evaporate the solvent and extract the solid nanofibers (**Figure 1**).[18, 21]

When a sufficient voltage is applied to a liquid droplet, a charge is generated in the liquid. If the charge of the droplet exceeds the surface tention force, the droplet is stretched. When the critical point is reached, a flow of the liquid is ejected from the surface. This ejected form is called Taylor cone. Then, the jet is formed, and the jet collects in a fiber form through a process of elongating and thinning the collector on the opposite side.[21, 22]

The electrospun nanofibers can be molded in to various shapes or components depending on the type of polymer solution, processing condition, and atmosphere condition. The basic component of an electrospinning setup are a syringe attached to a syring pump, metal

collector, and voltage supply. The variations of electrospinning are composed of syringe needle, liquid for spinning, apparatus and metal collector as shown in **Figure 2**. In particular, liquid for electrospinning such as polymer melt, polymer solution, and suspension is important factor to control the composition of final 1D nanomaterials. In recent years, Carbon or metal oxide 1D nanomaterials are fabricated using electospun nanofibers for precursor via heat treatment. In addition, there have been lot of studies for manufacturing organic/inorganic 1D nanomaterials by electrospun nanofiber.[20, 21]

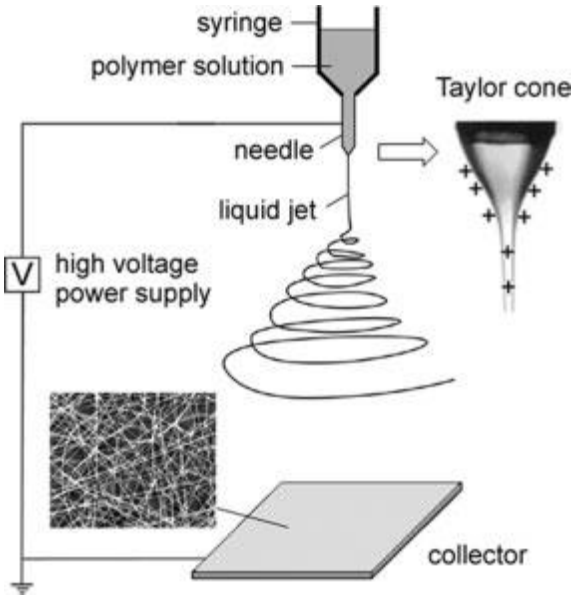

Figure 1. Schematic diagram for fabrication of polymer nanofibers by electrospinning[10]

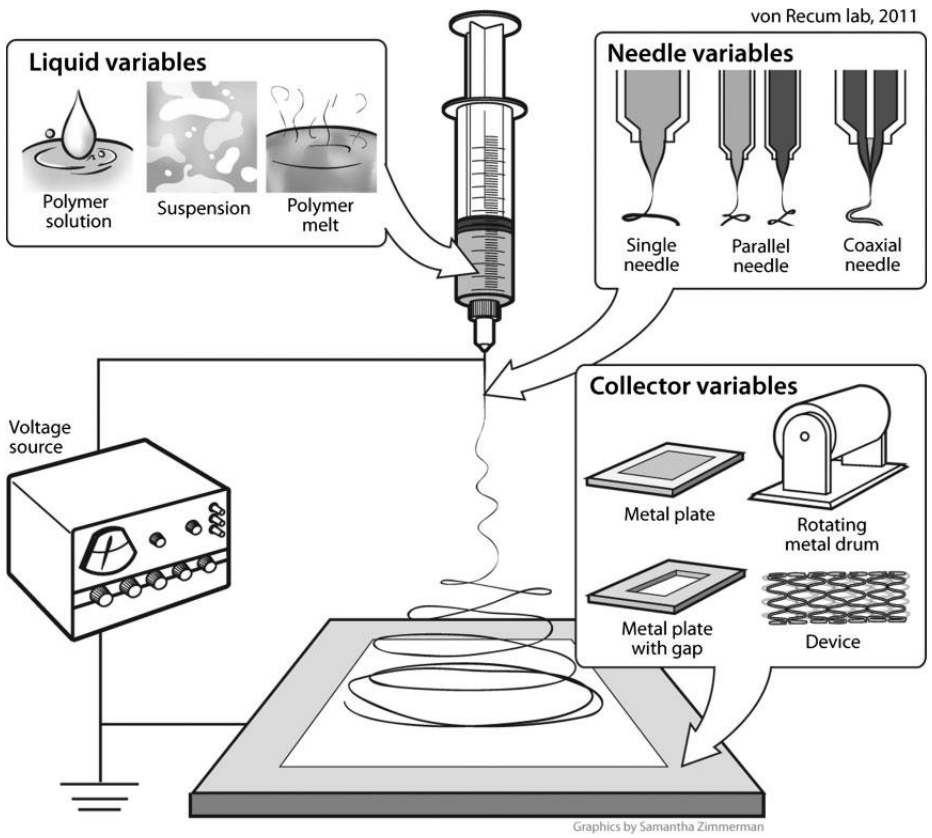

Figure 2. Electrospinning schematic with variation for diiffent processing outcomes[21]

1.1.2.1 Electrospun 1D carbon nanomaterial

The electrospun polymer nanofibers are applied to the precursors of 1D carbon nanomaterials. PAN and pitches are commonly used as carbon nanofiber precursors, similar to conventional carbon fiber process. In addition, poly(vinyl alcohol) (PVA), polyimides (PIs), polybenzimidazole (PBI), phenolic resin and lignin also used.[23-25]

In order to make the electrospun polymer into carbon, a heat treatmetnt process is essential. Theoretically, polymer nanofibers with carbon backbones can be converted to carbon materials and heat treat ment is accompanied by a thermal stabilization process and a high temperature carbonization process. If the thermal stabilization process is not followed, the cross-linking process of the carbon molecules does not proceed and the 1D sturucture may collapse. In recent years, studies have been made to modify the shape and porosity of the final carbon nanomaterials by controlling the type of polymer and processing condition.[23, 25-27]

1.1.2.2. Electrospun 1D metaloxide nanomaterial

1D Metal oxide nanomaterials have been studied by numerous research group for their futuristic applications in chemical catalyst, supercapacitor, battery, gas sensor, bio sensor, and waste water treatment due to their catalytic properties, high surface area to volume ratio, porosity and other properties.[4, 7, 19] Several methods for the fabrication of 1D metal oxide nanomaterials, like nanocraving, vapor-liquid-solid (VLS), and electrospinning.[3, 18] Amongst them, electrospinning is possibly the most adaptable, which allows for the control of diameter, pore structure, orientation, and compostion of the resulting 1D metal oxide materials.in general, heat treatment step (calcination) at high temperature is necessary to form the metal oxide. During the calcination step, the metal oxide nanocrystals begin to grow with nucleate, and at the same time, the polymer scaffold is thermally decomposed to form 1D metal oxide crystals.[3, 28]

Metal oxides have been developed for bio and chemical sensor applications. When applied as a biosensor, metal oxide 1D nanomaterial enhances the performance of the actual sensor as wll as to preserve the electrocatalytic activity due to their direct electron transfer. In chemical sensor, metal oxide based gas sensors give a

conductance change according to the chemical interaction btween the reducing/oxidizieng gases.[29]

1.1.2.2.1. Tin dioxide

Tin dioxide (SnO_2), which is a typrical metal oxide has been considered as n-type semiconductor with wide band gap.[28, 30, 31] There have been several studies based on the SnO_2 as chemical sensor transducer for broad spectrum of species, such as, H_2S, H_2, CO_2 and so on.[32-35] However, it is difficult to obtain high quality SnO_2 nanocrystals because of the strong trend of aggregation.[36]

1.1.2.2.2 Cobalt oxide

Cobalt oxide is p-type metal oxide semiconductor which have high theoretical specific capacitance, good redox performance, easily controllable size or shape, and tunable structural identities.[37, 38] Owing to these advantages, cobalt oxide have been studied for use in variety of applications such as lithium ion batteries, supercapacitor, and gas sensor. The catalytic activities of the Co_3O_4 materials depend on its size and morphology for therire diffent abilities of electron transfer. However, the spontaneous aggregation of Co_3O_4 materials is still unsolved.[39-41]

1.1.2.3 Composite materials

During the past years, there has been an increasing intrest in organic-inorganic composite materials from the viewpoints of both research and industrial fields. This strategy leads to improvement of mechanical, chemical and physical properties of the materials through a synergic interaction between the two phases.[42-44]

In general, inorganic materials for sensor application still require a high operating temperature to detect target analyte. Organic-based sensors have fast response/recovery timeas at room temperature; however, issues related to the poor stability of organic materials hider their use in sensor applications. Therefore, the use of composite nanomaterials of these two classes of materials may result in improved gas sensors that are more efficient at room temperature.[42, 43]

1.1.3 Polypyrrole

Conducting polymers are polymer which have conduct electricity through π-conjugation in their main chain. Singce the discovery of polyacetylene in 1977, a variety of conducting polymers such as polypyrrole (PPy), polyaniline (PANI), polythiophene (PT), poly(para-phenylene vinylene) (PPV), and poly(3,4-ethylenedioxythiophene) (PEDOT) have beend discovered and studied (**Figure 3)**.[45] In general, the conducting polymers include alternating single bond (σ bond) and double bond (π bond), and the electrical properties are obtained through the resonance thereof.[46-48]

Among the conducint polymers, PPy is one of the best known conducting polymers and contains five membered heterocyclic rings. Due to its high electrical properties and redox properties, PPy has been studied extensively for applictions (**Figure 4**).[49]

There are four diffent electronic band structures depending on the doping level of the PPy chain. In the neutral state, PPy is an insulator with a large $\pi-\pi^*$ band gap (ca. 3.16 eV). When a negative charge is extracted from the neutral component of the PPy chain by the doping process, a polaron (a radical cation) is formed du to a local deformation from the benzenoid to quinoid structure. This formation

of polaron generates two lovalized electron levels (bonding and antibonding) whith in the band gap (**Figure 5**).[50] As the oxidateive doping proceeds further, the formation of double charged bipolaron is formed, because another electron is removed. At higher oxidation level, the bipolarons overlap and thus the foarmation of two narrow bipolaronic bond is formed (**Figure 6**).[50]

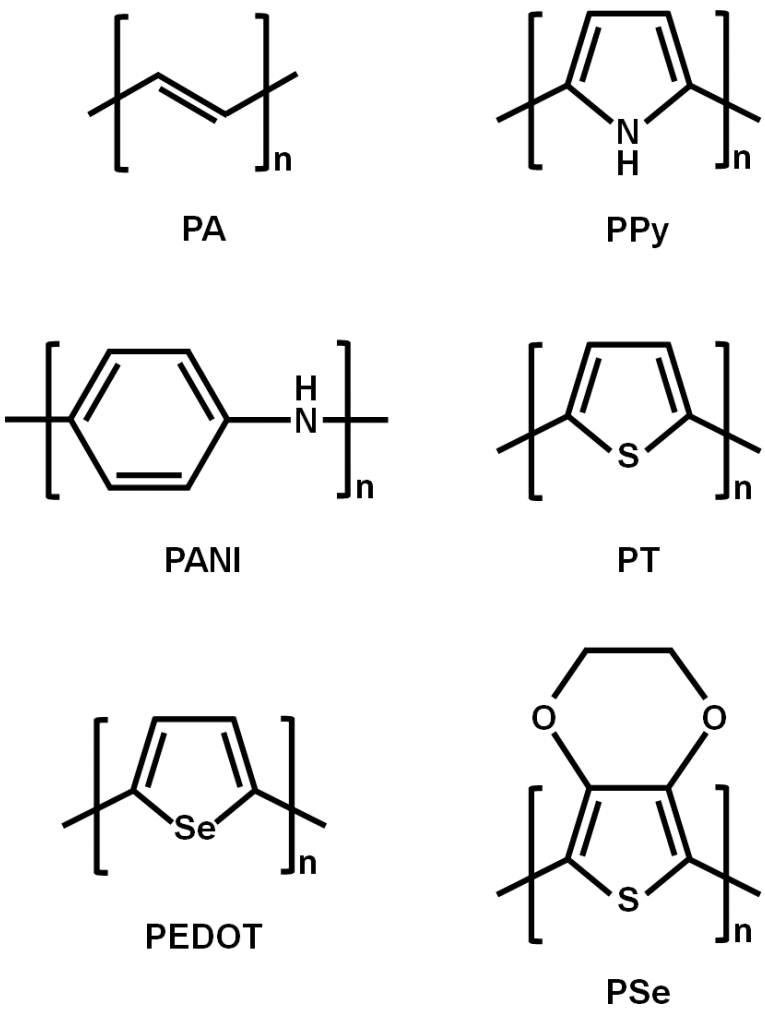

Figure 3. Various conducting polymer structures[45]

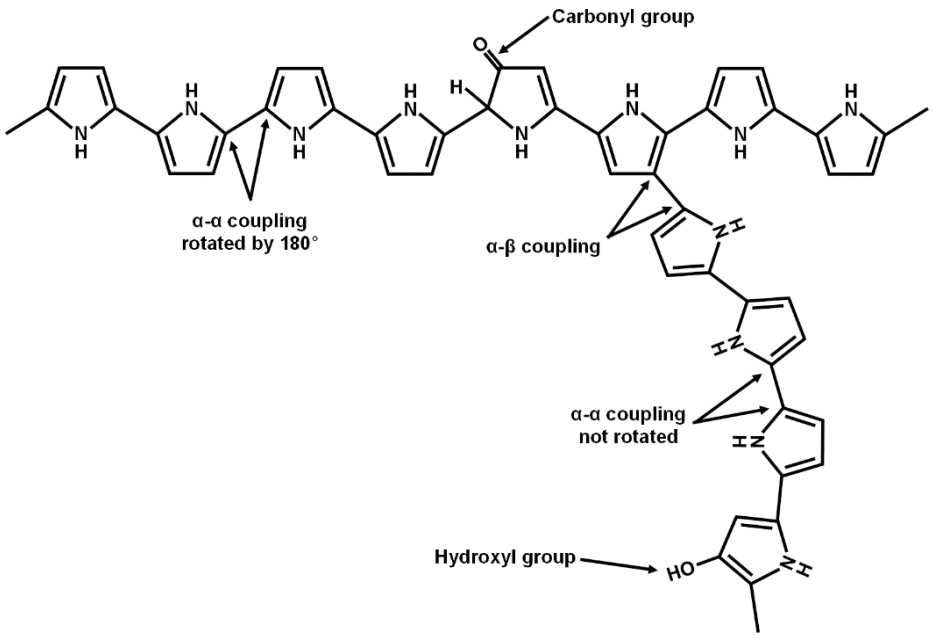

Figure 4. Possible chemical structures in PPy chains[49]

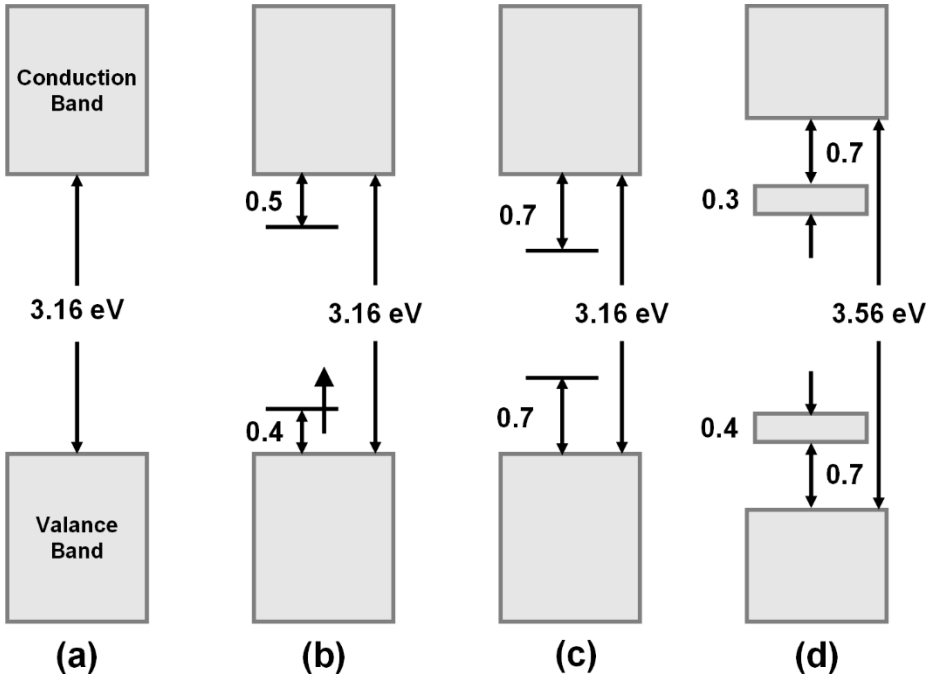

Figure 5. Electronic energy diagrams for (a) neutral (b) polaron, (c) bipolaron, and (d) fully doped PPy, respectively[50]

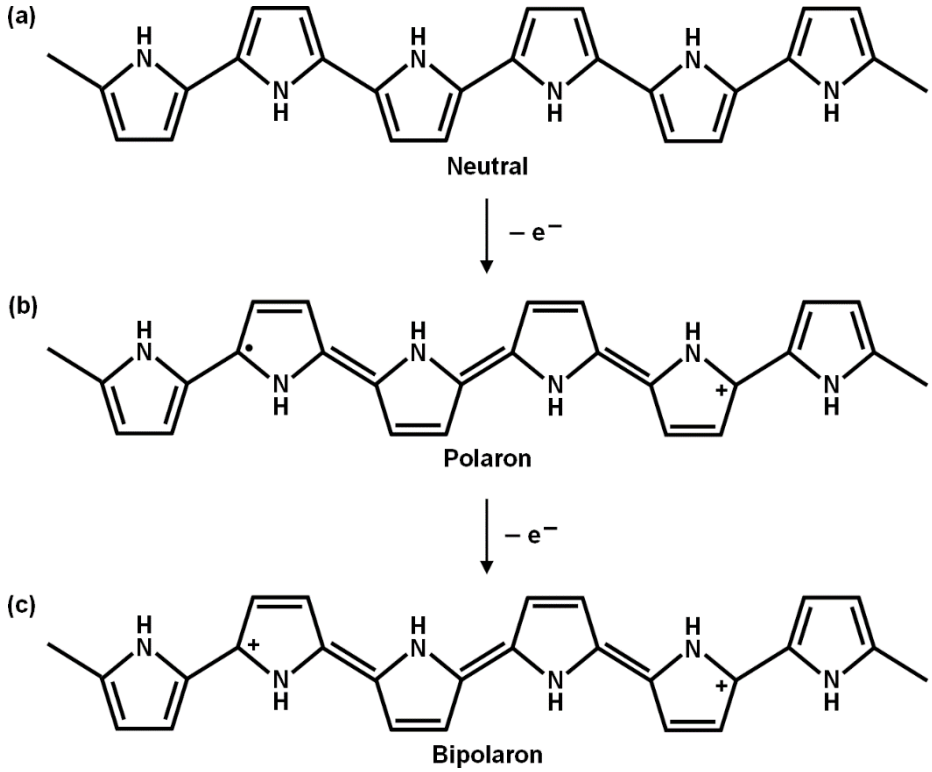

Figure 6. Structure for (a) neutral, (b) polaron, (c) bipolaron PPy, respectively[50]

1.1.4 Sensor applications

Sensor is a part of an electronic device, module, or subsystem that is to detect the changes or stimuli in its environment and sends the information to other electronic equipments using electrical signals.[51] With the advances in technology, various electronic devices are becoming more automated, and sensors are expected to become more compct and to play an important role in such fields as electic automobiles, space engineering, and robotics.

The sensors can be classified in to various categories according to the analytes to be sensed such as optical, acoustic, thermal, chemical, bio, pressure and so on. Among various sensors, chemical sensors and biosensors are very important research areas in that they are directly related to human life, for example disease diagnosis, terror preventions, pollution monitoring.[52-55]

In general, chemical sensors repond to and proved information about the chemical compostion of a substance or a specific chemical. On the other hand, bio sensor is an anlytical device which detect the biological analytes such as tissue, microorganisms, organelles, cell receptors, enzymes, antibodies, and proteins.

There are several factors that require high performance sensors:

1)high sensitivity to target analyte; 2)selectivity to target anlyte; 3)fast response/recovery time; 4)low operating temperature; and 5)durability.[56, 57]

In order to meet these demands, sensor transducers must exhibit high surface area, activity, and conductivity properties, and many studies have been carried out to apply nanomaterial as transducer materials.[58]

1.1.4.1 Chemical Sensor

Chemical and Gas sensors play a key roles in public and domestic safety, industrial applications and environmental pollution monitoring.[42, 59-61] Toxic and explosive gases can be used as chemical weapons in warfare and terrorist acts; therefore, detection of these gases has become one of the most important technologies.[62] Within the area of chemical sensors, resitive chemical sensor (i.e., chemiresistive sensor) is the most attractive system due to its simple operation, low production cost, miniaturation, and relatively high sensitivity.[58, 63]

A typical resistive sensor contains an active layer, the conductivity of which is highly sensitive to the target gasses. The mechanism of these sensor is to directly change the resistnace of the active layer through the change of the electorn withdrawing or donating on the surface of the sensor. Therefore, a major objective in resistive sensor research is to develop a high-performance, high-stability sensing material that can function at room temperature (**Figure 7**).[64, 65]

In generally, metal oxide semiconductor has been considered as a sensing material for broad spectrum of specaies, such as hydrogen sulfide (H_2S), hydrogen (H_2), nitrogen dioxide (NO_2), ammonia (NH_3),

ethanol, carbon dioxide (CO_2) and so on. However, sensors based metal oxide semiconductor requreis a high operating temperature to detect the toxic gasses and vapors. Meanwhile, organic-based sensors based on conducting polymer have fast response/recovery times at room temperature. However, issues related to the poor stability of organic materials hider their use in gas sensor applications. The use of hybrid materials of these two classes of materials may result in improved gas sensors that more efficient at room temperature.[42]

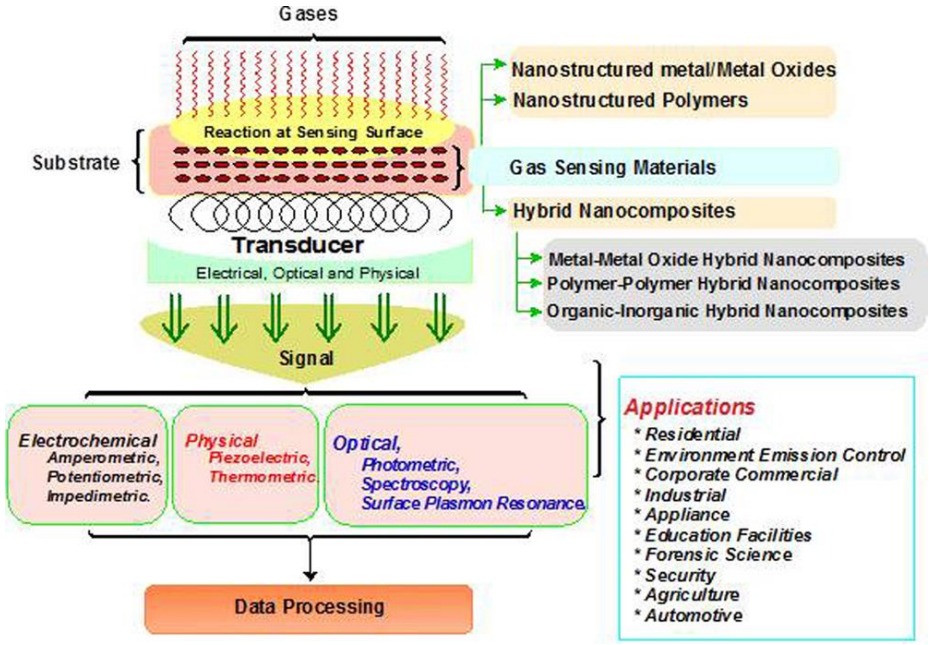

Figure 7. Schematic of gas sensor fabrication techniques[43]

1.1.4.1.1 DMMP gas sensor

Toxic and harzadous gasses can be used as a chemical weapon to produce numerous victims in warfare and terrorist acts; for example, gas terrorism in the Tokyo subway in 1995 caused 13 casulties and wounded about 5000 people, and the gases used are organophosphorous compounds that paralyze the organs of the human body and are generally colorless and odorless chemicals. These organophosphorous compounds such as sarin, soman, tabun, and VX, are the most dangerous, which inhibit the enzyme cholinesterase by forming covalent bonds with a serine residue at the active site of the enzyme.[66, 67] Therefore, detection of these gases has become one of the most important technologies. However, these organophosphorous compounds are very lethal to the human body, there is a great limitation in direct application to gas sensor in air. Thus, instead of detecting directly these organophosphorous compounds, sensors must be fabricated using a simulants for nerve agents that have similar chemical structure and the sensing mechanism.[62]

Among the simulants, dimethyl metahphosphonate (DMMP) has a similar chemical structure to sarin, and can be directly for sensor performance test in air because it shares the same sensing mechanism.

Varous types of sensors such as those based on colorimetric assays, gas choromatography, mass spectroscopy, enzymetric assays and atomic emission detection have been designed to detect DMMP.[68-72] However, these approaches still have limitations such as low sensitivities, slow response/recovery times, complex operation, and high costs.

1.1.4.2 Bio sensor.

Sensors which detect analytes thanks to a biological component, such as cells, protein, nucleic acid or biomimetic polymers, are referred to as biosensor in biotechnology and biomedicine.[73] The biological component can react selectively with the target analyte, resulting in chemical structural or electrical changes. This changes lead to a physical change in the surface of the tranducer binded with it, allowing the target to respond.[74, 75] Biosensors based on nanomaterials as transducer have been developed for detecting ultra low concentration target anaylte in femto- and pico- level. These sensors are very important topics that can be applied to various fileds such as medical and diagnosis.

Biosensors can be classified by their biotransducer type for example, electrochemical, field effect transistor (FET), optical, electronic, piezoelectric, fluorescent, and so on.[76]

The electrochemical sensor is a commercially and researcheally studied sensor system due to their simple mechanism and fast response. Currently, this sensor system is usally used as a glucose sensor. Typical electrochemical sensors immobilize enzymes on the surface of the transducer and detect signal changes thorugh a catalytic

activation process.[77] In recent year, various kind of enzymes other than glucose have been applied to detect a target substance. The liquid electrolyte gated FET type sensor is a sensor sysmte with great potential owing to its high performance current amplification and sustaingng an enhanced signal-to-noise (S/N) ratio.[78, 79] In general, this type sensor is composed of gold electode, transducer material, and target sensitive receptor. To enhance the sensing performance, transducer materials with high surface area, conductivity and orientation have been studied. 1D nanomaterials have great advantage that the can be used as building blocks for FET sensor.[80]

1.1.4.2.1 Glucose sensor

Diabetes mellitus, commonly referred to as diabetes, is a metabolic disorder that affects many people worldwide and is a symptom of persistent high blood sugar levels.[81-83] Because diabetes continues to cause divers complications such as cardiovascular disease, stroke, chronic kidney disease, foot ulcers, and damage to the eyes, it is important to manage the blood sugar levels.[84, 85]

Therefore, accurate blood sugar measurement tehchnique is essential for diabetes management. Various methods have been studied for the development of these sensors such as electrochemical (amperometry, potentiometry), and optical (Raman, infrared spectroscopy, and surface plasmon resomance).[86-89] Among the methods, the electrochemical sensor has a simple sensor system structure, high sensitivity, and reliability.[90-93]

In recent years, nanomaterials are applied to electrochemical sensor as transducer in order to obtatin ultra-low detection level and reliability.[90]

1.1.4.2.2 Platelet-derived growth factor (PDGF) sensor

Platelet-derived growth factor (PDGF) is a protein that regulates cell growth and division. Moreover, over concnetration of PDGF associated with several human disorders such as pulmonary hypertension, atherosclerosis, balloon injury-induced restenosis, organ fibrosis, and tumorigenesis.[94-99] Particluarly, concnetration of PDGFs dramatic increased at diseased vessels compare to normal vessels. PDGF are composed of two different types of monomers, A and B chains (PDGF-AA, PDGF-AB, and PDGF-BB). Among them, PDGF-BB that is oncogene protein is often overexpressed in human malignant tumors and is known as a potential protein marker for cancer diagnosis.[99, 100] To detect PFGF-BB, there have been conducted several appraoches using fluorescence and electrochemistry methods.[101-107] In fluorescence-based PDGF detection techniques, fluorophore-labeled aptamers have been used to signal binding by monitoring changes in fluorescence intensity through energy transfer. However, the precise target-binding sites and conformational changes in the aptamers are generally unknown. Additionally, conjugation of a fluorophore to an aptamer may weaken the affinity of the aptamer for its ligand. For electrochemistry-based detection using redox reactions,

the electrodes are limited to conductive materials, with different linkers used to attach the aptamer to the electrode surface (typically gold), and there is rapid degradation over time.

1.2 Objectives and Outlines

1.2.1 Objectives

The aim of this dissertation is proposing novel method to fabricate electrospun 1D composite nanomaterials for highly sensitive sensor application. Various condition contolled 1D composite nanomaterials such as porosity, composition, and shape were introduced to manufacture the sensor electrode. To achieve this aim, various polymers, solvents, and metal oxide precursors were mixed and applied to electrospinning. These as-prepared 1D composite nanomaterials applied to several chemical/bio sensor applicatios such as glucose, DMMP, and platelet derived growth factor (PDGF), respectively.

1.2.2 Outlines

This dissertation focused on the fabrication of electrospun 1D nanostructured composite materials and their applications in sensor field. This dissertation involves the following subtopic:

I. Fabrication of a One-dimensional cobalt oxide NPs embedded multichannel carbon for glucose sensor

I-1. Fabrication of Multichannel Carbon nanofiber and Cobalt oxide NPs embedded Multichannel Carbon nano fiber.

I-2. Application for glucose sensor

II. Fabrication of a One-dimensional Tube-in-tube Polypyrrole/Tin oxide Structure for Highly Sensitive DMMP Sensor Applications

II-1. Fabrication of complex tube in tube composite structure using electrospinning

II-2. Application for DMMP gas sensor

III. Fabrication of One-dimensional nano-nodule decorated Carbon Nanofiber for a Highly Sensitive and Selective Platelet-Derived Growth Factor Biosensor

III-1. Fabrication of Metal oxide nano nodule decorated ultrathin carbon nanofiber

III-2. Application for Platelet Derived Growth Factor (PDGF) sensor

2. Experimental Details

2.1 Fabrication of a One-dimensional cobalt oxide NPs embedded multichannel carbon nanofibers for glucose sensor

2.1.1 Materials

Poly(acrylonitrile) (PAN, Mw = 150,000), poly(methyl methacrylate) (PMMA, MW = 350,000), cobalt (Ⅱ) acetate and N,N-dimethylformamide (DMF) were purchased from Sigma−Aldrich and used without further purification.

2.1.2 Fabrication of MCNFs

A PAN solution was prepared by dissolving PAN (10 g) in DMF (90 g) at 60℃ for 2 h with vigorous stirring. Then, PMMA solution was prepared by dissolving 7 g of PMMA in 93 g of DMF at 50 ℃ for 1 h. Then, PAN and PMMA solution were mixed at room temperature for 30 min. The resulting viscous polymer solution was electrospun using a single-nozzle electrospinning at a flow rate of 15 μL min^{-1}, with an

applied voltage of 15 kV. The nanofiber were stabilized at 300℃ for 4h and heated in flowing argon at 900℃ 2h for carbonization.

2.1.3 Fabrication of C_MCNFs

Then, cobalt (Ⅱ) acetate was mixed with the PMMA solution at 70 °C for 3 h. Then, the resulting red viscous solution was mixed with 10wt% of PAN solution at room temperature. The resulting viscous polymer solution was injected from a syringe into the electrospinning device. The collected nanofiber was treated by O_2 plasma for 5 min. After that, the nanofiber were stabilized at 300 ℃ for 4 h and heated in flowing argon at 900 ℃ 2 h for carbonization.

2.1.4 Electrochemical measurement

To construct a C_MCNF active material for an electrochemical sensor, the C-MCNF was dispersed in distilled water using ultrasonicator. Then, this homogeneous solution was drop casted on the glassy carbon electrode (GCE) and vacuum dried for 12 h. The sensing properties of samples were measured using a three electrode cell system consisting of 0.1 M NaOH, an Ag/AgCl reference

electrode, and a platinum (Pt) counter electrode. All electrochemical sensing properties were obtained by Zahner Elektrik IM6 analyzer.

2.1.5 Characterization

Transmission electron microscopy (TEM) images were acquired by a JEM-2100 (JEOL Ltd., Japan) installed at the National Center for Inter-university Research Facilities (NCIRF) at Seoul National University. HR-TEM images were obtained with Tecnai F20 microscopes. A JEOL 6700 instrument was used for the FE-SEM measurements. XRD and XPS were performed using M18XHF SRA (MAC Science Co.) and Kratos AXIS-His instruments, respectively. Fourier transform-infrared (FT-IR) data were obtained with a Thermo Scientific Nicolet 6700 FT-IR spectrophotometer.

2.2 Fabrication of a One-dimensional Tube-in-tube Polypyrrole/Tin oxide Structure for Highly Sensitive DMMP Sensor Applications

2.2.1 Materials

Poly(vinylpyrrolidone) (PVP, Mw = 1,300,000), tin chloride dihydrate, iron (III) chloride, pyrrole and N,N- dimethylformamide (DMF) were purchased from Sigma–Aldrich and used without further purification.

2.2.2 Fabrication of the tube-in-tube SnO_2

A PVP solution was prepared by dissolving PVP (0.5 g) in DMF (2.5 g) at room temperature for 2 h with vigorous stirring. Then, a solution of $SnCl_2 \cdot 2H_2O$ (0.2 g) in ethanol (2.5 g) was mixed with the prepared PVP solution at room temperature for 3 h. The resulting transparent viscous hybrid solution was injected from a syringe into the electrospinning device. The diameter of the needle was 0.1 mm, and the needle was connected to the positive terminal of the power supply. Electrospinning was conducted at a flow rate of 8 μL min^{-1} at an

applied voltage of 15 kV. The electrospun polymer nanofiber was heated at 600 ℃ at a heating rate of 5 ℃ min^{-1}.

2.2.3 Fabrication of the PPy@SnO_2 tube-in-tube structure

VDP was used to coat the tube-in-tube SnO_2 with polypyrrole. First, tube-in-tube SnO_2 (0.1 g) was stirred in 20 mL of aqueous ferric chloride ($FeCl_3$) solution (10 wt%) at 60 ℃ for 3 h. Then, the soaked tube-in-tube SnO_2 was washed with deionized water several times and dried in a vacuum oven for 5 h. The dried tube-in-tube PPy@SnO_2 was then exposed to pyrrole monomer (0.1 mmol) inside the VDP vacuum chamber and finally transferred into the 120 ℃ oven for 30 min.

2.2.4 Characterization of the PPy@SnO_2 tube-in-tube structure

Transmission electron microscopy (TEM) images were acquired by a JEM-2100 (JEOL Ltd., Japan) installed at the National Center for Inter-university Research Facilities (NCIRF) at Seoul National University. HR-TEM images were obtained with Tecnai F20 microscopes. A JEOL 6700 instrument was used for the FE-SEM, EDX spectrum and EDS mapping measurements. XRD and XPS were

performed using M18XHF SRA (MAC Science Co.) and Kratos AXIS-His instruments, respectively. Fourier transform-infrared (FT-IR) data were obtained with a Thermo Scientific Nicolet 6700 FT-IR spectrophotometer. Brunauer–Emmett–Teller (BET) surface area measurements were obtained using ASAP2010 (Micrometrics).

2.2.5 Electrical sensitivity measurements of the tube-in-tube PPy@SnO_2

The resistance changes of the tube-in-tube PPy@SnO_2 were monitored with a source meter connected to a computer. A mass flow controller (MFC, KNH Instruments) was used to expose the sensor electrode to various DMMP gas concentrations (0.01 ppb to 100 ppm), and the resistance values were recorded in real-time. The tube-in-tube PPy@SnO_2 was allowed to interact with the DMMP gas over several minutes. Then the vapor was replaced with nitrogen gas to remove DMMP molecules attached to the backbone of the PPy@SnO_2 tube-in-tube structure.

2.3 Fabrication of One-dimensional nano-nodule decorated Carbon Nanofiber for a Highly Sensitive and Selective Platelet-Derived Growth Factor Biosensor

2.3.1 Materials

Poly(acrylonitrile) (PAN, Mw = 150,000), poly(vinylpyrrolidone) (PVP, Mw = 1,300,000), zinc acetate (ZnAc2), pyrrole, and pyrrole-3-carboxylic acid were purchased from Sigma. The platelet-derived growth factor-B (PDGF-B) binding aptamer was from Bioneer Co. (Dajeon Korea). The PDGF-B binding aptamer was modified at the 5' terminus with an amine group, and its sequence was as follows: 5' NH2 CAG GCT ACG GCA CGT AGA GCA TCA CCA TGA TCC TG 3'. PDGF-BB, PDGF-AB, PDGF-AA, adenosine, triphosphate (ATP), and calmodulin (Cal) were purchased from Aldrich as analyte materials.

2.3.2 Fabrication of MCNFs

Metal oxide-decorated CNFs (MCNFs) were fabricated as starting materials. PAN solutions were prepared by dissolving 1.0 g PAN in 10 mL DMF at 80–90 °C for 1 h with vigorous stirring. PVP solutions were prepared by dissolving 1 g PVP and 0.3 g $ZnAc_2$ in 10 mL DMF

at 50°C for 2 h with vigorous stirring. Then, the PAN and PVP solutions were mixed at 80–90°C for 3 h. The resulting viscous hybrid solution was injected from syringe (10 mL) using a single-nozzle co-electrospinning method. The syringe for electrospinning was filled with hybrid solution. The electrospinning needle diameter was 30 guage (OD:0.40 mm, ID:0.20 mm). The needle was connected to the positive terminal of a power supply. The voltage was conducted at 17 kV, and the solution was delivered to the syringe by the syringe pump. The flow rate of the syringe pump was fixed at 10 μL/min. The distance of tip to collector was fixed at 15 cm. The electrospun NFs were heated at 400 °C for 2 h to calcine and then heated in flowing argon gas at 800 °C for 1 h for carbonization.

2.3.3 Fabrication of CPMCNFs

Carboxylated polypyrrole-coated hybrid carbon nanofibers (CPMCNFs) were prepared by vapor deposition polymerization (VDP) of the MCNFs. First, MCNFs 0.5 g were soaked in 10mL ethanolic ferric chloride ($FeCl_3$) solution (0.1M) for 5 min. Then, the soaked MCNFs were dried in a vacuum oven for 4 h and inserted inside the reactor with 0.18 mmol pyrrole-3-carboxylic acid. The internal pressure

was then reduced to 10^{-2} torr, and the reactor was moved into the 60°C oven for 10 min. After VDP process, approximately 0.5 g CPMCNFs was gained with little loss.

2.3.4 Fabrication of the CPB-Apt FET sensor

To construct the CPMCNFs-aptamer FET sensor, the IDA substrate was first treated with 5 wt% aqueous amino silane (3 aminopropyltrime-thoxysilane, APS) for 6 h to introduce amino groups on the IDA substrate. It was then exposed to a mixture of 0.1 wt% aqueous CPMCNFs solution (40 μL) and 1 wt% aqueous 4-(4,6-dimethoxy-1,3,5-triazin-2-yl)-4-methylmorpholinium chloride (DMT-MM, 40 μL) solution for 12 h. The resulting CPMCNFs-immobilized substrate was rinsed with distilled water. Subsequently, the coupling reaction to attach the PDGF-B binding aptamer to the CPMCNF surface was carried out using a mixture of PDGF-B binding aptamer and 1 wt% aqueous DMT-MM (40 μL) for 12 h. Then, the platform substrate was rinsed with distilled water and dried at room temperature.

2.3.5 Characterization

TEM and HRTEM images were obtained with JEOL JEM-200CX

and JEOL JEM-3010 microscopes, respectively. A JEOL 6700 instrument was used to obtain FE SEM images. IR data were obtained with a Bomem MB 100 (Quebec, Canada) in absorption mode.

2.3.6 Electrical measurements with the CPB-Apt sensor

All electrical measurements were conducted with a Keithley 2612A source meter and probe station (MS TECH, model 4000) and a Wonatech WBCS 3000 potentiostat. A chamber (300-μL volume) was designed and used for solution-based measurements. The current change was normalized as

$$\left[\frac{\Delta I}{I_0}\right]_{SD}(\%) = \frac{(I - I_0)}{I_0} \times 100 \qquad (1)$$

Where, I_0 was the initial current, and I was the measured real-time current.

3. Results and Discussions

3.1. Fabrication of a One-dimensional cobalt oxide NPs embedded multichannel carbon nanofibers for glucose sensor

3.1.1 Fabrication of Materials

3.1.1.1 Fabrication of MCNF

Figure 8 illustrates the steps of the multichannel carbon nanofiber (MCNF) fabrication process. Single-nozzle co-electrospinning was conducted using a hybrid polymer solution composed of two polymer solutions: poly(acrylonitrile) (PAN) and poly(methyl methacrylate) (PMMA).[108] Because of surface tension, two immiscible polymer solutions separated into a continuous PAN phase and a discontinuous PMMA phase, as confirmed by optical microscopy image (inset of **Figure 8**). The PMMA solutions with different concentrations (5 wt%, 7 wt% and 9 wt%) were applied to control morphology. Hereafter, the following notation is used to denote the concentration of PMMA for the MCNF samples: MCNF_5 for 5 wt%, MCNF_7 for 7 wt% and MCNF_9 for 9 wt%. The resulting phase-separated hybrid polymer nanofiber showed no aggregation, as confirmed by field-emission

scanning electron microscopy (FE-SEM) image (**Figure 9a**). Transmission electron microscopy (TEM) revealed that the continuous PAN solution made up the main walls of the nanofiber, with the discontinuous PMMA solution forming the inner parts of the fiber (**Figure 9b**). In the stabilization and thermal-treatment conversion step, the phase-separated hybrid polymer nanofiber was first stabilized under controlled air conditions at 300 ℃ for 4 h. This stabilization step was essential to prepare the nanofiber for a high-temperature heat treatment.[27] The stabilized phase-separated polymer nanofiber was treated in an inert atmosphere at 900 ℃, in which the continuous PAN phase transformed into carbon-like conventional PAN-based carbon fibers.[23, 25] However, the discontinuous PMMA phase that composed the inner portion of the phase-separated polymer nanofiber easily decomposed without carbon residue formation. **Figure 9c** shows an FE-SEM image of a multichannel carbon nanofiber (MCNF_7), which maintained a fibrous morphology following thermal treatment; the hollow multichannel in the MCNF_7 was clearly visible in cross-sectional FE-SEM image (**Figure 9d**). A TEM image of a MCNF showed that the long hollow multichannel inner pores were well oriented along the fiber length; as a result, a hollow

multichannel was created in the MCNF_7. On the other hand, at 5 wt%, a small pore is formed due to insufficient concentration to form an innerchannel, and at 9 wt%, an irregular channel is formed due to a dense concentration (**Figure 10**). Therefore, the concentration of PMMA was fixed at 7 wt%.

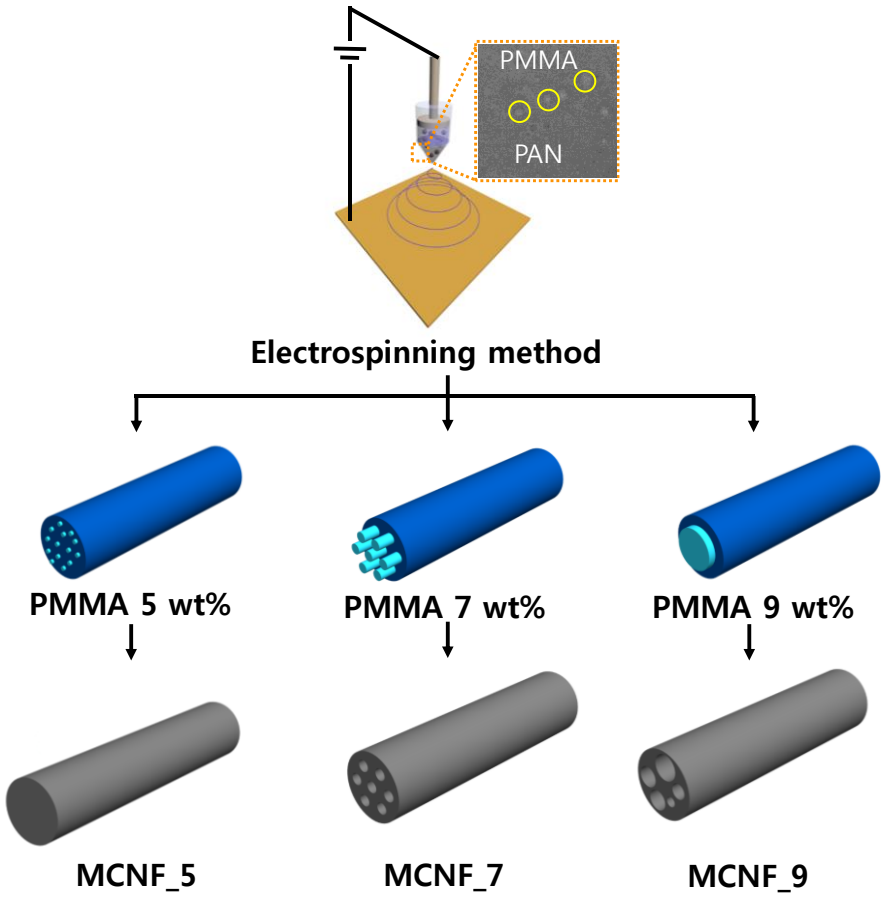

Figure 8. Schematic diagram illustrating the fabrication procedure of multichannel carbon nanofibers (MCNFs) (inset is optical microscopy of immisible polymer solution)

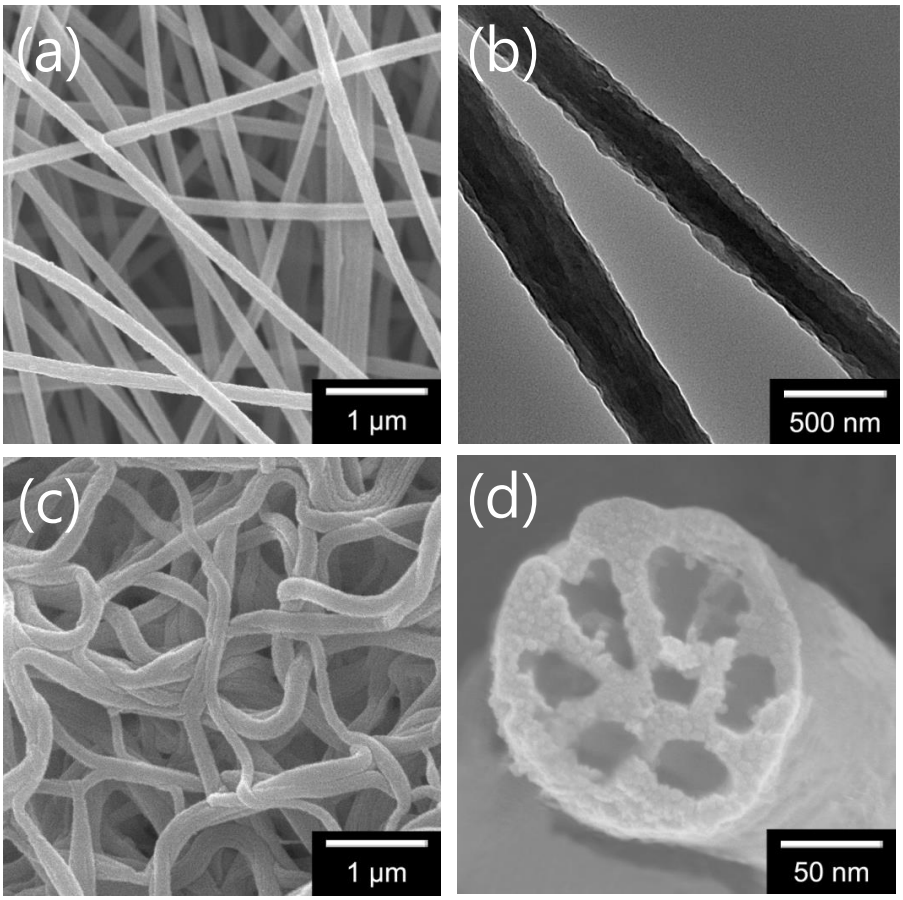

Figure 9. (a) Field-emission scanning electron microscopy (FE-SEM) and (b) Transmission electron microscopy (TEM) images of phase separated polymer nanofiber. (c) Low- and (d) high-resolution cross sectional FE-SEM image of multichannel carbon nanofibers

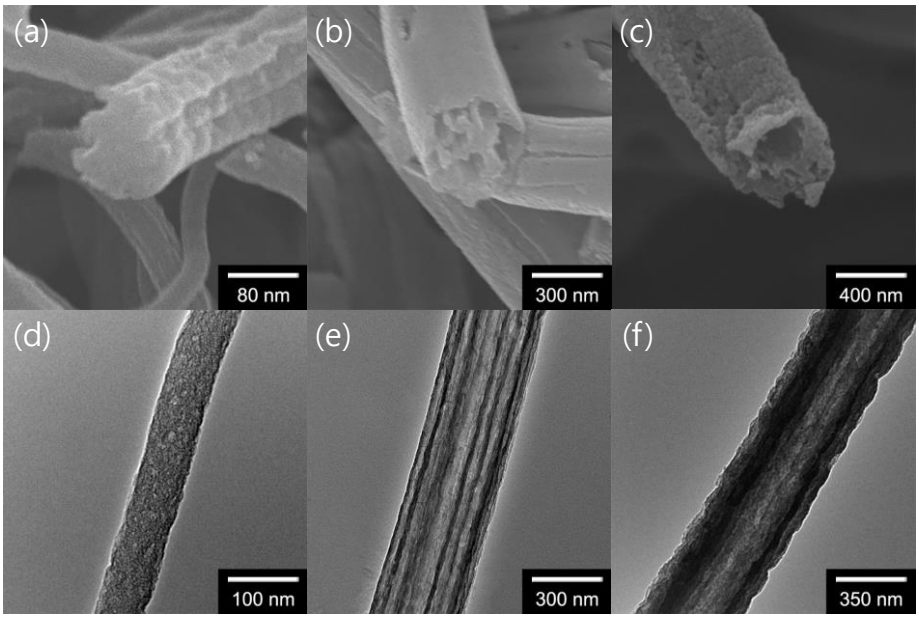

Figure 10. (a, d) Transmission electron microscopy (TEM) and scanning electron microscopy (SEM) images of the MCNF_5. (b, e) TEM and SEM images of the MCNF_7. (c, f) TEM and SEM images of the MCNF_9

3.1.1.2 Fabrication of C_MCNFs

Figure 11 describes a method for fabrication of cobalt oxide nanoparticles (NPs) embedded multichannel carbon nanofibers (MCNFs). To uniformly disperse the NPs, 0.05 g of cobalt acetate as cobalt oxide precursor was mixed with 7 wt% of PMMA solution at 60 ℃ with vigorous stirring. Also, to confirm the dispersion condtion, control experiment with different mass of cobalt acetate (0.01 g, 0.1 g, and 0.2 g) was performed. After that, PAN solution which is a carbon precursor was put into the cobalt acetate contained PMMA solution. This prepared solution was injected into an electrospinning syringe to conduct electrospnning to obtain a nanofibers. Due to different surface tension of the two polymer solutions, a phase separated nanofibers are formed which have a PMMA inner channel. Then, the nanofibers were treated with oxygen plasma for 5 minutes for even generation of Cobalt oxide NPs. Thereafter, final cobalt oxide NPs embedded MCNFs (C_MCNFs) are produced through a heat treatment in two step. Firstly, it undergoes thermal stabilization at 300 ℃ in air condition.[24] In this process, the cyano group in the PAN is cross-linked in the case of conventional PAN based carbon fibers. At this time, the cobalt ions belonging to PMMA are bonded with oxygen to form cobalt oxide.

Without plasma treatment, the surface of the final C_MCNFs collapses due to lack of oxygen on the polymer structure. After thermal stabilization process, carbonization process was carried out in inert atmosphere at 900 ℃.

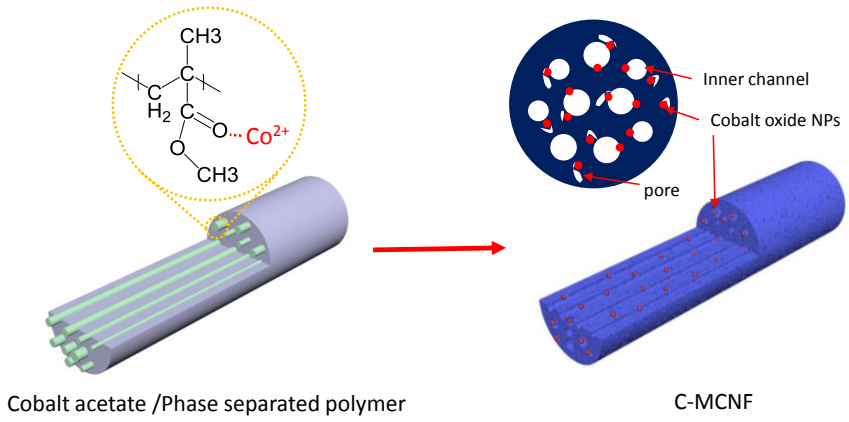

Figure 11. Schematic diagram of the sequential fabrication of the C-MCNFs

3.1.2 Characteirzations

3.1.2.1 Characterization of MCNFs

To determine the microstructure of MCNFs, XRD and Raman anaylsis were carried out. **Figure 12** exhibits the XRD patterns of the MCNFs with differnent PMMA contents (MCNF_5, MCNF_7, and MCNF_9). These patterns reveal broad and strong reflection at 2 θ of 24.5 °, which corresponds to the (002) planes of the graphite structure. In general, the three XRD patterns do not show any sinificant diffences because PMMA inner channel is thermal decomposed and does not signicantly affect the crystallinty

Raman spectroscopy also represent the microstructure of the MCNFs. The main two peaks of 1350cm^{-1} and 1590cm^{-1} are D band and G band, repectively, indicating disordered carbon and graphite (**Figure 13**).[23, 27] The ratio of the D and G bands (I_D/I_G) corresponds to the sp^3/sp^2 carbon ratio.[23, 27] This ratio represents the degree of graphitization of the carbon structure. The ratio of the three patterns tends to decrease slightly, but does not show significant difference. This reduction is due to the increase in the disordered morphology of the carbon structure as the amount of PMMA increases.

Figure 14 displays the nitrogen adsorption-desorption isotherm curves for the MCNFs with varying PMMA concentrations. The low relative pressure range ($0 < 0.2$ P/P_0) was attributable to the presence of micropores which originated from electrospun carbon nanofibers. Whereas additional adsorption for a high relative pressure (> 0.9 P/P_0) was observed for mesoporous MCNFs. The Barrett-Joyner-Halenda (BJH) pore size distribution of the MCNFs show a sharp peak at 2 nm, which is strongest at 7 wt% because the distribution of the pore is further increased as a uniform inner channel is formed (**Figure 15**).

Furthermore, the calculated-Brunauer-Emmett-Teller (BET) specific surface area value of MCNF_7 (335 m^2/g) was higher than that of the MCNF_5 (165 m^2/g) and MCNF_9 (277 m^2/g) owing to well organized hollow inner channlel.

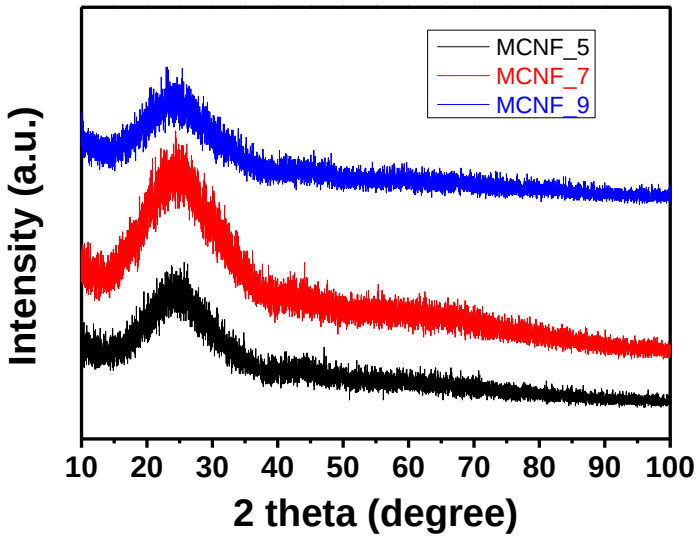

Figure 12. XRD patterns of MCNFs (black: MCNF_5; red: MCNF_7; blue: MCNF_9)

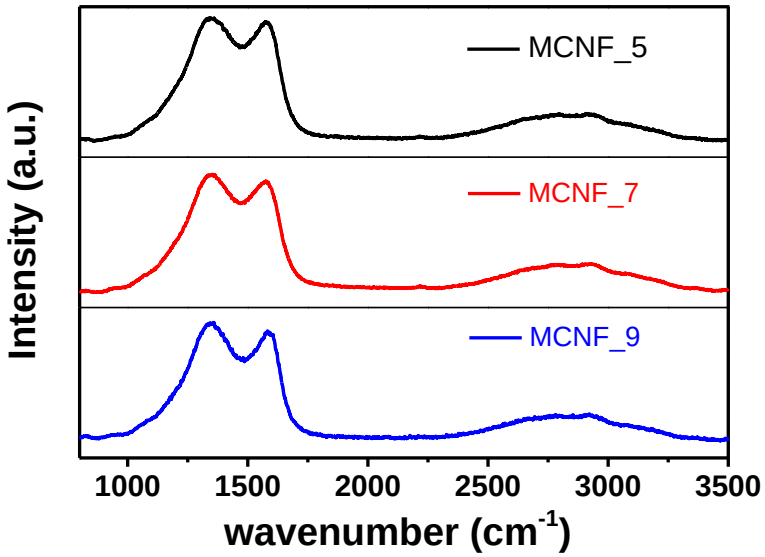

Figure 13. Raman spectroscopy of MCNFs (black: MCNF_5; red: MCNF_7; blue: MCNF_9)

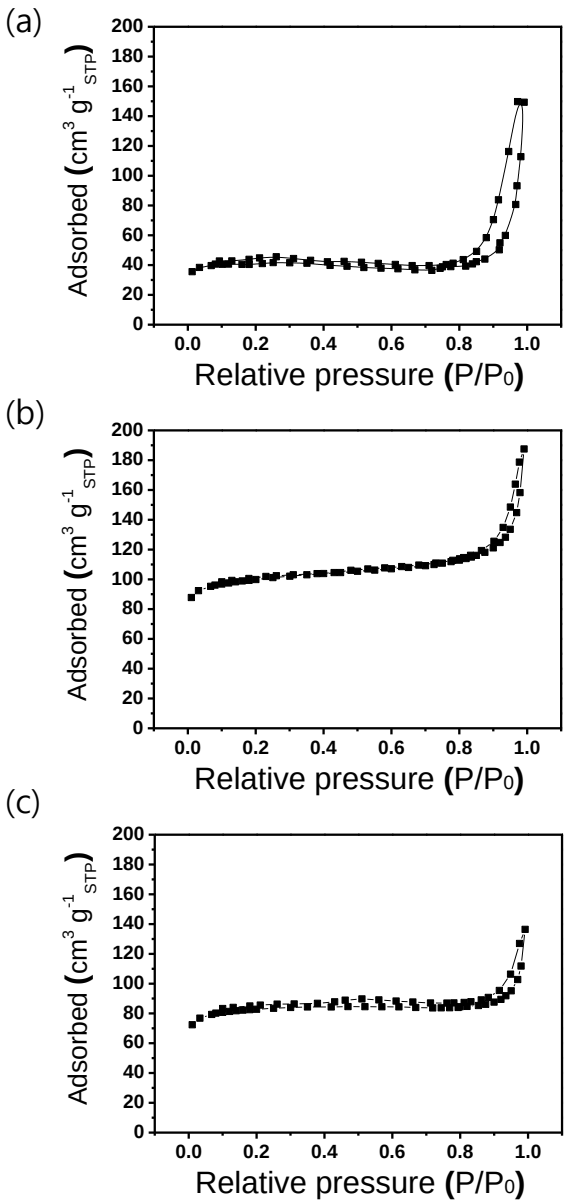

Figure 14. Nitrogen adsorption–desorption isotherm curves of (a) MCNF_5, (b) MCNF_7 and (c) MCNF_9

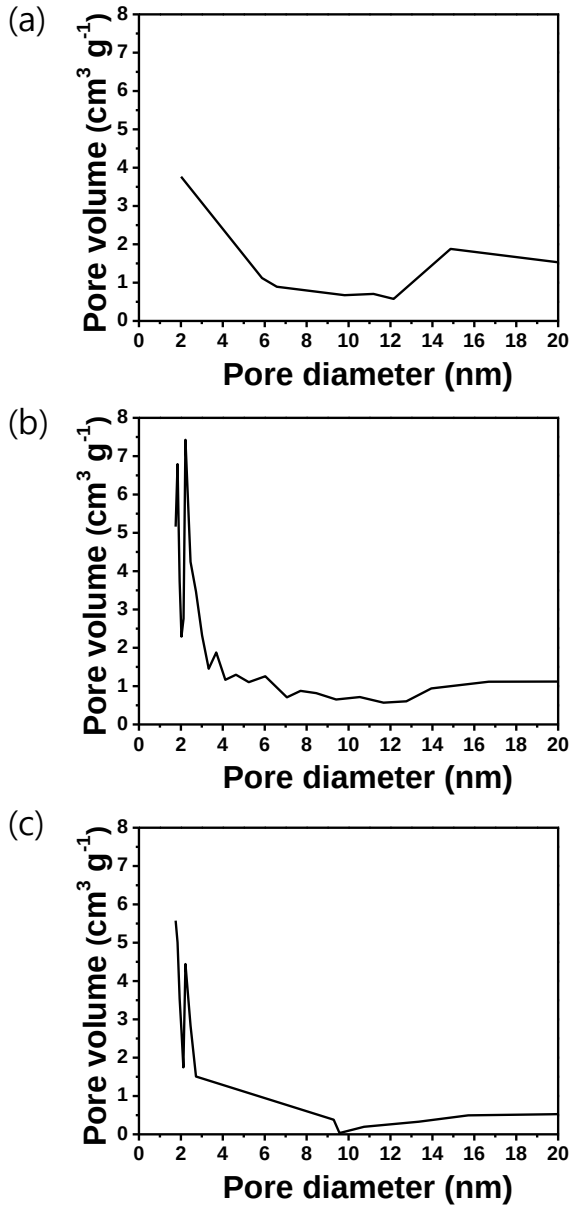

Figure 15. Barrett–Joyner–Halenda (BJH) pore-size distribution curves of (a) MCNF_5, (b) MCNF_7 and (c) MCNF_9

3.1.2.2 Characterizations of C_MCNFs

Figure 16a and **16b** exhibit a field-emission scanning electron microscopy (FE-SEM) images of the carbonized C_MCNFs with a diameter of 300 nm and hollow inner channel (30-50 nm). **Figure 16c** shows a transmission electron microscopy (TEM) image of the highly dispersed cobalt oxide NPs embedded MCNFs without any aggregation. The cobalt oxide NPs (ca. 10 ± 5 nm) were observed in the inner channel. Furthermore, C_MCNFs have small pores on the surface of the C_MCNFs about 5 ± 0.5 nm formed during cobalt oxidation (**Figure 16d** and **16e**). **Figure 16f** reveals a high resolution TEM (HR-TEM) image of the cobalt nanoparticle (ca 10 nm) with an interplanar spacing of 0.46 nm for the (111) plane of the lattice. In addition, control experiment with different mass of cobalt acetate (0.01, 0.1, 0.2g) results in **figure 17**. Hereater, the notation of the following notation is applied to denote the mass of cobalt acetate for the C_MCNF samples: C0.01_MCNF for 0.01 g, C0.05_MCNF for 0.05 g, C0.1_MCNF for 0.1 g and C0.2_MCNF for 0.2 g. The 1D morphology of the C_MCNFs maintained after heat treatment, as tracked by the high-angle annular dark field (HAADF)-scanning electron transmission microscopy (STEM)-electron enegy-loss

spectroscopy (EELS) and EELS elemental mapping. This spectroscopy confirm that the enrichment of cobalt oxide NPs in the inner channel of the C_MCNFs (**Figure 18**).

Figure 19 displays the x-ray diffraction (XRD) patterns of C_MCNFs with different amount of cobalt acetate. As the amount of cobalt acetate increase, peaks at 2 θ of 36.5 °, which correspond to the (311) were observed, and other peaks were not observed because the cobalt oxide NPs were too small (ca. 10nm), and existed inside the MCNFs.[40] C_MCNFs containing 0.2 g of cobalt acetate had an excessive amount of precursors, so that decomposition occurred, as could be confirmed by TEM. Therefore, this XRD pattern exhibits the typical face centered cubic structure of CO_3O_4 crystalline peaks at 2 theta = 31.2, 36.5, 44.7, 55.5, 59.2 and 65.1 ° corresponding to the (220), (311), (400), (422), (511), and (440), respectively.[40][37]

ATR-FTIR spectra of the C_MCNFs as shown in **Figure 20**. Two peaks at ~590 $cm^{-1}$and ~670 cm^{-1}, which are related to the stretching vibration mode of co_O bond and confirm the formation of Co_3O_4 structure. The band at 590 is characteristic of Co^{3+} vibration in the

octahedral hole, while band at 670cm^{-1} indicates CO^{2+} vibration in tetrahedral hole in the spinel lattice.[37]

Figure 21 shows the Raman spectroscopy with increasing the amount of cobalt acetate. Due to the cobalt oxide NPs, the peaks at 687cm^{-1} were observed corresponding to the A_{1g} modes of CO_3O_4. At the same time, G peaks were increased because the pores were formed on the surface of the carbon structure. As with the XRD results, 0.2 g reveals the original peaks at 194, 480, 525, 616, and 687 cm^{-1} corresponding to the cobalt oxide.[37, 40]

Figure 22 displays the nitrogen adsorption-desorption isotherm of C_MCNFs, which have type4 hysteresis originated from both of micropores (range: 0 < 0.2 P/P_0) and mesopores (range: > 0.8 P/P_0). The calculated-Brunauer-Emmett-Teller (BET) surface area values are 0.01 (331 m^2/g), 0.05 (488 m^2/g), and 0.1 (115 m^2/g) due to decomposition of innerchannel at 0.1 g. This is consistent with the result from microscopy images of C-MCNFs.

The Barrett-Joyner-Halenda (BJH) pore size distribution patterns, represented as a sharp peak at 2 nm, were ascribed to the pore of the C-MCNFs (**Figure 23**). As the cobalt ions are oxidized, an additional

micropores are generated, thus the pore gradually increases with increasing cobalt acetate.

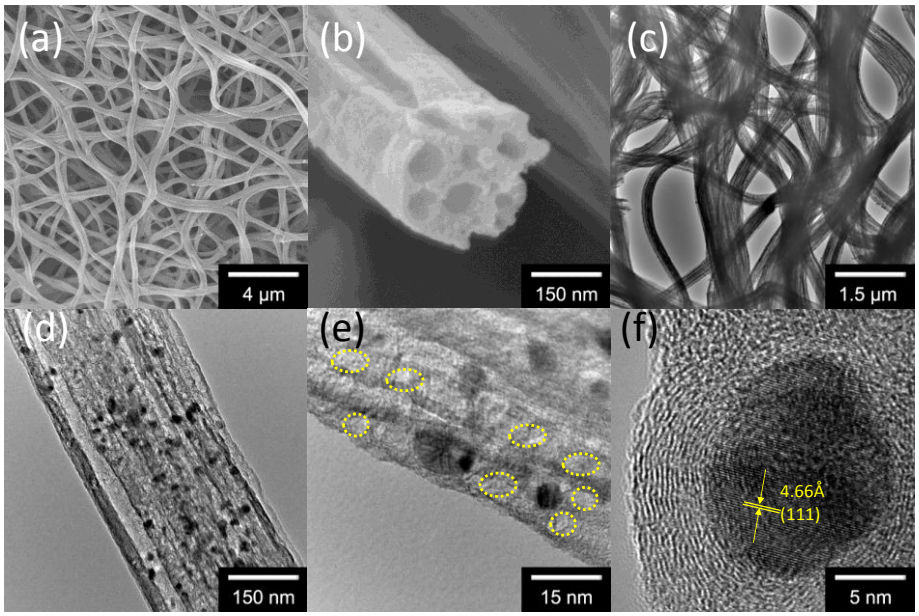

Figure 16. (a)Low-and (b)high resolution field-emission scanning electron microscopy(FE-SEM)images of the C0.05-MCNFs. (c)Low-, (d)mid- and (e)high magnification transmission electron microscopy (TEM) image of the C0.05-MCNF. (f)High resolution-TEM (HR-TEM)image of the cobalt nanoparticle

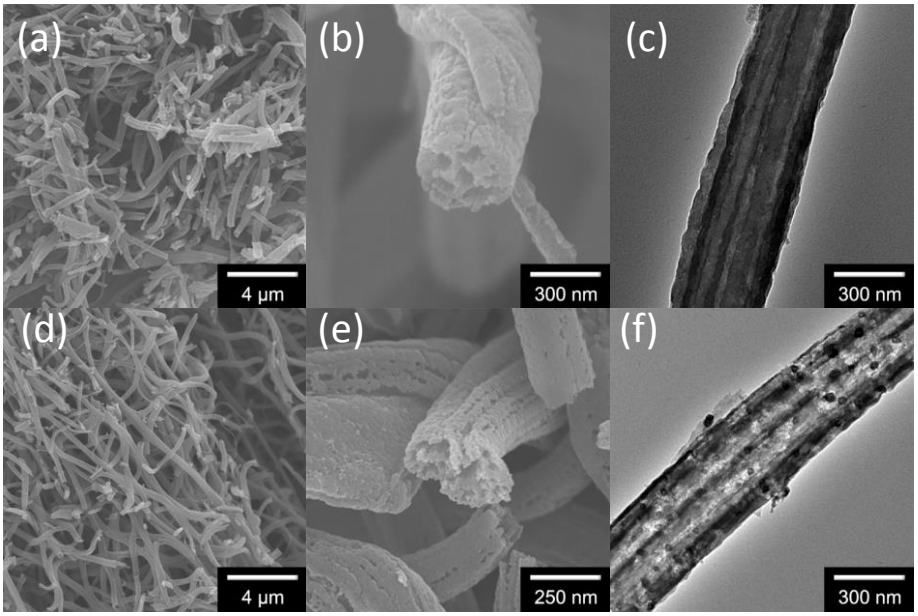

Figure 17. Field-emission scanning electron microscopy(FE-SEM)images of the C-MCNFs.(a)Low-and (b)High-resolution FE-SEM images of the C0.01-MCNF. (d)Low-and (e)high resolution FE-SEM images of the C0.1-MCNF. Transmission electron microscopy (TEM) image of the (c)C0.01-MCNF and (f)C0.1-MCNF

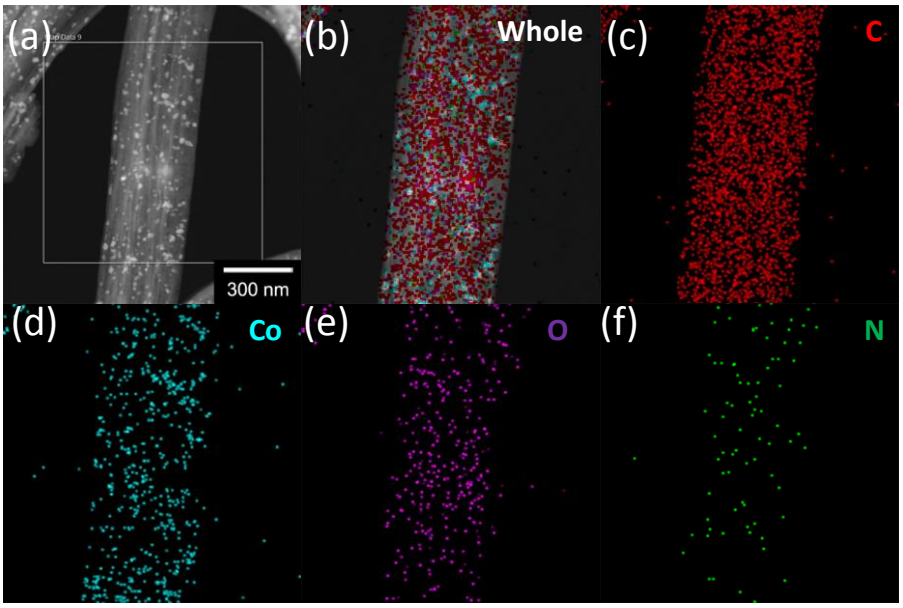

Figure 18. (a)High-angle annular dark field (HAADF)-scanning electron transmission microscopy (STEM)-electron enegy-loss spectroscopy (EELS) image of the C0.05-MCNF. EELS elemental mapping of C0.05-MCNF surface components indicating (b)whole, (c)carbon, (d)cobalt, (e)oxygen and (f)nitrogen

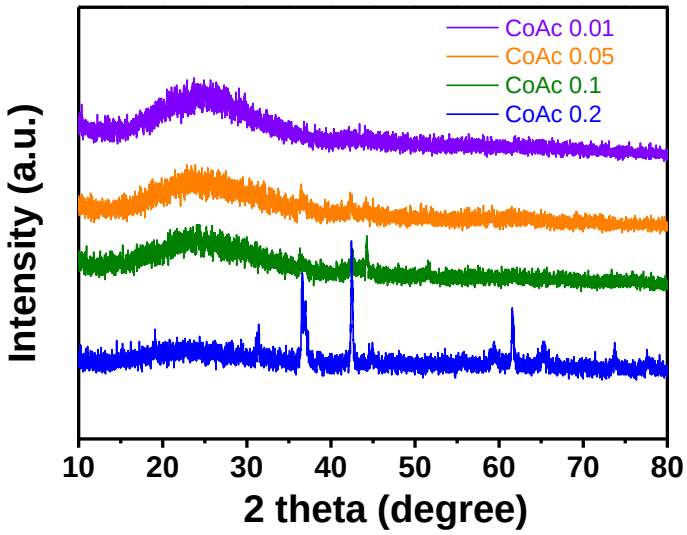

Figure 19. XRD patterns of C-MCNFs (green: C0.01-MCNF; orange: C0.05-MCNF; purple: C0.1-MCNF; Blue: C0.2-MCNF)

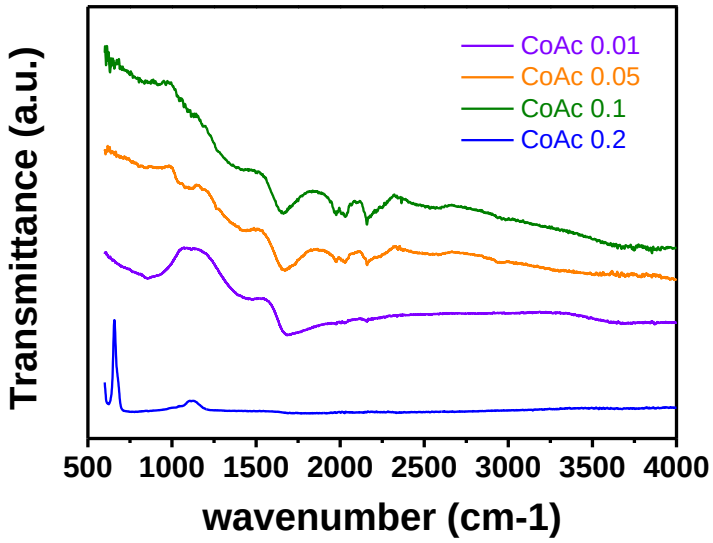

Figure 20. FT-IR spectra of C-MCNFs (green: C0.01-MCNF; orange: C0.05-MCNF; purple: C0.1-MCNF; Blue: C0.2-MCNF)

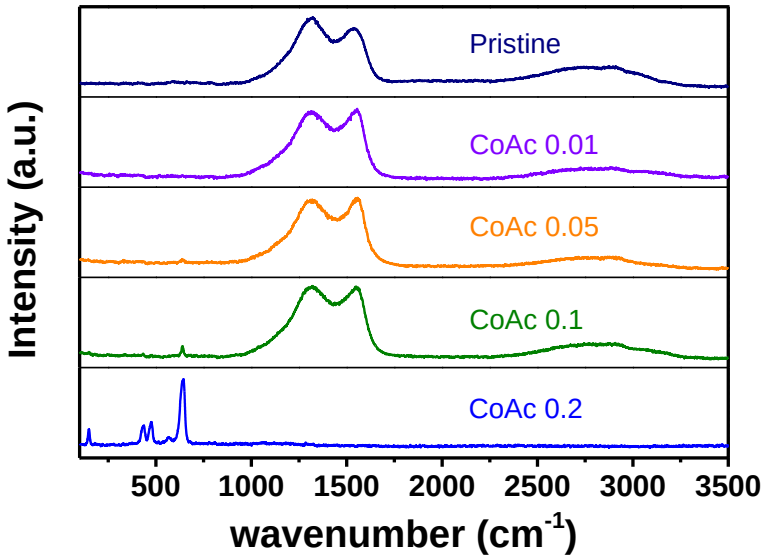

Figure 21. Raman spectroscopy of C-MCNFs (green: C0.01-MCNF; orange: C0.05-MCNF; purple: C0.1-MCNF; Blue: C0.2-MCNF)

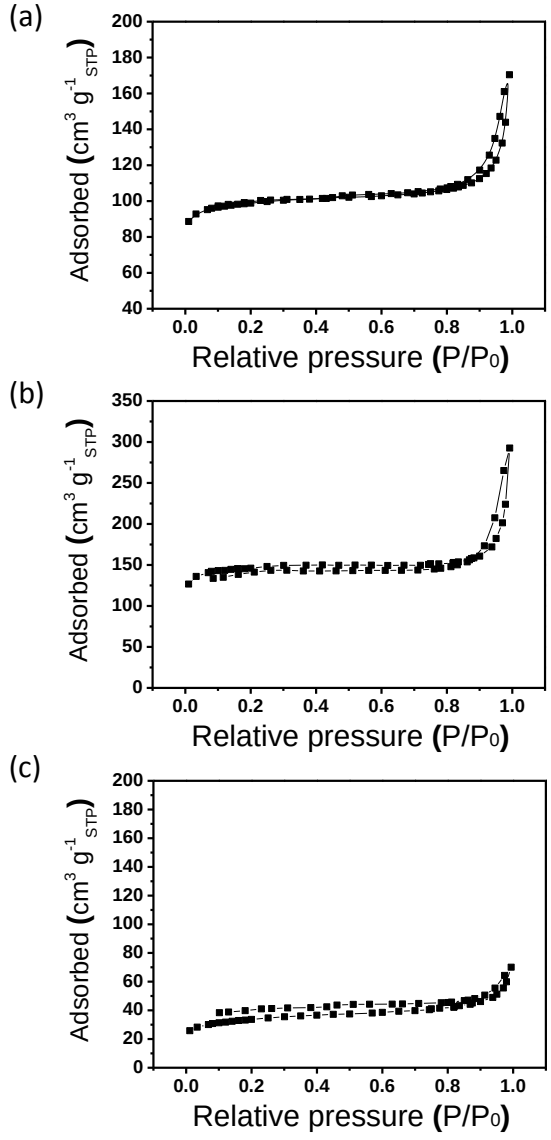

Figure 22. Nitrogen adsorption–desorption isotherm curves of (a)C0.01-MCNF, (b) C0.05-MCNF, and (c) C-0.1_MCNF

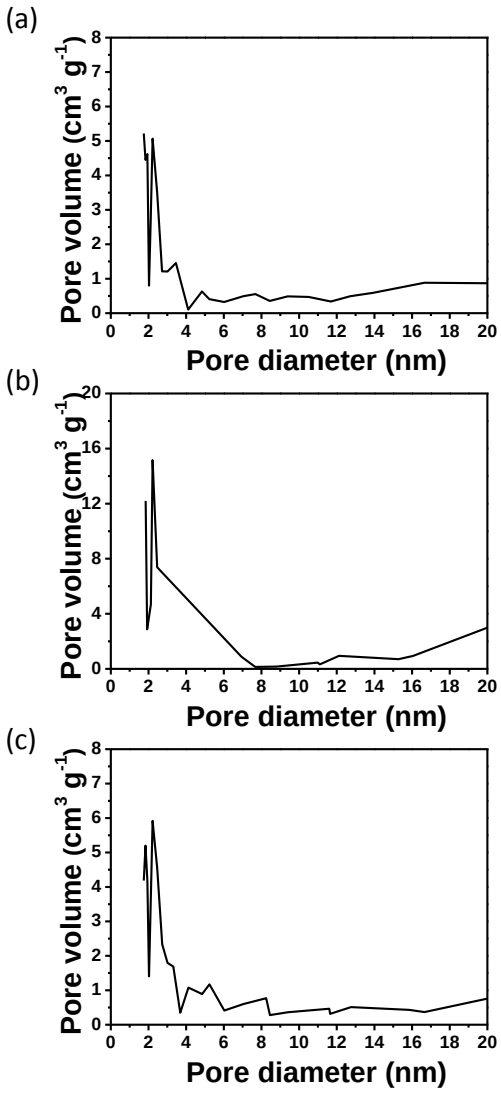

Figure 23. Barrett–Joyner–Halenda (BJH) pore-size distribution curves of (a)C0.01-MCNF, (b) C0.05-MCNF, and (c) C0.1_MCNF

3.1.2.3 Electrochemical sensing performance

To investigate the sensor applications of the C0.05_MCNF, the sample was evaluated with cyclic voltammetry (CV) measurement in three electrode system using a 0.1 M NaOH aqueous electrolyte solution. The CV curve of C0.05_MCNF reveals a reversible redox peak, which is the result of the phase change of cobalt oxide NPs. In addition, even when scan rated is gradually increased from 10 mV/s to 100 mV/s, it is confirmed that redox peak becomes even larger, but the shape of the CV is almost nonexistent (**Figure 24a**).

To explore the sensing performance, glucose diluted with PBS from 1 nM to 1M was added to confirm the change in the glucose concentrations (**Figure 24b**). As a result, the redox peak at 0.58 V increased with the addition of glucose. The mechanism of this result is as follows.[39]

$$Co(\text{Ⅲ}) + OH^- \rightarrow Co(\text{Ⅳ}) - (OH^-) + e^-$$

$$Co(\text{Ⅳ}) - (OH^-) + \text{glucose} \rightarrow Co(\text{Ⅲ}) + OH^- + \text{gluconolactone}$$

After that, an amperometric test was carried out at 0.58 V in order to investigate the change of the glucose concentration in real time (**Figure 25**). The non-enzyme C_MCNF based sensor exhibited a

rapid and sensitive response to the addition of glucose. In particular, the minimum detectable level (MDL) of this sensor is 1 nM, indicating that this sensor works very well without the enzyme.

In addition, the selectivity test was also conducted using ascorbic acid (AA), uric acid (UA), dopamine (DA) and sodium chloride (NaCl) (**Figure 26**). When AA, UA, DA and NaCl were added to this non-enzyme C_MCNF based sensor, it was confirmed that there was almost no electrical change. However, the change of the peak of about 3 times or more was confirmed, when the addition of glucose.

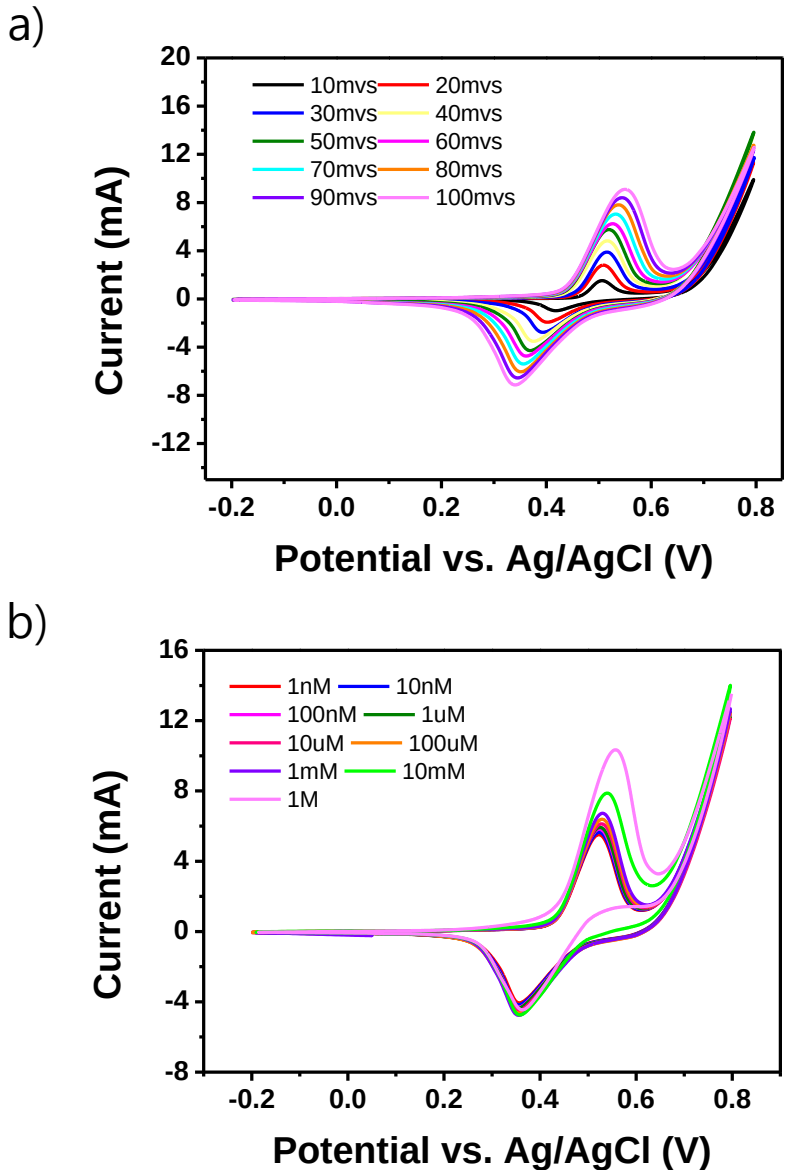

Figure 24. Detection of glucose in 0.1 M NaOH solution by using the C0.05_MCNF. a) CV curves measured at diffent scan rates b) CV curves in the presence of various concentrations of glucose

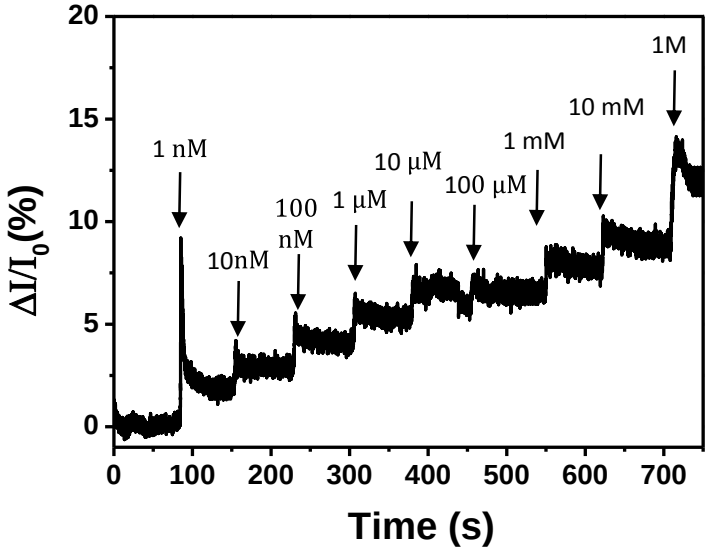

Figure 25. Amperometric response of the C0.05_MCNF electrode (at 0.58 V) upon addition of glucose with increasing concentrations

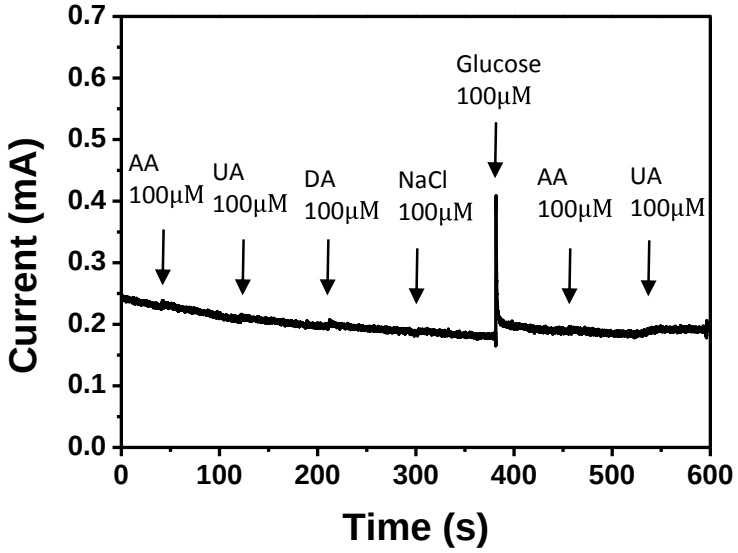

Figure 26. Amperometric response of the C0.05_MCNF with the addition of diffent analytes

3.2 Fabrication of a One-dimensional Tube-in-tube Polypyrrole/Tin oxide Structure for Highly Sensitive DMMP Sensor Applications

3.2.1 Fabrication of the One-dimensional Tube-in-tube Polypyrrole/Tin oxide Structure

Figure 27 illustrates the overall procedure for the fabrication of the PPy@SnO_2 tube-in-tube structure. Single- nozzle electrospinning was conducted using a polymer solution composed of two solvents, i.e., N,N-dimethylformamide (DMF) and ethanol.[26, 109, 110] First, poly(vinylpyrrolidone) (PVP) was dissolved in the mixed solvent with tin(II) chloride dihydrate as the metal oxide precursor. To fabricate the complex 1D SnO_2 tube-in-tube structure, the electrospun nanofiber was calcined at 600 ℃ for 1 h while controlling the heating rate at 5 ℃ min^{-1}. An outer shell of rigid metal oxide formed as the ethanol evaporated. In the subsequent calcination, shrinkage continued as the viscoelastic gel core contracted. The core transformed into an inner hollow tube structure as the DMF solvent evaporated. A 1D SnO_2 tube-in-tube structure formed during the calcination step due to the difference in boiling points of the two solvents.[111-113] Control

experiments were carried out to modify the shape of the 1D SnO_2 structure by adjusting the heating rate (**Figure 28**). To fabricate the organic/inorganic composite, the SnO_2 tube-in-tube structure was dipped into an aqueous $FeCl_3$ solution with vigorous stirring at 60 ℃ for 3 h. The ferric cations (Fe^{3+}) were an initiator for VDP and interacted with the partial negative charge of oxygen on the SnO_2 surface. The $FeCl_3$-soaked tube-in-tube material was then placed in the VDP vacuum chamber and exposed to pyrrole monomer at 120 ℃ for 30 min. The thickness of the conducting polymer layer could be adjusted by conducting the VDP step at different temperatures in **Figure 29** (60 ℃, 100 ℃). The uniform dispersion of Fe^{3+} as an oxidant ensured that polymerization of the pyrrole monomer occurred via chemical oxidation polymerization on the surface of the tube-in-tube SnO_2. Consequently, an aggregate-free 10-nm-thick-PPy layer formed on the surface of the tube-in-tube SnO_2 to form the PPy@SnO_2. When the VDP was conducted in ambient state, an uneven PPy layer was observed (**Figure 30**).

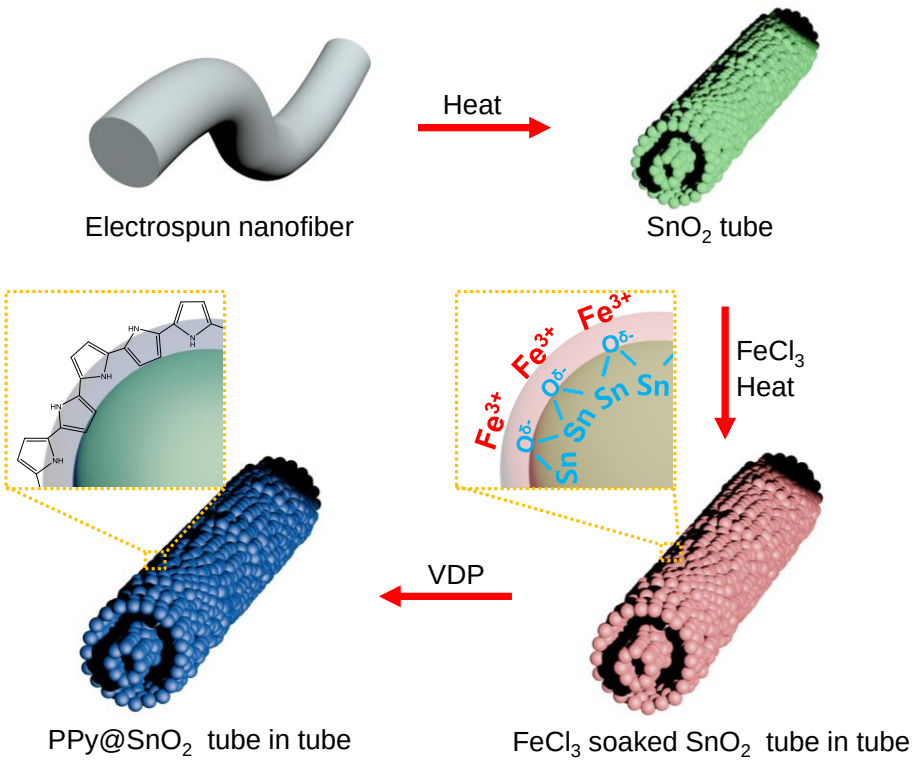

Figure 27. Schematic diagram of the sequential fabrication of the PPy@SnO_2 tube-in-tube structure

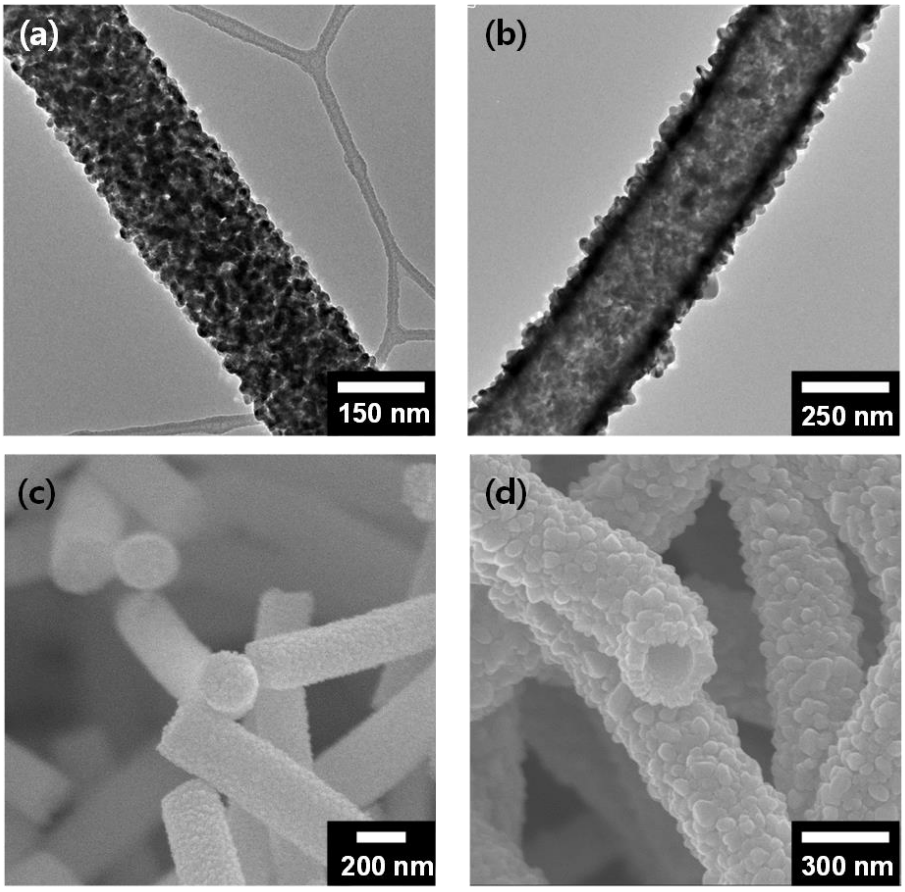

Figure 28. (a, c) Transmission electron microscopy (TEM) and scanning electron microscopy (SEM) images of the SnO_2 fibers. (b, d) TEM and SEM images of the SnO_2 tubes

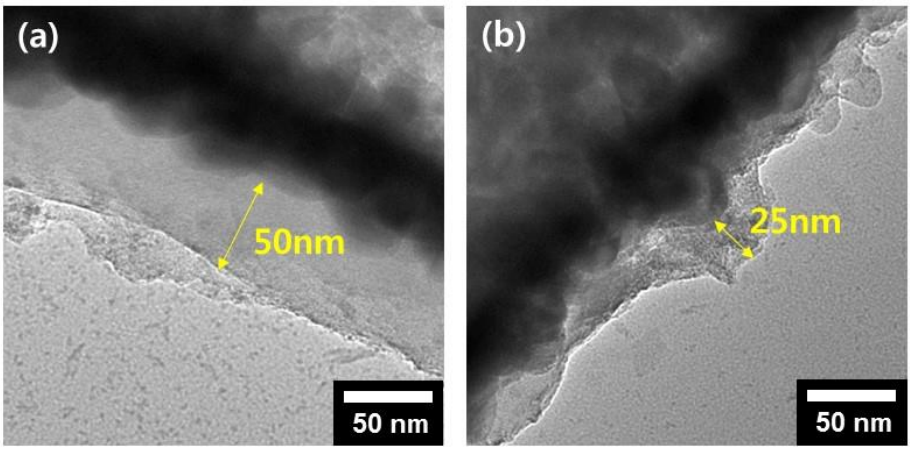

Figure 29. Transmission electron microscopy (TEM) images of the PPy@SnO_2 tube in tube by conducting the VDP step at different temperature (a)60 ℃ and (b)100 ℃

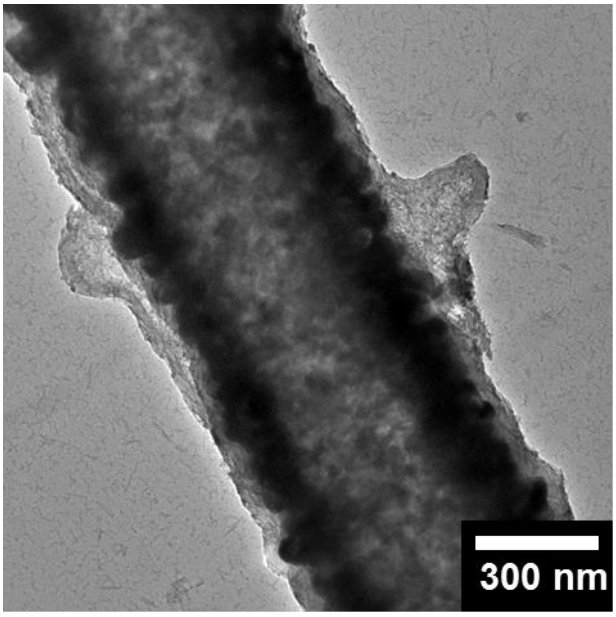

Figure 30. TEM image of the morphology of the PPy coated SnO_2 tube structure after VDP method in ambient state

3.2.2 Characterizations

Figure 31a shows a field-emission scanning electron microscopy (FE-SEM) image of the electrospun nanofiber (diameter: 500 nm), revealing a smooth surface and continuous features. Calcinied at 600 ℃ for 1 h transformed the smooth electrospun nanofiber into the 1D metal oxide tube-in-tube structure that was composed of a large number of nanograins (**Figure 31b** and **31c**). The diameter of this unique 1D nanostructure was smaller at 350 nm, which resulted from PVP decomposition during the calcination step. Also, SEM observation confirmed that it has a high aspect ratio (**Figure 32**).Transmission electron microscopy (TEM) was used for further morphological analysis of the SnO_2 tube-in-tube structure (**Figure 31d**), which revealed a unique hollow tubular structure having inner tube and outer shell diameters of ca. 100 and 350 nm, respectively.

Figure 31e displays a high-resolution TEM (HR-TEM) image of the SnO_2 surface, revealing an interplanar spacing of 0.34 nm for the (110) plane of the rutile lattice originated from highly crystalline SnO_2. The selected area electron diffraction (SAED) pattern revealed the polycrystalline nature of the SnO_2 tube-in-tube structure with (110), (101), (200) and (211) planes, respectively (**Figure 31f**).[114]

The tube-in-tube SnO_2 was coated with PPy using vapor-phase pyrrole monomer to ensure sensor operation at room temperature. **Figure 31g** and **31h** show that the PPy was successfully coated on the surface without any structural deformation. Additionally, polymerization of the vaporized pyrrole monomer in the presence of Fe cations provided a uniform, aggregate-free, ca. 10-nm-thick PPy layer (**Figure 31i**).

The crystallinity of the PPy@SnO_2 tube-in-tube structure was further characterized by X-ray diffraction (XRD) (**Figure 33a**). All of the diffraction peaks could be assigned to the tetragonal cassiterite crystalline phase of tin oxide (JCPDS card No. 77–0452), primarily in the (110), (101), and (200) orientations. No peaks corresponding to impurities were evident, indicating the high purity of the SnO_2 tube-in-tube material.[115, 116] The PPy-coated SnO_2 tube-in-tube material had a similar XRD pattern because the 10-nm-thick PPy layer did not deform the underlying structure. These XRD results indicate that our PPy@SnO_2 tube-in-tube structure was successfully coated with a thin conducting polymer layer. Fourier transform-infrared (FT-IR) spectroscopy was also used to characterize the PPy layer on the SnO_2 tube-in-tube structure (**Figure 33b**). The peaks at 1554 and 1473 cm^{-1}

correspond to C–C and C–N stretching vibrations in the pyrrole ring, respectively, while peaks at 1294 and 1195 cm^{-1} are associated with =C–H in-plane vibrations. These spectral features indicated that a PPy layer was present.[31]

X-ray photoelectron spectroscopy (XPS) was used to characterize the chemical bonding in the PPy@SnO_2 tube-in-tube structure. **Figure 33c** shows the high-resolution N1s peak of the PPy@SnO_2 tube-in-tube material. The strong N 1s peak corresponds to nitrogen atoms in the pyrrole ring of PPy. The deconvoluted peaks at 399.6 and 401 eV are related to the pyridinic and pyrrolic nitrogen atoms, respectively. As expected, the SnO_2 tube-in-tube structure lacking the PPy layer did not display any N 1s peaks. The Sn 3d spectra shows two symmetrical peaks at 489 and 497.5 eV corresponding to Sn d5/2 and Sn d3/2, respectively, with an energy separation of 8.5 eV (**Figure 33d**).[31] **Figure 34** shows the overall XPS spectroscopy of the PPy@SnO_2 tube in tube over the range of 0-1200eV; carbon, nitrogen, oxygen, tin, and iron atoms were present. Based on the XPS peak, it is considered that the small quantities of iron atom originated from $FeCl_3$ solution is still exist.

To further characterize the PPy@SnO2 tube-in-tube, the EDS mapping and EDX spectra analysis were carried out (**Figure 35 and 36**).

The surface morphology of the 1D PPy@SnO_2 tube-in-tube was investigated by nitrogen adsorption-desorption isotherm curves (**Figure 37**). Because of the structural effect, the nitrogen adsorption-desorption isotherm curve of the 1D PPy@SnO_2 tube-in-tube structure shows the higher relative pressure (P/P_0) compared with the 1D PPy@SnO_2 fiber and tube. Moreover, Brunauer-Emmett-Teller (BET) surface area of the PPy@SnO_2 tube-in-tube (38.4 m^2/g) was higher than that of the fiber (12.5 m^2/g) and tube (24.3 m^2/g).

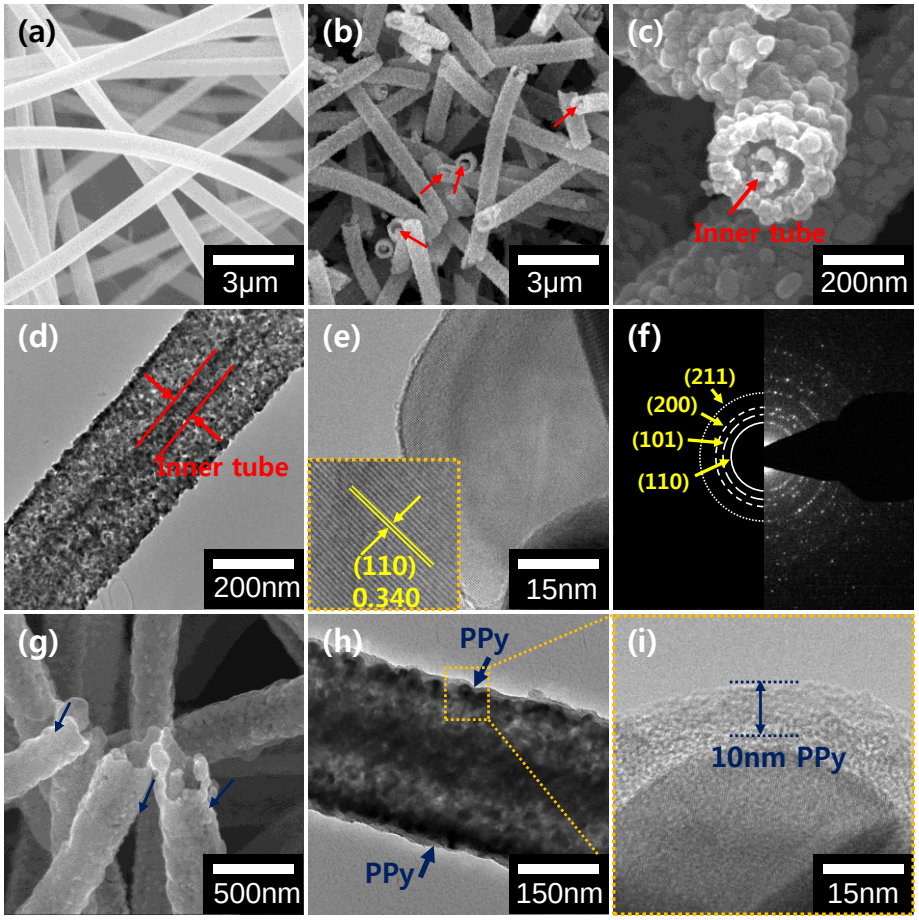

Figure 31. (a) Field-emission scanning electron microscopy (FE-SEM) image of the electrospun nanofiber. (b) Low-and (c) high-resolution FE-SEM images of the tube-in-tube SnO_2. (d) Low-and (e) high-resolution transmission electron microscopy (TEM) image of the tube-in-tube SnO_2. (f) Selected area electron diffraction (SAED) pattern of the tube-in-tubeSnO_2. (g) FE-SEM and (h) TEM images of the tube-in-tube polypyrrole (PPy)/SnO_2. (i) High-resolution TEM image of the tube-in-tube PPy/SnO_2

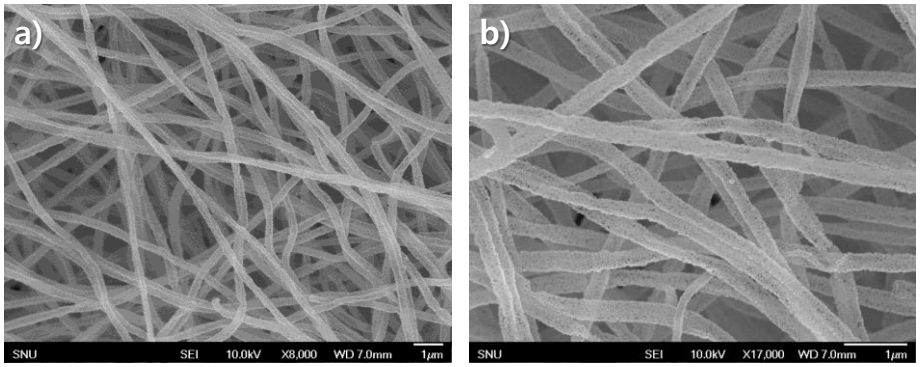

Figure 32. (a) Low-and (c) high-resolution FE-SEM images of the tube-in-tube SnO_2

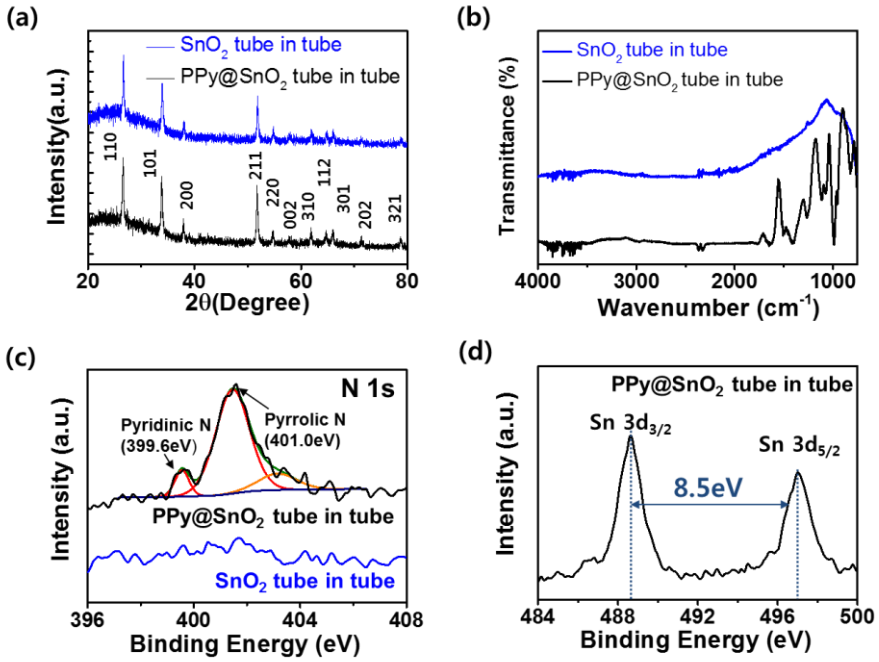

Figure 33. (a) X-ray diffraction (XRD) pattern for the tube-in-tube SnO_2 (blue) and tube-in-tube PPy@SnO_2 (black) structures. (b) Fourier transform-infrared (FT-IR) spectra of the tube-in-tube SnO_2 (blue) and tube-in-tube PPy@SnO_2 (black) structures. (c) High-resolution N 1s X-ray photoelectron (XPS) spectra of the tube-in-tube SnO_2 (blue) and tube-in-tube PPy@SnO_2 (black) structures. (d) High-resolution Sn 3d pattern of the tube-in-tube PPy@SnO_2

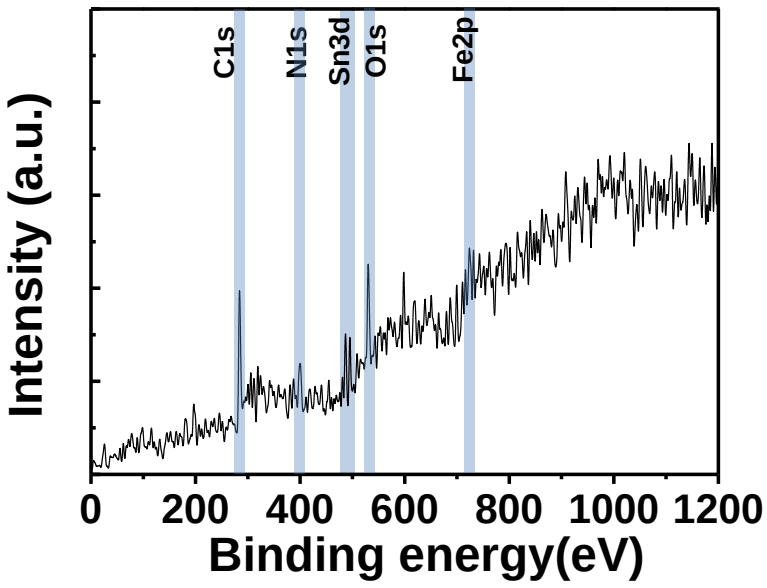

Figure 34. X-ray photoelectron spectroscopy (XPS) analysis of a fully scanned spectra (0–1200 eV)

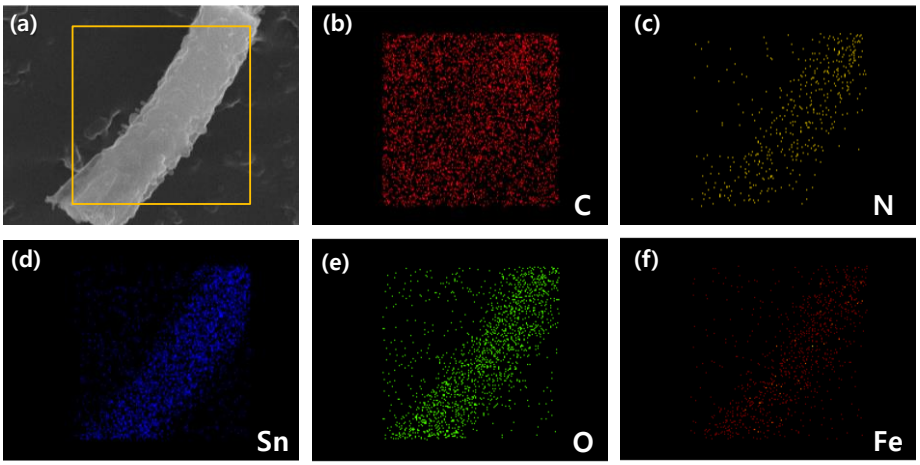

Figure 35. EDS dot mapping of PPy@SnO_2 tube in tube surface components indicating (a)overall SEM image, (b)carbon, (c)nitrogen, (d)tin, (e)oxygen and (f)iron

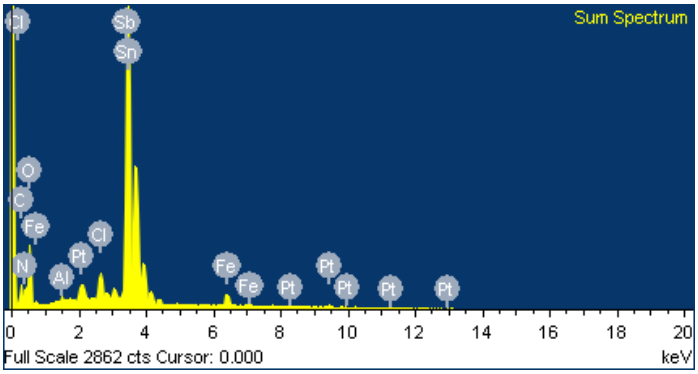

Figure 36. EDX spectrum of the PPy@SnO_2 tube in tube surface

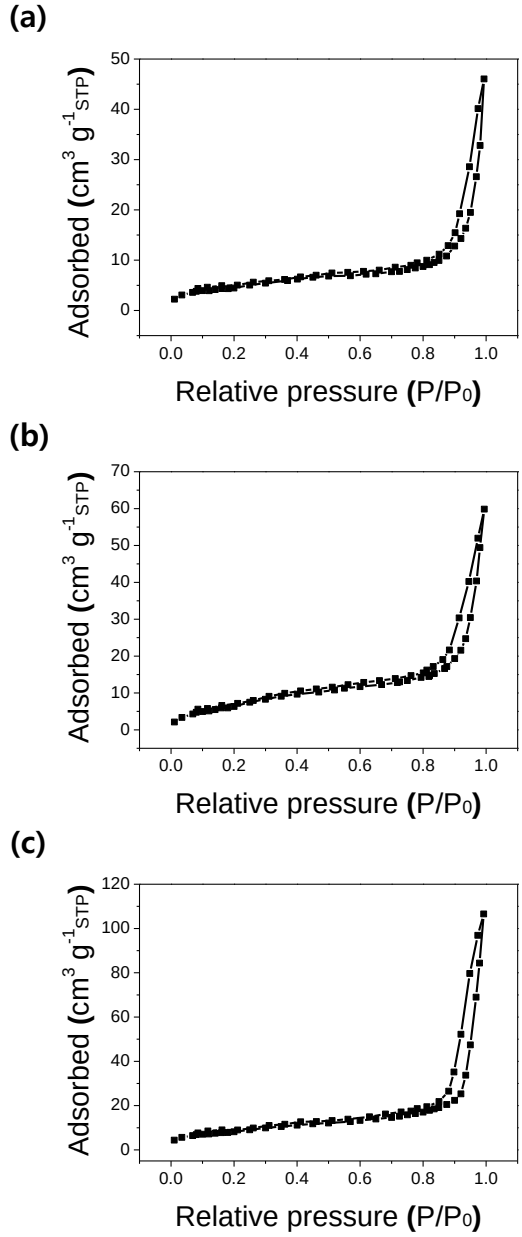

Figure 37. Nitrogen adsorption–desorption isotherm curves of (a) Fiber, (b) Tube, and (c) Tube-in-tube

3.2.3 **Electrical performance measurements**

The sensing performance of the tube-in-tube PPy@SnO_2 as a transducer was assessed by depositing it using drop-casting and spin-coating on a 2-μm-finger IDA substrate (**Figure 38**).[109, 117] The current–voltage curves displayed linear modulations because the tube-in-tube PPy@SnO_2 had ohmic contact with the sensor electrode (**Figure 39**). The real-time monitoring of the sensor was measured for various DMMP gas concentrations at room temperature. Upon exposure of the sensor electrode to DMMP, the pyrrole ring on the surface of the tube-in-tube PPy@SnO_2 interacted with DMMP molecules (**Figure 40**). Because DMMP is a powerful electron donor, the charge-carrier (electron–hole) concentration of the PPy backbone decreased. This phenomenon enhanced the resistance of the transducer. The electrical response was calculated using the following equation:

$$\Delta R / R_0 (\%) = (R - R_0) / R_0 \text{ X } 100 \%$$

Figure 41a displays the response upon sequential exposure to DMMP as a function of analyte concentration (0.05, 0.1, 1, 10, 100, 1000 ppb). The high sensitivity and rapid response/recovery times at room temperature of our tube-in-tube PPy@SnO_2-based sensor was attributed to the complex tubular structure and the p-n junction

between PPy and SnO_2.

When the SnO_2 surface is coated by PPy layer, depletion region will form between the interfaces. Then, electrons within SnO_2 will diffuse into the PPy layer and neutralize the holes. Therefore, partially shallow positive charge region will be formed on the SnO_2 layer based on the interfaces. Likewise, shallow negative charge region will be formed on the PPy layer. In the equilibrium, these regions retain their portion as shown in **Figure 42a**. When the sample were exposed to the target gas, the holes within PPy layer will react with target gas. The resistance of the PPy layer will be increased due to the reduction of hole concentrations within PPy layer. In conclusion, the depletion region on the PPy layer will be expanded, resulting in increase of the resistance change (**Figure 42b**).[44, 118] This synergetic effect is believed to increase the sensitivity of this sensor. The minimum detection level (MDL) of the sensor for DMMP was 0.05 ppb. This performance is very high compared to the previously reported results at room temperature (**Table 1**). To confirm the structural effect, control experiments were carried out using polymer-coated 1D SnO_2 fibers, tubes and nanoparticles (**Figure 43**) as the sensor transducer (**Figure 44** and **45**). The calibration curves calculated from real-time

sensing data are plotted in **Figure 46** for the different 1D structures. **Figure 41b** shows the electrical response of the tube-in-tube PPy@SnO_2-based sensor during periodic exposure to 0.05 ppb of DMMP at room temperature. Similar responses for DMMP were measured after cyclic testing. Moreover, the stability test indicated that our tube-in-tube PPy@SnO_2-based sensor retained 70.1% of its initial sensitivity during the monitoring period (**Figure 41c**). Average performance was confirmed for 10 devices at 1ppm (**Figure 47**).

Selectivity is one of the most important metrics used to evaluate sensor performance. **Figure 41d** shows the results of selectivity testing of the tube-in-tube PPy@SnO_2-based sensor toward various volatile organic compounds (VOCs) at room temperature. These VOCs were selected because they had similar functional groups that would interact via hydrogen bonding with the PPy@SnO_2 tube-in-tube surface. The vapors were introduced to the tube-in-tube PPy@SnO_2-based sensor in the same way as with DMMP. The change of the signal for DMMP vapor was at least double that for other vapors due to its intermolecular forces and dipole moment. The DMMP molecule contains an acceptor group (-OCH_3) that can generate strong hydrogen bonds and has high polarity (3.62 D).[62] These results demonstrated

that the PPy@SnO_2 tube-in-tube-based sensor had excellent selectivity and performed as a high-performance DMMP sensor.

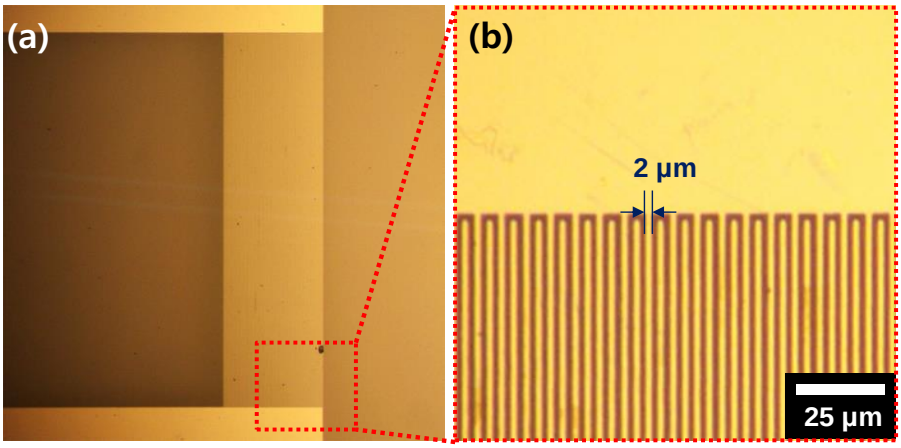

Figure 38. (a) Low- and (b) high-resolution optical microscopy images of the interdigitated array (IDA) electrode

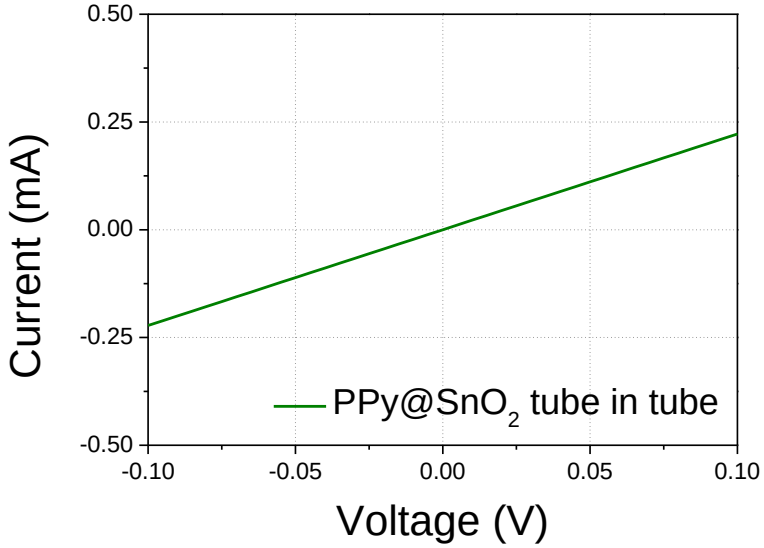

Figure 39. Current–voltage (I–V) curve of the tube-in-tube PPy@SnO_2 sensor electrode

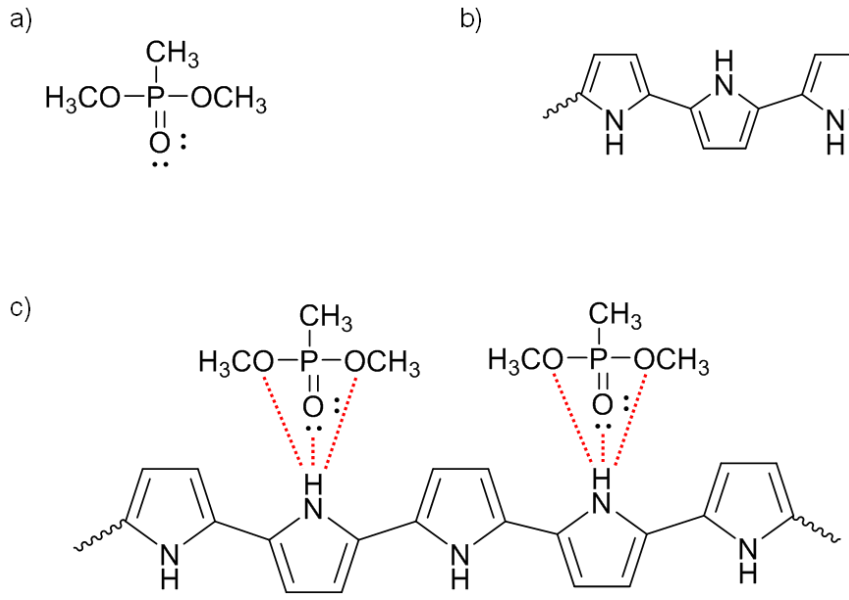

Figure 40. Molecular structures of (a) dimethyl methylphosphonate (DMMP) and (b) polypyrrole (PPy). (c) Schematic diagram describing the effect of hydrogen bonding on PPy

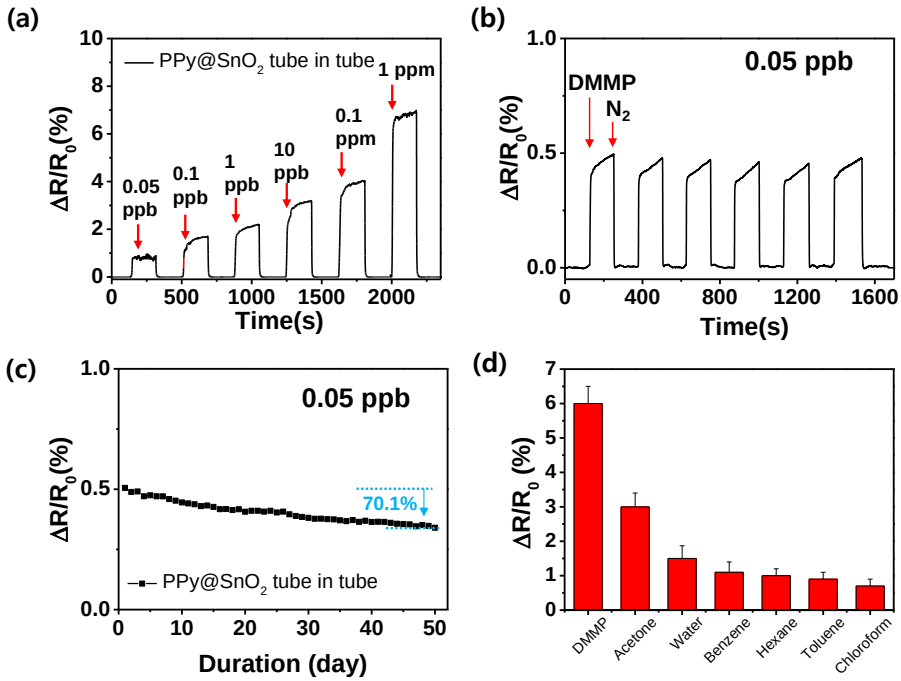

Figure 41. (a, b) Real-time responses of the tube-in-tube PPy@SnO_2 structure upon periodic exposure to dimethyl methylphosphonate (DMMP); (a) 0.05 ppb to 0.1 ppm and (b) 0.05 ppb. (c) Long-term stability of the tube-in-tube PPy@SnO_2 structure. (d) Selective DMMP-sensing characteristics of the tube-in-tube PPy@SnO_2 structure with respect to interfering analytes; each analyte concentration was fixed at 1 ppm. (acetone, water, benzene, hexane, toluene and chloroform)

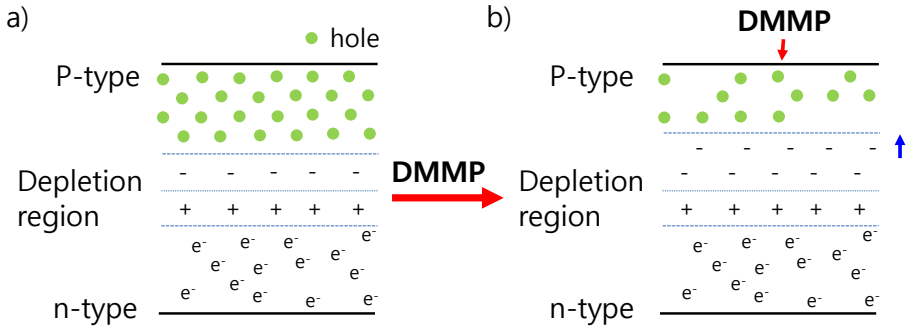

Figure 42. Schematic diagram of the formation of a p-n junction

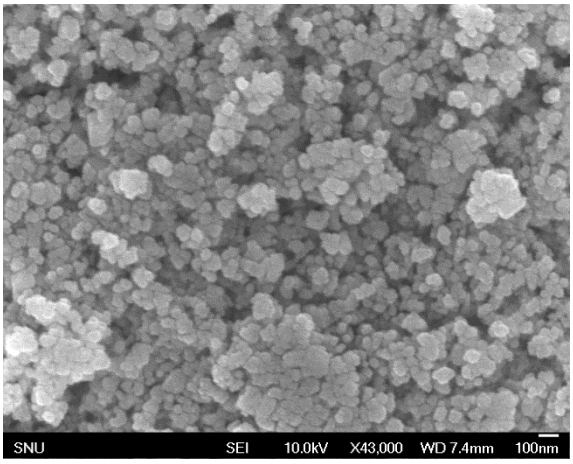

Figure 43. SEM image of the PPy@SnO_2 nanoparticles

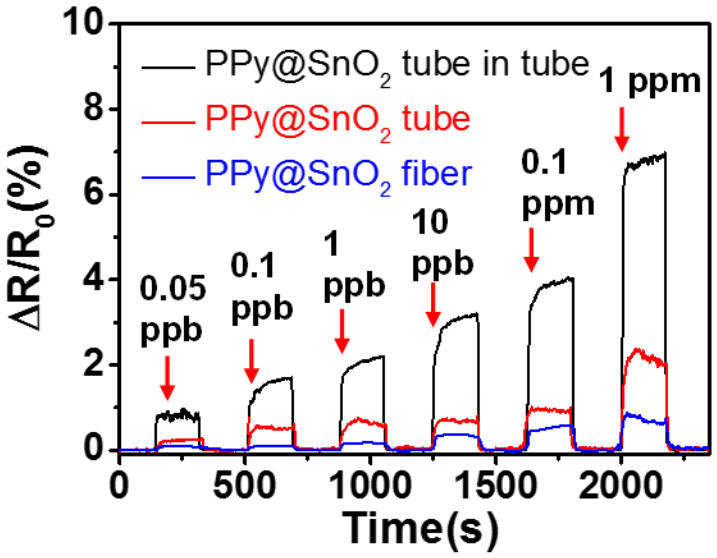

Figure 44. Real-time monitoring of PPy@SnO_2 having different one-dimensional (1D) structures after sequential exposure to DMMP

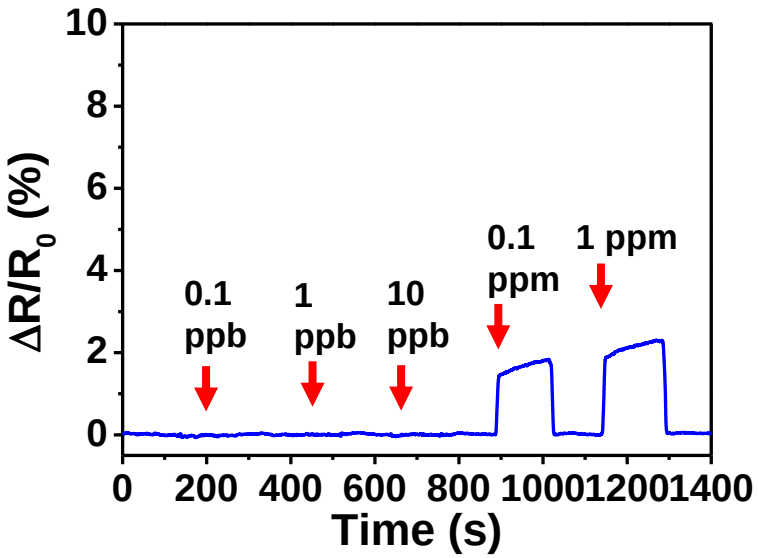

Figure 45. Real-time responses of the PPy@SnO_2 nanoparticles upon periodic exposure to dimethyl methylphosphonate(DMMP); 0.1 ppb to 1 ppm

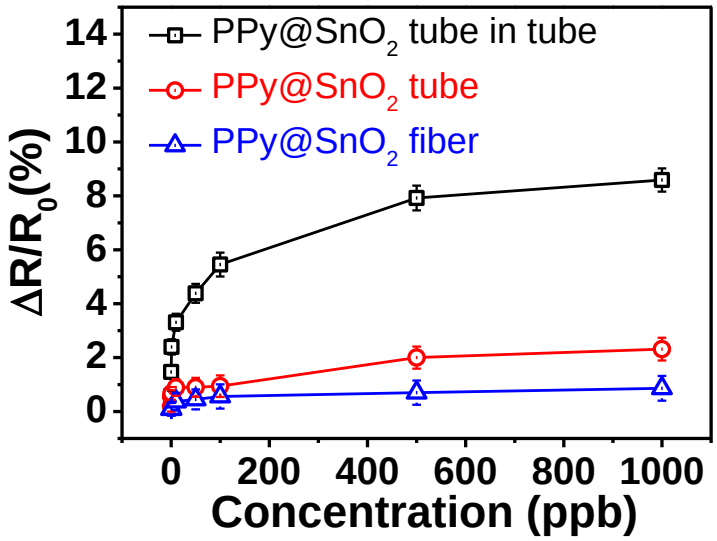

Figure 46. Changes in sensitivity as a function of DMMP concentration calculated from the real-time responses

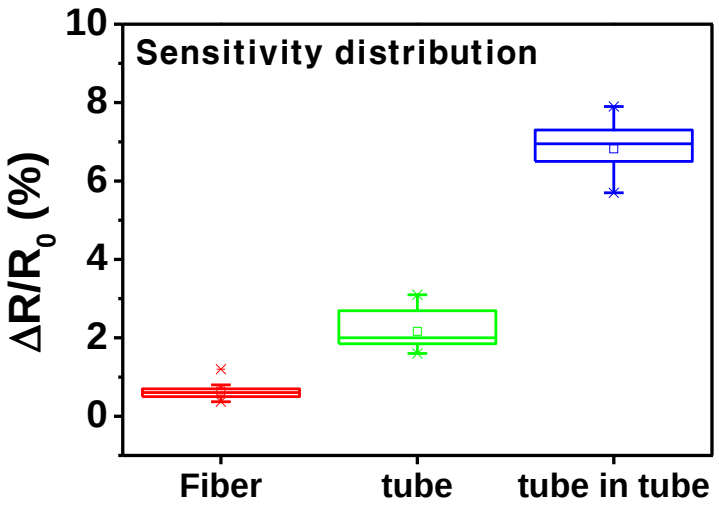

Figure 47. Variation and comparison of the sensitivity parameter. These parameters were evaluated from 10 devices fabricated at 1 ppm

Table 1. Room-temperature sensing properties of the tube in tube PPy@SnO_2-based sensor toward DMMP in comparison with other nanomaterial reported in the literature

Material[a)]	Morphology	MDL[b)]	Response time	Recovery time	Temperature(°C)[C)]	Ref.
Pani	fiber	5ppb	1s	40s	RT	
C-PPy	tube	0.5ppb	-	-	RT	
PPy/graphene	thin films	5ppm	1s	400s	RT	
CNF/SnO_2/ZnO 2	fiber	0.1ppb	<1s	30s	RT	
PPy/SnO_2	tube in tube	0.05ppb	1s	30s	RT	this work

[a)]CNF: carbon nanofiber, C-PPy: carboxylic acid functionalized polypyrrole, Pani: polyaniline [b)]MDL: minimum detectable level [c)]RT: room temperature

3.3 Fabrication of One-dimensional nano-nodule decorated Carbon Nanofiber for a Highly Sensitive and Selective Platelet-Derived Growth Factor Biosensor

3.3.1 Fabrication of CPZCNFs

Figure 48 illustrates the overall procedure for the fabrication of carboxylated polypyrrole-coated, zinc oxide-decorated ultrafine carbon nanofibers (CPZCNFs) via single-nozzle co-electrospinning and vapor deposition polymerization (VDP) methods. First, PVP solution containing the ZnO precursor ($ZnAc_2$) was mixed with PAN solution to make phase-separated polymers in the mixture solution. The mixed polymer solutions were then co-electrospun through a single nozzle. The result was that the phase-separated polymers in the mixed solutions formed core (PAN)/shell (PVP) nanofibers (NFs).[109] The electrospun core/shell NFs were subsequently calcined and carbonized to fabricate ZnO nanonodule-decorated hybrid CNFs (ZCNFs). These as-prepared MCNFs were *ca.* 40 nm in diameter with ZnO nanonodules (*ca*. 10 nm) on the surface and were aggregate free (**Figure 49**). The MCNFs were then dipped into ethanolic solution containing $FeCl_3$ as an initiator for the VDP step. In the dipping process, ferric cations (Fe^{3+}) were

adsorbed on the ZnO nanonodules because of a charge–charge interaction between Fe^{3+} ions and the partial negative charge of oxygen in the ZnO structure (red inset of **Figure 48**).[119, 120] The Fe^{3+}-adsorbed ZCNFs were exposed to 3-carboxylated pyrrole (CPy) monomer vapor in a 60 °C vacuum oven for 10 min. Polymerization of CPy monomers occurred via a chemical oxidation polymerization with the Fe^{3+} ions as oxidants on the ZnO surface.[119] As a result, the 3-carboxylated polypyrrole-coated ZCNFs (CPZCNFs) formed a 3-nm-thick coating layer on the surface (**Figure 50**). Additionally, there was no aggregation of the CPZCNFs despite the VDP steps, indicating that the Fe cations were uniformly dispersed on the ZCNF surfaces. To confirm the 3-carboxylated polypyrrole (CPPy) layer on the ZCNFs, Fourier-transform infrared (FT-IR) spectroscopy was carried out for each CNF, as shown in **Figure 51** The spectra of the ZCNFs exhibited the C–C–C symmetric stretching peak at around 850 cm^{-1}.[121] Due to the absence of the CPPy layer, the FT-IR spectrum of ZCNFs did not show peaks of functional groups, such as carbonyl and hydroxyl groups. However, the spectra of the CPZCNFs did show peaks at 1554 and 1473 cm^{-1}, corresponding to the C–C and C–N stretching vibrations in the pyrrole ring. Additionally, the peaks at 1294 and 1195 cm^{-1} were

attributed to =C–H in-plane vibrations. Furthermore, a peak at 1715 cm^{-1} was observed due to the stretching vibration of C=O and in the carboxylic acid functional group.[121-123] These spectral modulations indicate that the CPPy was coated successfully on the ZCNFs through the VDP step.

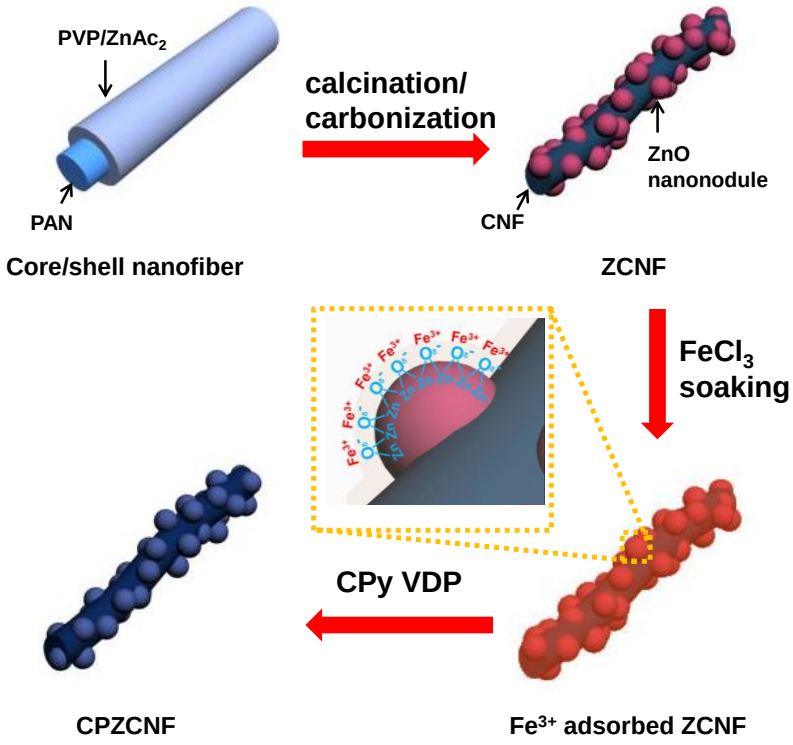

Figure 48. Illustrative diagram of the sequential fabrication steps for 3-carboxylated PPy coated hybrid carbon nanofibers (CPMCNFs)

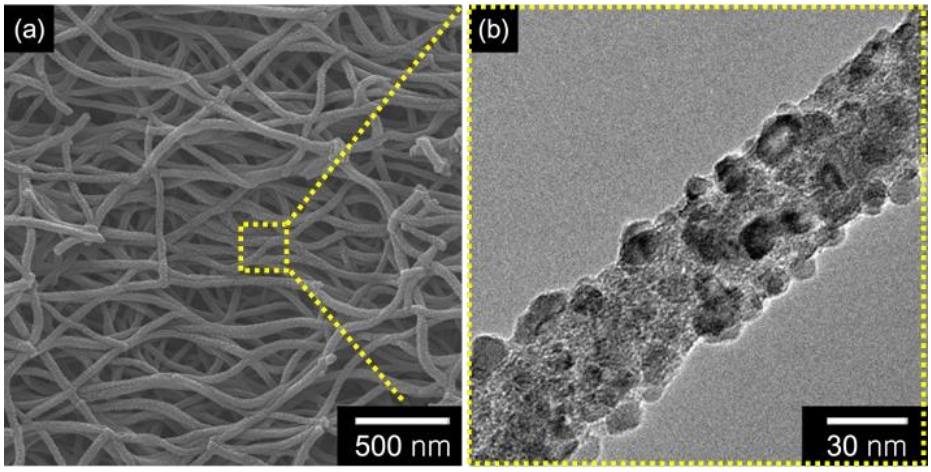

Figure 49. (a) SEM and (b) TEM image of ZnO nanonodule decorated on the surface CNFs with 40 nm-diameters

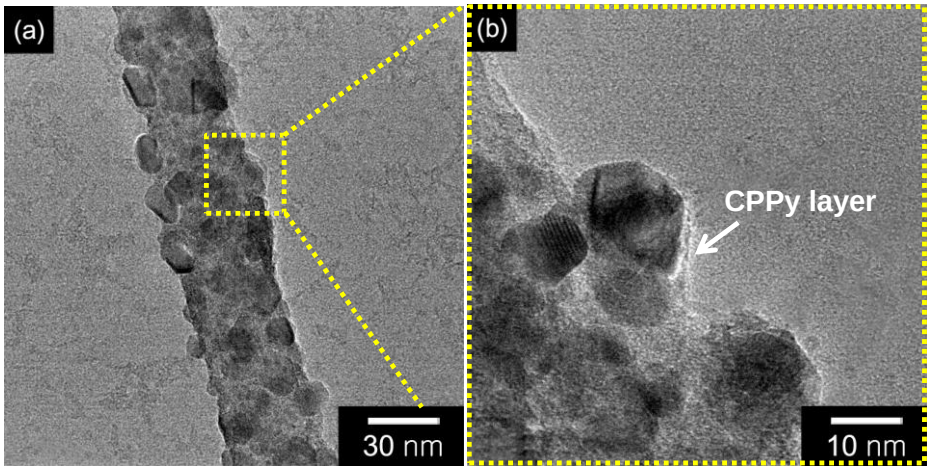

Figure 50. (a) TEM and (b) HR-TEM image of 3-carboxylated PPy coated hybrid CNFs with 3 nm-thickness coated layer on the surface

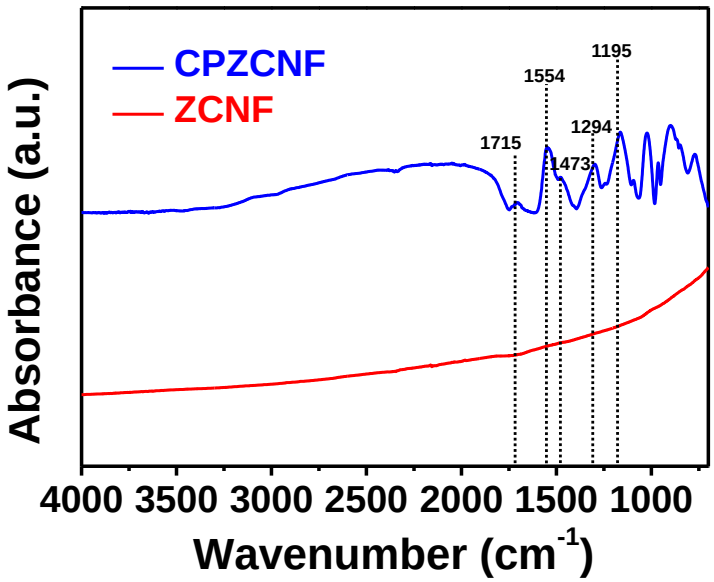

Figure 51. FT-IR spectra of MCNFs (red) and CPZCNFs (blue)

3.3.2. Fabrication of the CPB-Apt FET sensor

Figure 52 indicates the procedures for fabricating CPZCNF conjugated with the PDGF-B binding aptamer (CPB-Apt) FET sensor electrode using a condensation reaction of carboxyl and amino groups on the sensor electrode surface. First, CPMCNFs were attached by a chemical reaction, such as a condensation reaction through the carboxyl group (-COOH) of CPPy and the amino group ($-NH_2$) of the (3-aminopropyl)trimethoxysilane (APS)-treated interdigitated array (IDA) sensor electrode. The condensation reaction of CPPy and the APS-treated electrode formed amide bonding (-CONH-) using condensing agent (4-(4,6-dimethoxy-1,3,5-triazin-2-yl)-4-methyl-morpholinium (DMT-MM)).[124-126] Thus, the CPZCNFs covalently anchored on the IDA electrode were fabricated through simple condensation reactions. Then, the amine ($-NH_2$)-modified PDGF-B binding aptamer was immobilized on the CPZCNFs surface through a chemical condensation reaction between the carboxyl group (-COOH) of CPPy and the amino group ($-NH_2$) of the PDGF-B binding aptamer using a condensing agent (DMT-MM). As a result, CPB-Apt IDA sensor electrode was fabricated for applying electrolyte-based FET biosensor. The covalent bonding is strong because of the direct chemical bonding.

Indeed, this covalent attachment provides some advantages, such as better stability for analyte sensing in the liquid phase and the possibility of control of the functionality of the CPZCNFs, in contrast to a non-covalent approach. To evaluate the electrical contact of CPB-Apt on the IDA substrate, current–voltage (*I*-*V*) characteristics were investigated, as shown in **Figure 53a**. When the electrical contact is poor, the *I*-*V* modulation is nonlinear because of the formation of Schottky barriers at the electrode contact. However, the characteristics of the *I*-*V* curve for each CPZCNFs revealed linearity, *i.e.*, ohmic contact, indicating that the CPZCNFs bonded covalently to the IDA surface, providing a good electrical contact. The d*I*/d*V* values decreased slightly with the introduction of the PDGF-B binding aptamer on the CPZCNFs surface. Also, increasing the concentration of the PDGF-B binding aptamer on the CPZCNFs decreased the d*I*/d*V* values. It can be considered that PDGF-B binding aptamers were nonconductive. Consequently, the difference of the *dI/dV* values is presumably due to the difference in the resistance. However, the linearity of *I*-*V* modulation means that ohmic contact was retained after introduction of the aptamer. Thus, the PDGF-B binding aptamer was effectively incorporated into CPZCNFs with no deterioration in electrical contact or conductivity.

Figure 53b shows a liquid-ion-gated FET-type sensor system based on CPB-Apts. The liquid-ion-gated FET geometry was constructed with the IDA substrate array using CPZCNFs as the conductive channel. The FET sensor platform was surrounded with phosphate-buffered saline (PBS, pH 7.4), which facilitated gate control. The two gold bands of the IDA electrode acted as the source and drain in this FET-type sensor system. Furthermore, the CPB-Apts were immobilized in the liquid electrolyte with no deterioration due to the covalent bonds to the IDA surface. **Figure 53c** shows the modulation of source-drain current (I_{sd}) and voltage (V_{sd}) under varying gate voltage (V_g) to investigate this FET-type CPB-Apt sensor device. The I_{sd} became more negative when the V_g increased in the negative direction. The subsequent graph indicated that the CPB-Apt FET sensor showed a p-type accumulation mode in the V_g range of 0 to -100 mV. Moreover, the I_{sd} that followed through the CNF network channel was modulated by varying V_g. Negative V_g can give rise to an increase in the oxidation level of the CPZCNF chain. These negative modulations indicate that CPZCNF is a p-type (hole-transporting) transducer in the doped state. These results indicate that the CPB-Apt FET sensor is suitable as an electrochemical biosensor for detecting charged bio-molecules in a

PBS buffer solution.

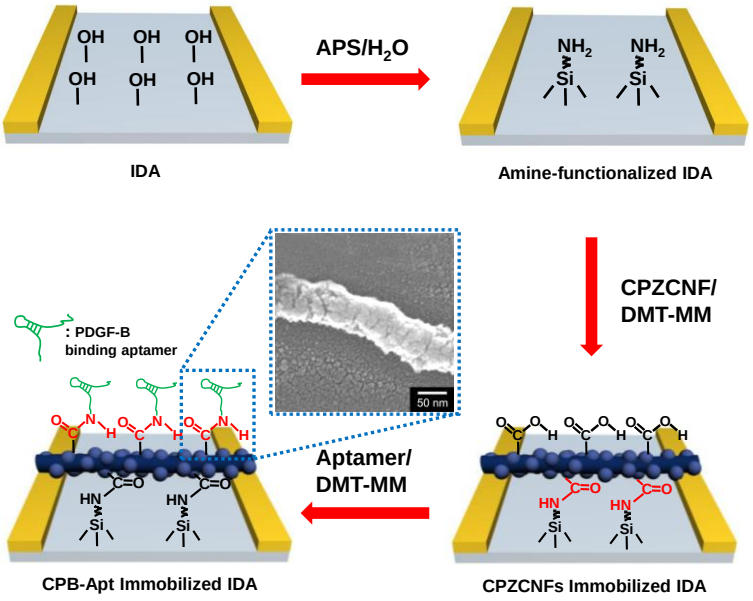

Figure 52. Synthetic protocol of immobilization of CPZCNF-aptamer tranducers on the inter-digitated array electrode substrate

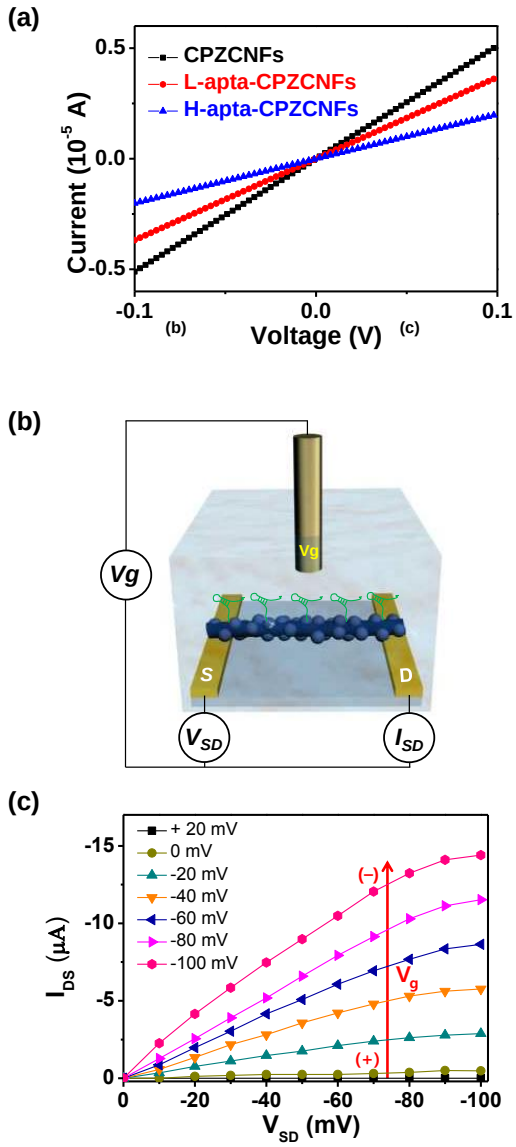

Figure 53. (a) Current-voltage (I-V) curves of aptamer-conjugated CPZCNF immobilized IDA electrode (black: without aptamer; red: low concentration of conjugated-aptamer; blue: high concentration of conjugated-aptamer). (b) Schematic diagram of a liquid-ion gated

3.3.3. Real-time responses of the CPB-Apt FET sensor

To investigate the performance of the CPB-Apt FET sensor, current changes were measured with various PDGF concentrations in real time at constant V_{sd} (50 mV) and V_g (50 mV). **Figure 54a** indicates the real-time responses of the CPB-Apt FET sensor to the three types of PDGF (PDGF-AA, PDGF-AB, and PDGF-BB). The CPB-Apt sensor showed a very fast real-time response (<1 s) when the sensor device was exposed to the diverse concentrations of the target PDGF (PDGF-AB and PDGF-BB) solution. Furthermore, the CPB-Apt sensor showed a concentration-dependent decrease in I_{sd} on exposure to PDGF-BB and PDGF-AB. The current decrease is caused by the negative charge of the PDGF-B binding aptamer. The binding aptamer can be screened by the PDGF-B of PDGF-AB/PDGF-BB when the target biomolecule-aptamer complex is formed. The specific binding caused a structural rearrangement of the aptamer, finally leading to a decrease in the negatively charged base state. The decreased negative charge density at the CPB-Apt sensor interface can reduce the hopping rate of charge carriers (holes) in the CPMCNFs, which is probably responsible for the decrease in current.[127] The negative charge of the CPB-Apt sensor reduced to limit of detect level that is generally considered a significant

signal when the signal-to-noise ratio is greater than or equal to 3.0 with decreasing concentration of target analyte.[125] The limit of detection of the CPB-Apt sensor was 5 fM (signal-to-noise ratio: 3.4) for PDGF-BB, lower than those of other aptamer-based PDGF sensor and carboxylated polypyrrole coated pristine CNF without metaloxide nanonodule (see **Figure 55**).[128, 129] Additionally, PDGF-AB detected as low as 500 fM and injection of PDGF-AA did not induce current changes because the PDGF-A chain had no affinity for the PDGF-B binding aptamer.

Figure 54b shows the calibration curve of the sensitivity of the CPB-Apt FET sensor. The sensitivity (S) was determined from the normalized current change ($(\triangle I/I_0)_{sp}$ x 100) saturation point, measured after a 10s of the analyte addition was inserted. The sensitivity was enhanced with increasing concentrations from 5×10^0 to 5×10^4 fM of the PDGF-BB and from 5×10^2 to 5×10^4 fM of PDGF-AB, respectively. Importantly, the sensitivity of CPB-Apt sensor to PDGF-BB was higher than that of PDGF-AB over a wide range of concentrations. Also, there was no current change with increasing injection amounts of PDGF-AA in the FET sensor device due to the absence of any affinity with the PDGF-B binding aptamer.

To test the selectivity of the CPB-Apt FET sensor for PDGF-B analysis, control experiments were conducted using other biological components. **Figure 57a** shows the selectivity of the CPB-Apt FET sensor toward the three variants of PDGF and other biomolecules, including bovine serum albumin (BSA), ATP, and calmodulin (Cal). During the real-time selectivity test, insignificant changes in I_{sd} were observed on the addition of non-target molecules such as BSA, ATP, Cal, and PDGF-AA. Furthermore, there was a difference in I_{sd} with the two types of PDGF (PDGF-AB, and PDGF-BB) because the PDGF-B binding aptamer had no affinity for the PDGF-A chain. In addition, CPB-Apt sensor displayed significant I_{sd} changes at 5 fM of PDGF-BB, however, did not show any significant signals of PDGF-AB (**Figure 57b**). Thus, the CPB-Apt FET sensor showed higher specificity for PDGF-BB, which is composed only of PDGF-B chains, than for PDGF-AB, which is composed of both A and B chains. These results demonstrated the high selectivity of the CPB-Apt FET sensor. **Figure 58** suggests the reusability of the CPB-Apt FET sensor system based on sensitivity changes to a constant concentration (50 pM) of the three variant PDGFs. To demonstrate the reusability of CPB-Apt sensor, a three-step process was conducted. First, the used CPB-Apt sensor was

washed with sodium chloride solution which causes disruption of the hydrogen bonding and electrostatic interactions responsible for most of the aptamer-target association. Second, it was rinsed with distilled water and air-dried for removing salt residue.[130, 131] Then, injections of target biomolecules were carried out several times at an injection interval of 3 days. The sensitivity of the CPB-Apt sensor system to the three variants of PDGF was generally consistent during the repeated tests, although the sensitivity decreased slightly due to aptamer degradation. The covalent anchoring of the electrode substrate/CPZCNFs and CPZCNF/binding aptamers provided stability for long-term reusability. Based on these data, this covalent anchoring aptamer sensor can be successfully reused in consecutive assays.

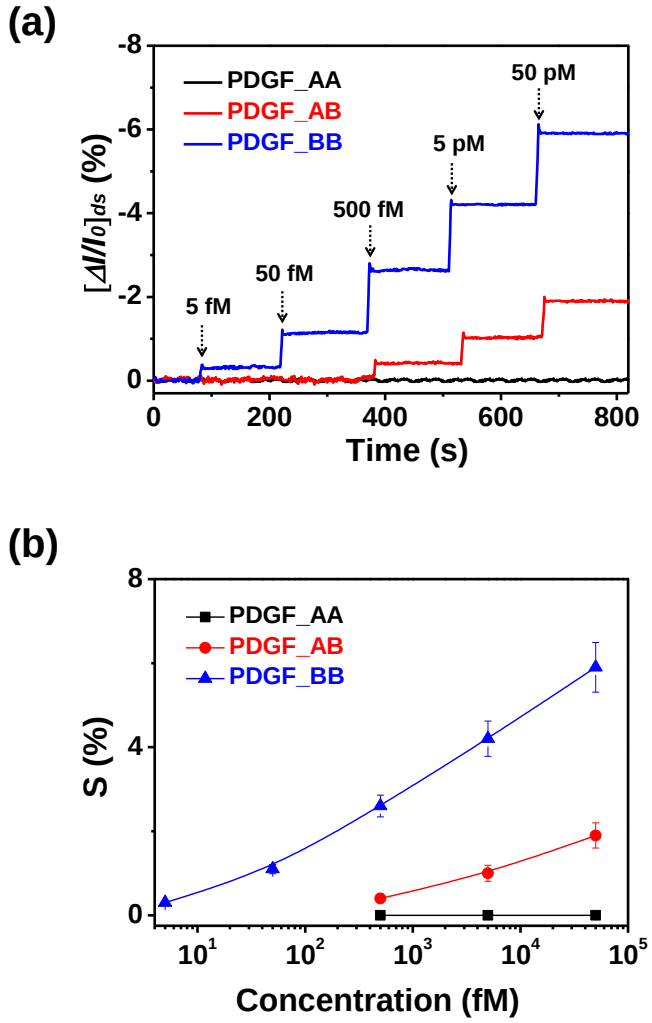

Figure 54. (a) Real-time responses with normalized current changes (Vg: 50 mV and Vsd: 50 mV) and (b) calibration curve of CPB-Apt FET sensor toward three variants of PDGF with different concentration (black: PDGF_AA; red: PDGF_AB; blue: PDGF_BB)

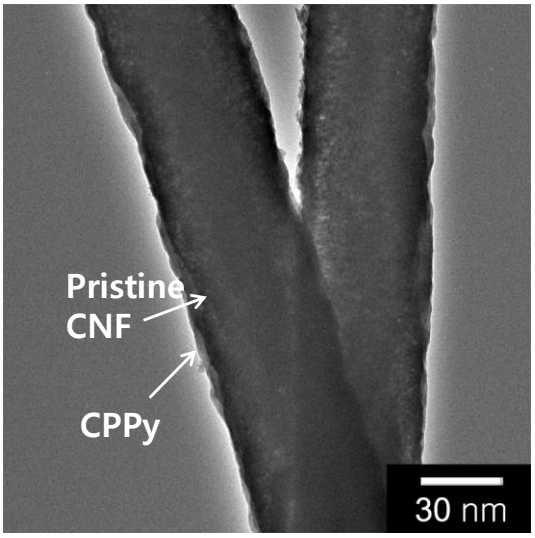

Figure 55. TEM image of Carboxylated polypyrrole(CPPy) coated pristine CNFs using vapor deposition polymerization (VDP). There was CPPy layer on the surface of CNFs

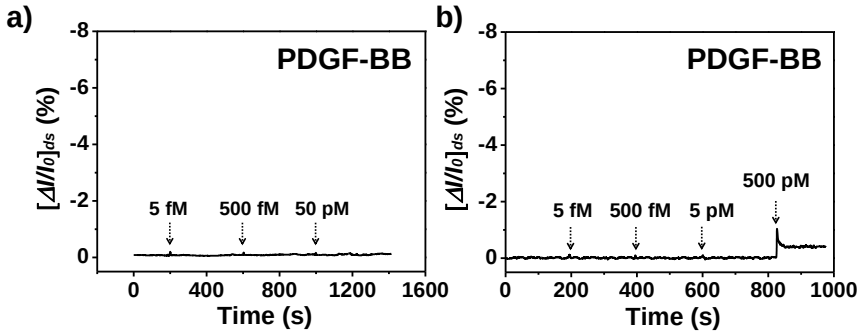

Figure 56. Control experiment using (a) CPPy coated MCNFs without PDGF-B binding aptamer and (b) CPPy coated pristine CNFs with aptamer

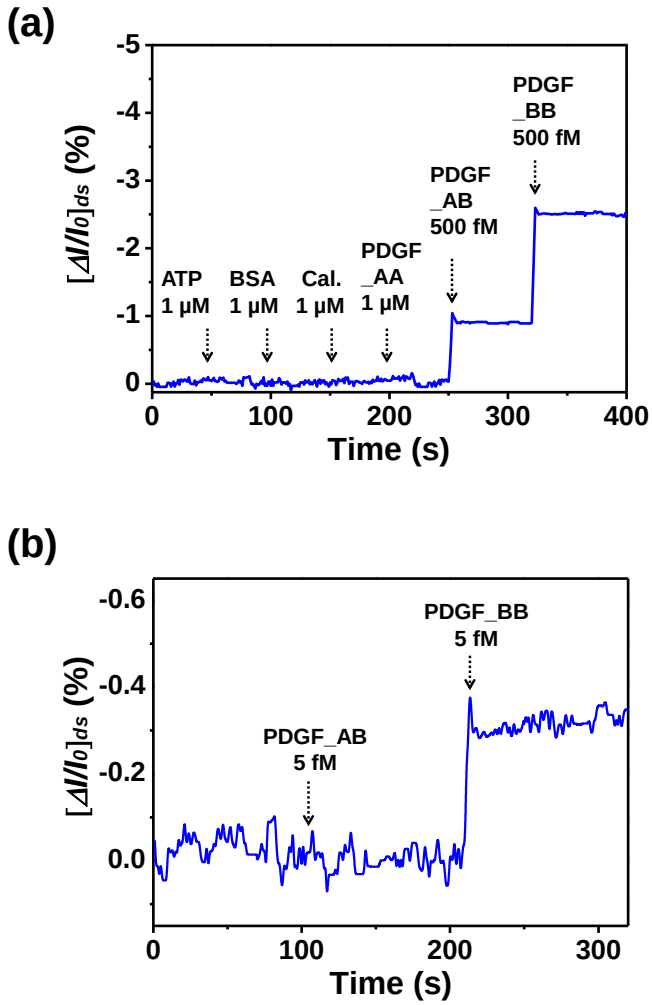

Figure 57. Real-time selective responses of CPB-Apt FET sensor toward (a) 1 μM of non-target molecules (ATP, BSA, Calmoduline (Cal), PDGF-AA) and 500 fM of target molecules (PDGF-BB and PDGF-AB) and (b) 5 fM of different target molecules (Vg: 50 mV; Vsd: 50 mV)

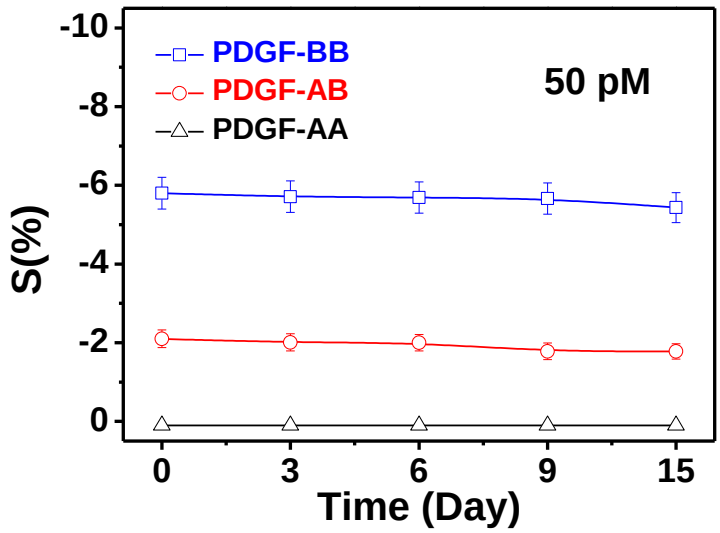

Figure 58. Re-usability test of the CPB-Apt FET sensor system toward three variants of PDGF at 50 pM concentration (black: PDGF-AA; red: PDGF-AB; blue: PDGF-BB)

4. Conclusion

The various types of one-dimensional nanostructure were fabricated by mixing the polymer, solvent and metal oxide precursor using electrospinning method. This fabricated 1-D nanosturucture were applied to gas sensor, and biosensor. In addition, this manufacturing method has possibilities in other application fields as well as sensors. The subtopic is concluded in the view point of each subtopic as follows:

1. We fabricated the mutlincahnnel carbon nanofibers (MCNFs) and cobalt oxide nanoparticles (NPs) embedded MCNFs using hybrid polymer solution and single nozzle electrospinning. During the electospinning, phase seperated nanofibers were formed because of the difference in surfacetension between PMMA and PAN. After heat treatment, carbon nanofibers with hollow inner channel were successfully fabricated. In addition, cobalt oxide NPs were dispersed uniformly inside the C_MCNFs without any aggregation. This C-MCNFs were characterized using XRD, IR, Raman, TEM, SEM, and STEM. Due to their highly oriented hollow innerchannel and cobalt oxide NPs, glusocse sensor based C_MCNFs exhibits high performance. .

2. We fabricated an organic/inorganic 1D tube-in-tube composite and demonstrated its use as a high-performance sensor transducer. To fabricate the tube in tube structure, hybrid solution which composed of DMF, EtOH, PVP and $SnCl_2$ was applied to the electrospinning method. The SnO_2 surface coated with polypyrrole could detect DMMP with high sensitivity and selectivity. The unique structure of the tube-in-tube PPy@SnO_2-based gas sensor enabled the low MDL (0.05 ppb) at room temperature. This novel approach incorporating the PPy@SnO_2 tube-in-tube structure is expected to advance the application of 1D organic/inorganic materials in high-performance sensors.

3. We successfully fabricated a FET system sensor transistor using PDGF-B binding aptamer-conjugated CPZCNFs as a transducer. The CPZCNFs was fabricated via single-nozzle co-electrospinning and vapor deposition polymerization (VDP). Due to the zinc oxide nanonodules on the MCNF surface, there was no need for any further treatment for surface functionalization to form the CPPy layer. Then, the CPZCNFs were immobilized on the IDA substrate and bonded to the amine-modified PDGF-B binding aptamer by amide covalent bonding. The CPZCNFs-aptamer (CPB-Abt) FET sensor system

showed real-time responses and a very low detection level (5 fM) for PDGF-BB. Additionally, the CPB-Apt sensor displayed high selectivity for PDGF-BB. Furthermore, the CPB-Apt sensor was reusable over a long period because of the covalent bonding of each component. From a sensor performance point of view, the CPB-Apt FET sensor should be applicable over a wide range of applications in biological and environmental research.

References

[1] H. D. Tran, D. Li, R. B. Kaner, *Adv. Mater. (Weinheim, Ger.)* **2009,** *21,* 1487.

[2] M. R. Abidian, D. H. Kim, D. C. Martin, *Adv. Mater. (Weinheim, Ger.)* **2006,** *18,* 405.

[3] Q. Wei, F. Xiong, S. Tan, L. Huang, E. H. Lan, B. Dunn, L. Mai, *Adv. Mater. (Weinheim, Ger.)* **2017,** *29*.

[4] H. G. Wang, S. Yuan, D. L. Ma, X. B. Zhang, J. M. Yan, *Energy Environ. Sci.* **2015,** *8,* 1660.

[5] X. Lu, C. Wang, F. Favier, N. Pinna, *Adv. Energy Mater.* **2017,** *7*.

[6] L. B. Huang, W. Xu, J. Hao, *Small* **2017,** *13*.

[7] S. Gong, W. Cheng, *Adv. Electron. Mater.* **2017,** *3*.

[8] R. Vasita, D. S. Katti, *Int. J. Nanomed.* **2006,** *1,* 15.

[9] R. Khajavi, M. Abbasipour, A. Bahador, *J. Appl. Polym. Sci.* **2016,** *133*.

[10] D. Li, Y. Xia, *Adv. Mater. (Weinheim, Ger.)* **2004,** *16,* 1151.

[11] X. Wang, Q. Li, J. Xie, Z. Jin, J. Wang, Y. Li, K. Jiang, S. Fan, *Nano Lett.* **2009,** *9,* 3137.

[12] U. Feldkamp, C. M. Niemeyer, *Angew. Chem. Int. Ed.* **2006,** *45,* 1856.

[13] N. G. Chopra, R. J. Luyken, K. Cherrey, V. H. Crespi, M. L. Cohen, S. G. Louie, A. Zettl, *Science* **1995,** *269,* 966.

[14] G. Mogilevsky, Q. Chen, A. Kleinhammes, Y. Wu, *Chem. Phys. Lett.* **2008,** *460,* 517.

[15] R. Tenne, L. Margulis, M. Genut, G. Hodes, *Nature* **1992,** *360,* 444.

[16] I. Kiricsi, Á. Fudala, Z. Kónya, K. Hernádi, P. Lentz, J. B. Nagy, *Appl. Catal., A* **2000,** *203,* L1.

[17] R. Moradian, S. Azadi, S. V. Farahani, *Phys. Lett. A* **2008,** *372,*

6935.

[18] Y. Xia, P. Yang, Y. Sun, Y. Wu, B. Mayers, B. Gates, Y. Yin, F. Kim, H. Yan, *Adv. Mater. (Weinheim, Ger.)* **2003,** *15,* 353.

[19] L. Li, S. Peng, J. K. Y. Lee, D. Ji, M. Srinivasan, S. Ramakrishna, *Nano Energy* **2017,** *39,* 111.

[20] C.-L. Zhang, S.-H. Yu, *Chem. Soc. Rev.* **2014,** *43,* 4423.

[21] S. R. Merritt, A. A. Exner, Z. Lee, H. A. von Recum, *Adv. Eng. Mater.* **2012,** *14,* B266.

[22] J. T. McCann, M. Marquez, Y. Xia, *J. Am. Chem. Soc.* **2006,** *128,* 1436.

[23] C. Kim, B. T. N. Ngoc, K. S. Yang, M. Kojima, Y. A. Kim, Y. J. Kim, M. Endo, S. C. Yang, *Adv. Mater. (Weinheim, Ger.)* **2007,** *19,* 2341.

[24] W.-J. Youe, S.-M. Lee, S.-S. Lee, S.-H. Lee, Y. S. Kim, *Int. J. Biol. Macromol.* **2016,** *82,* 497.

[25] M. Inagaki, Y. Yang, F. Kang, *Adv. Mater. (Weinheim, Ger.)* **2012,** *24,* 2547.

[26] J. Jun, J. S. Lee, D. H. Shin, S. G. Kim, J. Jang, *Nanoscale* **2015,** *7,* 16026.

[27] C. Kim, Y. I. Jeong, B. T. N. Ngoc, K. S. Yang, M. Kojima, Y. A. Kim, M. Endo, J. W. Lee, *Small* **2007,** *3,* 91.

[28] I. S. Hwang, J. K. Choi, H. S. Woo, S. J. Kim, S. Y. Jung, T. Y. Seong, I. D. Kim, J. H. Lee, *ACS Appl. Mater. Interfaces* **2011,** *3,* 3140.

[29] Y. S. Kim, S. C. Ha, K. Kim, H. Yang, S. Y. Choi, Y. T. Kim, J. T. Park, C. H. Lee, J. Choi, J. Paek, K. Lee, *Appl. Phys. Lett.* **2005,** *86,* 1.

[30] T. Kida, T. Doi, K. Shimanoe, *Chem. Mater.* **2010,** *22,* 2662.

[31] J. Yue, W. Wang, N. Wang, X. Yang, J. Feng, J. Yang, Y. Qian, *J. Mater. Chem. A* **2015,** *3,* 23194.

[32] A. Kolmakov, Y. Zhang, G. Cheng, M. Moskovits, *Adv. Mater. (Weinheim, Ger.)* **2003,** *15,* 997.

[33] Z. L. Wang, *Adv. Mater. (Weinheim, Ger.)* **2003,** *15,* 432.

[34] Z. Li, Q. Zhao, W. Fan, J. Zhan, *Nanoscale* **2011,** *3*, 1646.

[35] N. D. Hoa, N. V. Quy, Y. S. Cho, D. Kim, *Phys. Status Solidi A* **2007,** *204*, 1820.

[36] S. C. Lee, S. Y. Kim, W. S. Lee, S. Y. Jung, B. W. Hwang, D. Ragupathy, D. D. Lee, S. Y. Lee, J. C. Kim, *Sensors* **2011,** *11*, 6893.

[37] C.-W. Tang, C.-B. Wang, S.-H. Chien, *Thermochim. Acta* **2008,** *473*, 68.

[38] X.-Y. Lang, H.-Y. Fu, C. Hou, G.-F. Han, P. Yang, Y.-B. Liu, Q. Jiang, *Nat. Commun.***2013,** *4*, 2169.

[39] L. Bao, T. Li, S. Chen, C. Peng, L. Li, Q. Xu, Y. Chen, E. Ou, W. Xu, *Small* **2017,** *13*, 1602077.

[40] X.-C. Dong, H. Xu, X.-W. Wang, Y.-X. Huang, M. B. Chan-Park, H. Zhang, L.-H. Wang, W. Huang, P. Chen, *ACS Nano* **2012,** *6*, 3206.

[41] J. Liu, J. Jiang, C. Cheng, H. Li, J. Zhang, H. Gong, H. J. Fan, *Adv. Mater. (Weinheim, Ger.)* **2011,** *23*, 2076.

[42] J. Zhang, X. Liu, G. Neri, N. Pinna, *Adv. Mater. (Weinheim, Ger.)* **2016,** *28*, 795.

[43] A. Kaushik, R. Kumar, S. K. Arya, M. Nair, B. D. Malhotra, S. Bhansali, *Chem. Rev. (Washington, DC, U. S.)* **2015,** *115*, 4571.

[44] T. Jiang, Z. Wang, Z. Li, W. Wang, X. Xu, X. Liu, J. Wang, C. Wang, *J. Mater. Chem. C* **2013,** *1*, 3017.

[45] J. Jang, Conducting polymer nanomaterials and their applications. In *Adv. Polym. Sci.*, **2006**; Vol. 199, pp 189.

[46] A. J. Heeger, *Angew. Chem. Int. Ed.* **2001,** *40*, 2591.

[47] A. G. MacDiarmid, *Angew. Chem. Int. Ed.* **2001,** *40*, 2581.

[48] H. Shirakawa, *Angew. Chem. Int. Ed.* **2001,** *40*, 2575.

[49] J. Jang, J. H. Oh, X. L. Li, *J. Mater. Chem.* **2004,** *14*, 2872.

[50] P. Camurlu, *RSC Adv.* **2014,** *4*, 55832.

[51] J. Fraden, *Handbook of modern sensors: Physics, designs, and applications*. **2016**; p 1.

[52] F.-G. Bănică, Optical Sensors – Applications. In *Chemical Sensors and Biosensors*, John Wiley & Sons, Ltd: 2012; pp 435.

[53] F.-G. Bănică, Acoustic-Wave Sensors. In *Chemical Sensors and Biosensors*, John Wiley & Sons, Ltd: 2012; pp 473.

[54] F.-G. Bănică, Thermochemical Sensors. In *Chemical Sensors and Biosensors*, John Wiley & Sons, Ltd: 2012; pp 157.

[55] F.-G. Bănică, Chemical Sensors Based on Semiconductor Electronic Devices. In *Chemical Sensors and Biosensors*, John Wiley & Sons, Ltd: 2012; pp 217.

[56] H. Yoon, M. Chang, J. Jang, *J. Phys. Chem. B* **2006,** *110,* 14074.

[57] S. Ko, J. Jang, *Biomacromolecules* **2007,** *8,* 182.

[58] O. S. Kwon, S. J. Park, H. Yoon, J. Jang, *Chem. Commun. (Cambridge, U. K.)* **2012,** *48,* 10526.

[59] J. S. Lee, J. Jun, D. H. Shin, J. Jang, *Nanoscale* **2014,** *6,* 4188.

[60] Y. Li, H. Ban, M. Yang, *Sens. Actuators, B* **2016,** *224,* 449.

[61] J. Jun, J. Oh, D. H. Shin, S. G. Kim, J. S. Lee, W. Kim, J. Jang, *ACS Appl. Mater. Interfaces* **2016,** *8,* 33139.

[62] S. Cho, O. S. Kwon, S. A. You, J. Jang, *J. Mater. Chem. A* **2013,** *1,* 5679.

[63] Z. Dai, G. Duan, Z. Cheng, L. Xu, T. Li, G. Liu, H. Zhang, Y. Li, W. Cai, *Chem. Commun. (Cambridge, U. K.)* **2015,** *51,* 8193.

[64] M. Xue, F. Li, D. Chen, Z. Yang, X. Wang, J. Ji, *Adv. Mater. (Weinheim, Ger.)* **2016,** 8265.

[65] T. Wang, Y. Guo, P. Wan, H. Zhang, X. Chen, X. Sun, *Small* **2016,** 3748.

[66] S. Royo, R. Martinez-Manez, F. Sancenon, A. M. Costero, M. Parra, S. Gil, *Chem. Commun. (Cambridge, U. K.)* **2007,** 4839.

[67] V. Pavlov, Y. Xiao, I. Willner, *Nano Lett.* **2005,** *5,* 649.

[68] T. J. Dale, J. Rebek, *Angew. Chem. Int. Ed.* **2009,** *48,* 7850.

[69] X. Ji, J. Zheng, J. Xu, V. K. Rastogi, T.-C. Cheng, J. J. DeFrank, R.

M. Leblanc, *J. Phys. Chem. B* **2005,** *109,* 3793.

[70] C. Hartmann-Thompson, J. Hu, S. N. Kaganove, S. E. Keinath, D. L. Keeley, P. R. Dvornic, *Chem. Mater.* **2004,** *16,* 5357.

[71] F. Wang, H. Gu, T. M. Swager, *J. Am. Chem. Soc.* **2008,** *130,* 5392.

[72] E. S. Snow, F. K. Perkins, E. J. Houser, S. C. Badescu, T. L. Reinecke, *Science* **2005,** *307,* 1942.

[73] K.-I. Chen, B.-R. Li, Y.-T. Chen, *Nano Today* **2011,** *6,* 131.

[74] L. Liu, Q. Ma, Y. Li, Z. Liu, X. Su, *Biosens. Bioelectron.* **2015,** *63,* 519.

[75] B. N. Johnson, R. Mutharasan, *Analyst* **2014,** *139,* 1576.

[76] J.-M. Moon, N. Thapliyal, K. K. Hussain, R. N. Goyal, Y.-B. Shim, *Biosens. Bioelectron.* **2018,** *102,* 540.

[77] J. S. Lee, S. G. Kim, J. Jun, D. H. Shin, J. Jang, *Adv. Funct. Mater.* **2014,** *24,* 6145.

[78] J. A. Hagen, S. N. Kim, B. Bayraktaroglu, K. Leedy, J. L. Chávez, N. Kelley-Loughnane, R. R. Naik, M. O. Stone, *Sensors* **2011,** *11,* 6645.

[79] J.-i. Hahm, *Sensors* **2011,** *11,* 3327.

[80] A. K. Wanekaya, M. A. Bangar, M. Yun, W. Chen, N. V. Myung, A. Mulchandani, *J. Phys. Chem. C* **2007,** *111,* 5218.

[81] O. Veiseh, R. Langer, *Nature* **2015,** *524,* 39.

[82] N. S. Oliver, C. Toumazou, A. E. G. Cass, D. G. Johnston, *Diabetic Med.* **2009,** *26,* 197.

[83] A. Heller, B. Feldman, *Chem. Rev. (Washington, DC, U. S.)* **2008,** *108,* 2482.

[84] M. F. Hossain, J. Y. Park, *Electroanalysis* **2014,** *26,* 940.

[85] J. Wang, D. F. Thomas, A. Chen, *Anal. Chem.* **2008,** *80,* 997.

[86] J. Wang, *Chem. Rev. (Washington, DC, U. S.)* **2008,** *108,* 814.

[87] X.-d. Wang, O. S. Wolfbeis, *Chem. Soc. Rev.* **2014,** *43,* 3666.

[88] M.-S. Steiner, A. Duerkop, O. S. Wolfbeis, *Chem. Soc. Rev.* **2011,** *40,* 4805.

[89] H. Matsui, W. Badalawa, A. Ikehata, H. Tabata, *Adv. Opt. Mater.* **2013,** *1,* 397.

[90] A. Chen, S. Chatterjee, *Chem. Soc. Rev.* **2013,** *42,* 5425.

[91] N. J. Ronkainen, H. B. Halsall, W. R. Heineman, *Chem. Soc. Rev.* **2010,** *39,* 1747.

[92] C. Chen, Q. Xie, D. Yang, H. Xiao, Y. Fu, Y. Tan, S. Yao, *RSC Adv.* **2013,** *3,* 4473.

[93] J. Liu, W. Lv, W. Wei, C. Zhang, Z. Li, B. Li, F. Kang, Q.-H. Yang, *J. Mater. Chem. A* **2014,** *2,* 3031.

[94] R. J. Barst, *J. Clin. Invest.* **2005,** *115,* 2691.

[95] M. Lassila, T. J. Allen, Z. Cao, V. Thallas, K. A. Jandeleit-Dahm, R. Candido, M. E. Cooper, *Arterioscler., Thromb., Vasc. Biol.* **2004,** *24,* 935.

[96] A. Szabó, J. Laki, H. O. Madsen, E. Dósa, Z. Prohászka, S. Rugonfalvi-Kiss, M. Kókai, G. Acsádi, I. Karádi, L. Entz, L. Selmeci, L. Romics, G. Füst, P. Garred, L. Cervenak, *Stroke* **2007,** *38,* 2247.

[97] M. Trojanowska, *Rheumatology* **2009,** *47,* v2.

[98] A. H. Shih, C. Dai, X. Hu, M. K. Rosenblum, J. A. Koutcher, E. C. Holland, *Cancer Res.* **2004,** *64,* 4783.

[99] V. Penmatsa, A. R. Ruslinda, M. Beidaghi, H. Kawarada, C. Wang, *Biosens. Bioelectron.* **2013,** *39,* 118.

[100] M. C. Vicens, A. Sen, A. Vanderlaan, T. J. Drake, W. Tan, *ChemBioChem* **2005,** *6,* 900.

[101] C. J. Yang, S. Jockusch, M. Vicens, N. J. Turro, W. Tan, *Proc. Natl. Acad. Sci. U. S. A.* **2005,** *102,* 17278.

[102] M. P. Plante, E. Bérubé, L. Bissonnette, M. G. Bergeron, M. Leclerc, *ACS Appl. Mater. Interfaces* **2013,** *5,* 4544.

[103] Y. Wang, F. Zhou, X. Liu, L. Yuan, D. Li, Y. Wang, H. Chen, *ACS Appl. Mater. Interfaces* **2013,** *5,* 3816.

[104] A. R. Ruslinda, V. Penmatsa, Y. Ishii, S. Tajima, H. Kawarada, *Analyst* **2012,** *137,* 1692.

[105] X. Fang, A. Sen, M. Vicens, W. Tan, *ChemBioChem* **2003,** *4,* 829.

[106] R. Y. Lai, K. W. Plaxco, A. J. Heeger, *Anal. Chem.* **2007,** *79,* 229.

[107] T. H. Degefa, J. Kwak, *Anal. Chim. Acta* **2008,** *613,* 163.

[108] O. S. Kwon, T. Kim, J. S. Lee, S. J. Park, H. W. Park, M. Kang, J. E. Lee, J. Jang, H. Yoon, *Small* **2013,** *9,* 248.

[109] J. S. Lee, O. S. Kwon, S. J. Park, E. Y. Park, S. A. You, H. Yoon, J. Jang, *ACS Nano* **2011,** *5,* 7992.

[110] J. Jun, J. S. Lee, D. H. Shin, J. Jang, *ACS Appl. Mater. Interfaces* **2014,** *6,* 13859.

[111] J. W. Jung, C. L. Lee, S. Yu, I. D. Kim, *J. Mater. Chem. A* **2016,** *4,* 703.

[112] K. R. Yoon, G. Y. Lee, J. W. Jung, N. H. Kim, S. O. Kim, I. D. Kim, *Nano Lett.* **2016,** *16,* 2076.

[113] S. Peng, L. Li, Y. Hu, M. Srinivasan, F. Cheng, J. Chen, S. Ramakrishna, *ACS Nano* **2015,** *9,* 1945.

[114] J. S. Jang, S. Yu, S. J. Choi, S. J. Kim, W. T. Koo, I. D. Kim, *Small* **2016,** *12,* 5989.

[115] Z. Jun, W. Shurong, X. Mijuan, W. Yan, X. Huijuan, Z. Shoumin, G. Xianzhi, W. Shihua, *J. Phys. Chem. C* **2009,** *113,* 1662.

[116] D. Pham-Cong, J. S. Park, J. H. Kim, J. Kim, P. V. Braun, J. H. Choi, S. J. Kim, S. Y. Jeong, C. R. Cho, *Carbon* **2017,** *111,* 28.

[117] M. Ding, Y. Liu, G. Wang, Z. Zhao, A. Yin, Q. He, Y. Huang, X. Duan, *Small* **2017,** *13*.

[118] J. S. Lee, O. S. Kwon, D. H. Shin, J. Jang, *J. Mater. Chem. A* **2013,** *1,* 9099.

[119] H. Zhang, X. Zhong, J. J. Xu, H. Y. Chen, *Langmuir* **2008,** *24,* 13748.

[120] D. H. Shin, J. S. Lee, J. Jun, J. Jang, *J. Mater. Chem. A* **2014,** *2,* 3364.

[121] J. Jang, J. Bae, *Sens. Actuators, B* **2007,** *122,* 7.

[122] C. A. Vetter, A. Suryawanshi, J. R. Lamb, B. Law, V. J. Gelling, *Langmuir* **2011,** *27,* 13719.

[123] S. Fujii, S. Matsuzawa, H. Hamasaki, Y. Nakamura, A. Bouleghlimat, N. J. Buurma, *Langmuir* **2012,** *28,* 2436.

[124] W. Yoon, S. H. Lee, O. S. Kwon, H. S. Song, E. H. Oh, T. H. Park, J. Jang, *Angew. Chem. Int. Ed.* **2009,** *48,* 2755.

[125] O. S. Kwon, S. J. Park, J. Jang, *Biomaterials* **2010,** *31,* 4740.

[126] X. J. Huang, A. M. O'Mahony, R. G. Compton, *Small* **2009,** *5,* 776.

[127] H. Xie, S. C. Luo, H. H. Yu, *Small* **2009,** *5,* 2611.

[128] Z. S. Wu, H. Zhou, S. Zhang, G. Shen, R. Yu, *Anal. Chem.* **2010,** *82,* 2282.

[129] H. Hu, H. Li, Y. Zhao, S. Dong, W. Li, W. Qiang, D. Xu, *Anal. Chim. Acta* **2014,** *812,* 152.

[130] L. Guo, D. H. Kim, *Biosens. Bioelectron.* **2012,** *31,* 567.

[131] J. H. Park, J. Y. Byun, H. Mun, W. B. Shim, Y. B. Shin, T. Li, M. G. Kim, *Biosens. Bioelectron.* **2014,** *59,* 321.

국문초록

1차원 나노구조체는 높은 종횡비와 비 표면적과 같은 소재의 구조적 특성에서 나타나는 다양한 장점 덕분에, 최근에는 구성 성분과 구조 성형에 따른 물성 향상 제조방법에 대한 다양한 연구가 진행되고 있다. 전기방사법은 1차원 나노 구조체를 제조하는 방법 중 하나로, 방사 조건의 변경을 통해 유기소재에서 무기소재까지 제조가 비교적 간단하기 때문에 응용분야가 크게 확장된다는 장점이 있다. 하지만, 전기방사의 방사 조건을 통해 정밀한 1차원 구조체를 형성하는 제조 방법과 이를 심화하여 1차원 유무기 복합 소재를 제조하는 방법에 대한 연구는 아직까지 미진한 실정이다

본 학위 논문에서는 고분자와 용매, 금속산화물 전구체를 섞은 혼합 용액을 전기방사에 적용하여 최종 1차원 나노 구조체의 성분 및 형태를 조절하는 방법을 제시한다. 또한 성능 향상을 위해 1차원 나노 구조체의 표면에 전도성 고분자인 피롤을 코팅하여 1차원 유무기 복합소재를 제조하는 방법을 제시하였고 이를 다양한 센서 분야에 응용하였다.

폴리메틸메타크릴레이트/폴리아클릴로니트릴을 섞은 고분자

용액과 코발트 산화물 전구체를 전기방사에 적용하여 상분리된 나노섬유를 제조하고 이를 이용해 내부에 채널이 생긴 탄소 나노섬유 및 코발트 나노입자가 도입된 탄소 나노섬유를 제조해 전기화학 센서로 응용하였다.

또한 두 가지 이상의 용매를 섞어 1차원 나노 구조체의 형태를 조절하는 방법으로, 최종적으로 섬유, 튜브, 튜브 인 튜브 구조체를 제조해 가스센서에 응용하여 성능을 향상시켰다.

폴리비닐피롤리돈/폴리아크릴로니트릴을 섞은 고분자와 아연 산화물 전구체를 섞어 표면에 아연 나노입자가 고르게 분포된 탄소나노섬유를 제조하여 빠른 응답속도의 바이오 센서를 구현하였다.

주요어: 전기방사, 1차원 나노소재, 탄소 나노섬유, 금속산화물, 폴리피롤, 센서

학 번: 2013-22535